Technische Universität München
Fakultät für Chemie

FORMATION OF CU-(AL-)OXO CLUSTERS IN ZEOLITES FOR SELECTIVE OXIDATION OF METHANE TO METHANOL

Lei Tao

Vollständiger Abdruck der von der Fakultät für Chemie der Technischen Universität München zur Erlangung des akademischen Grades eines

Doktors der Naturwissenschaften (Dr. rer. nat.)

genehmigten Dissertation.

Vorsitzender: Prof. Dr. Ulrich K. Heiz

Prüfer der Dissertation: 1. Prof. Dr. Johannes A. Lercher

2. Prof. Dr. Klaus Köhler

Die Dissertation wurde am 10.01.2022 bei der Technischen Universität München eingereicht und durch die Fakultät für Chemie am 16.02.2022 angenommen.

„Es ist nicht genug, zu wissen, man muß auch anwenden; es ist nicht genug, zu wollen, man muß auch tun."

Johann Wolfgang von Goethe

Acknowledgements

This has been an absolutely sensational journey, though certainly there were times when I was caught off guard, at a loss. Yet as one might put it, were it not for the serendipity, an adventurer would not live up to his name. I am truly glad that I hung in there and made it through, and this would never be possible without the helping hands that I have been given throughout my very adventure.

First of all, I would like to thank my supervisor, Prof. Dr. Johannes A. Lercher, for accepting me into the group. I have to be honest that it was not always easy for me to work with you, especially when faced with your harsh, yet incisive questions. The most appalling sentence that I have ever heard here would probably be "Lei, this is a question!" Nevertheless, I guess that is just your way of teaching me how to think critically and do rigorous science, strict and profound.

My sincere gratitude also goes to Dr. Maricruz Sanchez-Sanchez, for your continuous support and guidance throughout my doctoral study. I cannot stress enough how much I benefited from our countless discussions. I am always so impressed by how you managed to disentangle complicated situations and found out a most accurate way of expressing ideas. This work would not have been completed without your relentless efforts and helps.

Of course, I should not forget our excellent administrative and technical staffs. I would like to thank Stefanie Seibold and Kateryna Kryvko for arranging various meetings and dealing with cumbersome paperwork; Bettina Federmann for sorting out and offering helps in every respect related to finance; Andreas Marx for connecting my numerous heating wires and furnaces; Martin Neukamm for doing AAS measurements and Muhammad Iqbal for locating the spared parts I needed.

I had a great time with my colleagues and friends at TC II, especially my co-workers from the methane team, Takaaki Ikuno and Insu Lee. Thank you guys for welcoming me to the team even before I came to Germany and helping me quickly integrated into the group. It was a blessing to have worked closely together with you guys and tried to squeeze more methanol out of methane. I will surely miss our chit-chats during coffee breaks and our little hunting tours for authentic Asian restaurants in Munich.

The remote company of my old friends from different places of the world made up a very important part of my life here. Many thanks go to Di Chen for being such a great friend for so many years. Your occasional greetings from Lyon assured me of not being alone here in Europe. I would also like to thank my college classmates and close friends, Dr. Meikun Shen and Dr. Zhongtian Mao. (And yes, you guys can no longer tease me for not having the same prefix you own.) Our weekly game sessions made me believe that I was not fighting this war all by myself, in game or in life.

Finally, I would like to say that I am very much grateful to my parents for always backing me up with their unconditional trust in my every life decision. Without their understanding and support, I would not have had the chance to go this far. I also owe my gratitude to my beloved wife Canace. These past several years have not been easy on us, but still we made it, together through time and space, as we always do. I cannot wait to embark on my next life chapter with you.

Lei

Garching, December 2021

Abbreviations

AAS	atomic absorption spectroscopy
aiTA	ab initio thermodynamic analysis
BAS	Brønsted acid sites
bypm	2,2'-bipyrimidinyl
CN	coordination number
DFT	density functional theory
DMFC	direct methanol fuel cell
EFAl	extra-framework Al
EME	ethyl methyl ether
Etppz	ethylpiperazine
EXAFS	extended X-ray absorption fine structure
HERFD	high energy resolution fluorescence detected
IR	infrared
LMCT	ligand-to-metal charge transfer
LMMD	low-mode molecular dynamics
MAS NMR	magic-angle spinning nuclear magnetic resonance
MD	molecular dynamics
MMO	methane monooxygenase
MR	membered-ring
MS	Mass spectrometer
MTG	methanol-to-gasoline
MTO	methanol-to-olefins
pMMO	particulate methane monooxygenase

SEM	secondary electron multiplier
sMMO	soluble methane monooxygenase
TDDFT	time-determined density functional theory
UV-Vis	ultraviolet-visible
XANES	X-ray absorption near-edge structure

Abstract

The selective oxidation of methane to methanol requires di- and trimeric Cu-oxo clusters embedded in zeolites. These clusters interact with extra-framework aluminum, and their reactivity is mediated by the local steric environment of the micropores in zeolites. Subtle pretreatment strategies, developed in this thesis, adjust the chemical and steric environment to increase the efficiency of the selective methane oxidation.

Zusammenfassung

Die selektive Oxidation von Methan zu Methanol erfordert in Zeolithe eingebettete di- und trimere Cu-oxo Cluster. Diese Cluster wechselwirken mit Extraframework Aluminium und ihre Reaktivität wird durch die lokale sterische Umgebung der Mikroporen in Zeolithen gesteuert. Die subtilen Vorbehandlungsstrategien, die in dieser Arbeit entwickelt wurden, stellen die chemische und sterische Umgebung ein, um die Effizenz für die selektive Oxidation von Methan zu erhöhen.

Table of Contents

3.   Influence of Cu Concentration on Equilibrium of Cu-(Al-)oxo Cluster Speciation in Mordenite for Oxidative Transformations of Methane

4.   Activity Enhancement from Formation of Cu-Al-oxo Clusters in FER via Mild Steaming

1. General Introduction

1.1. Necessity and Challenge in Methane Utilization

Over the past few decades, methane has emerged as one of the most important feedstocks for various chemicals and fuels due to its increasing availability discovered in different forms, such as shale gas and methane clathrates.[1, 2] Despite the relative abundance, the utilization of methane still requires special techniques and handlings, as natural gas, what the majority of naturally occurring methane is in form of, is usually found alongside other fossil fuel reserves,[3, 4] which in most cases are located in remote areas far away from standing industrial infrastructures. This requires a long-range transportation of natural gas, which would not be economically feasible unless a full-on liquefaction is manageable.[5] The boiling point of methane, however, is only 109 K at atmospheric pressure, which makes the transportation in liquid form an impractical option. As a result, most natural gas found in remoteness is simply flared on-site in practice, leaving an appreciable waste in a potential energy source and posing a further burden on global warming.[6-8]

The valorization of methane via chemical transformation constitutes a viable scheme for more efficient utilization of natural gas.[9] Nevertheless, the challenge lies in the recalcitrant nature of methane, as it is a non-polar molecule with a high C-H bond dissociation energy of 105 kcal mol^{-1}. To effectively activate methane, harsh reaction conditions are oftentimes necessary, leading to a limited selectivity toward desired products.[10, 11] Therefore, it is of great significance to understand the catalytic processes of methane conversion for a better design of less energy-intensive, yet product-specific reaction pathways.

1.2. Reaction Pathways of Methane Conversion

Methane, as the simplest alkane molecule, consists of four equivalent C-H bonds. As mentioned earlier, the dissociation energy of the C-H bond amounts to 105 kcal mol^{-1}, resulting in a generally high activation barrier for methane conversion. Yet still, methane shows its versatility in chemical transformations, given the suitable reaction conditions and catalytic systems.[9, 12]

The oxidation of methane into various oxygenates represents a most common way to functionalize methane. The oxidative functionalization of methane proceeds with a sequential insertion of oxygen into the C-H bonds (with release of water), forming methanol, formaldehyde, formic acid/carbon monoxide and carbonic acid/carbon dioxide in cascade (Equation 1.1).[13] The insertion of oxygen disintegrates the symmetry and introduces polarity into the molecule, which in turn leads to a weakened strength in the remaining C-H bonds.[14] This makes the corresponding oxygenates more susceptible toward further oxidation than methane and thus a target-specific transformation of methane into any of the intermediates in the oxidation chain particularly difficult to achieve. For this reason, a facile methane oxidation without meticulously designed schemes easily ends up in complete combustion into carbon dioxide (or its equivalent).

$$(1.1)$$
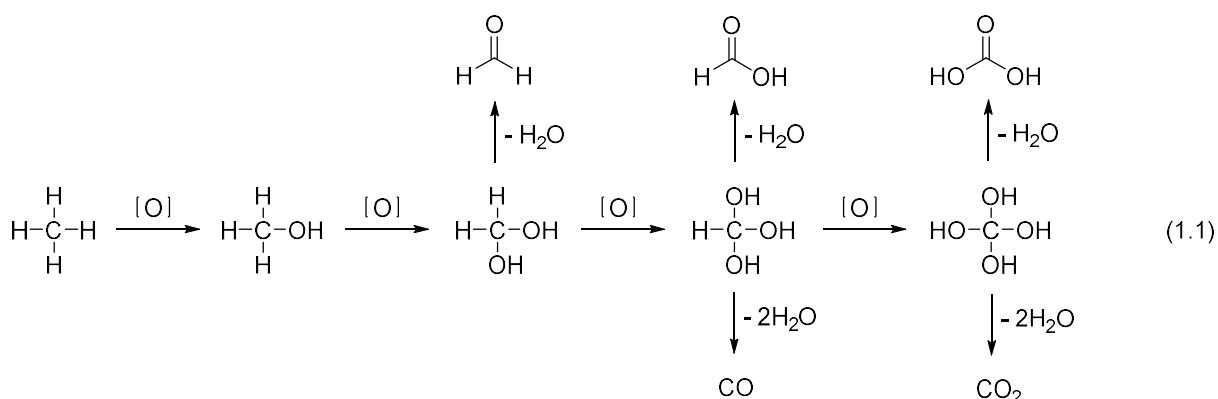
The halogenation of methane by molecular halogens stands for a different route of functionalization of C-H bonds. Similar to tandem oxidation, the reaction occurs via a stepwise replacement of C-H bond with C-X bond through a radical mechanism, yielding mono- or poly- halogenated methane depending on the halogenating agents and the operating conditions (Equation 1.2).[15] The production of halomethanes is of great industrial relevance, not only that some of them are widely used as organic

solvents, but that monohalomethane in particular can also be readily integrated into current industrial processes in a similar way to methanol.[15]

$$CH_4 \ + \ X_2 \ \longrightarrow \ CH_3X \ + \ HX$$

$$CH_3X \ + \ X_2 \ \longrightarrow \ CH_2X_2 \ + \ HX$$

$$CH_2X_2 \ + \ X_2 \ \longrightarrow \ CHX_3 \ + \ HX \qquad (1.2)$$

$$CHX_3 \ + \ X_2 \ \longrightarrow \ CX_4 \ + \ HX$$
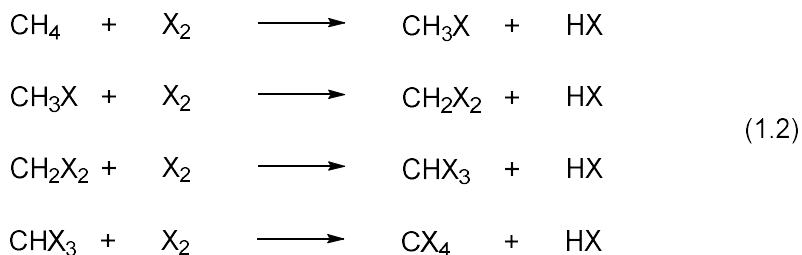
Another commonly used strategy for methane conversion is the (non-)oxidative dehydrogenation of methane to construct other hydrocarbons, which is typically identified with the formation of C-C bonds. The oxidative coupling of methane, for example, provides an opportunity to form C_2 products including ethane and ethylene (Equation 1.3).[16] The reaction involves a thermal catalytic generation of methyl radicals on the catalyst surface, followed by a coupling reaction between two methyl radicals (and further dehydrogenation).[17] This process usually operates at high temperatures (750 - 950 °C) and suffers from inevitable deep oxidation of methyl radicals into carbon dioxide, which has still prevented the process from commercial implementation to this day.[18] The dehydrogenative aromatization, on the other hand, gives rise to the possibility of constructing aromatic rings from methane (Equation 1.4). Despite its great economic potential, its strongly endothermic nature prevents appreciable formation of benzene at equilibrium unless using an impractically high reaction temperature, which usually causes severe coking, resulting in fast deactivation of the catalyst.[19, 20]

$$2\,CH_4 \ + \ O_2 \ \longrightarrow \ H_3C{-}CH_3 \ + \ H_2O$$
$$2\,CH_4 \ + \ O_2 \ \longrightarrow \ H_2C{=}CH_2 \ + \ 2\,H_2O \qquad (1.3)$$

$$6\,CH_4 \ \longrightarrow \ C_6H_6 \ + \ 9\,H_2 \qquad (1.4)$$
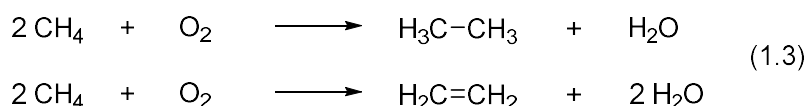
1.3. Methanol as Feedstock for Energy and Chemicals

Among various downstream products in methane conversion, methanol has its unique advantages as a primary target. As stated in Chapter 1.2, methanol sits on top of the oxidation chain of methane, which means the loss of chemical energy during oxidation is kept to minimum compared to the others in the series. Besides, methanol has a boiling point of 65 °C and a vapor pressure of 13 kPa at 20 °C with a volumetric energy density of 15.6 MJ L^{-1}. Taken together, it makes methanol a suitable liquid medium to replace non-condensable natural gas in terms of direct transportation from remote reserves.
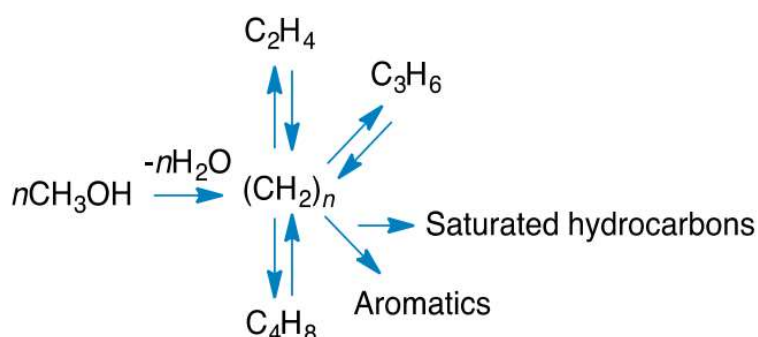
Figure 1.1 Schematic representation of methanol-related industrial processes[21]

More importantly, methanol is a key ingredient for multiple essential industrial processes.[22-24] The methanol-to-olefins (MTO) process, for instance, converts methanol into light olefins, mostly ethylene and propylene, which can directly feed into the polymer industry for vast production of plastics. Methanol can also be used to produce liquid fuels through what is known as the methanol-to-gasoline (MTG) process. Essentially, both processes start with dehydration between the methanol molecules over the acid sites of zeolite materials to form an equilibrium mixture of methanol, dimethyl ether and water. The equilibrium mixture goes through an induction period to form a hydrocarbon pool in the micropores of zeolites, which then, depending on the operating conditions and catalytic systems, produces a series of olefinic, paraffinic or even aromatic products through repetitive methylation, hydride transfer and dealkylation steps.[25, 26] These methanol-centric processes are fundamental in the

chemical industry, as they potentially bridge the gap between the increasing demands on petrochemicals and the dwindling oil reserves.
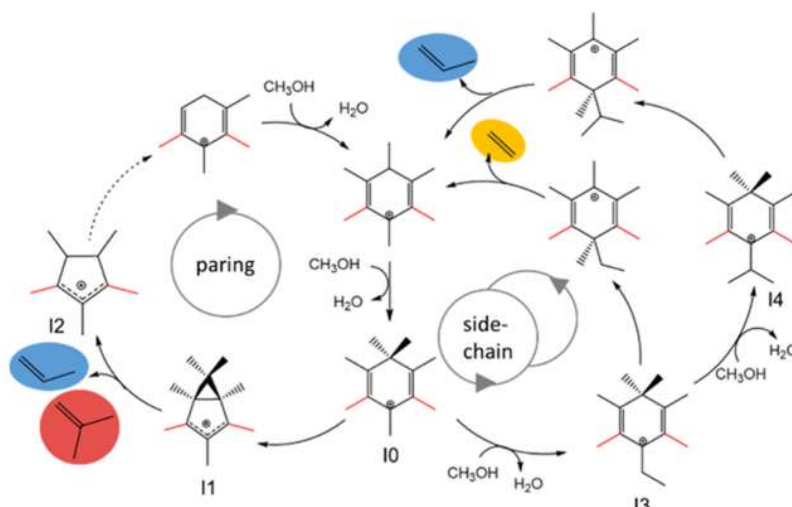
Figure 1.2 Formation of light olefins through hydrocarbon pool mechanism[25]

As a rather stable liquid at ambient condition, methanol can also be directly used as a fuel chemical due to its reasonably high energy density. The direct combustion of methanol is the most straightforward way of releasing its stored chemical energy, while harvesting the released energy from combustion is intrinsically low in efficiency. Instead, we can harness the chemical energy in form of electricity in a controlled manner via the direct methanol fuel cell (DMFC).
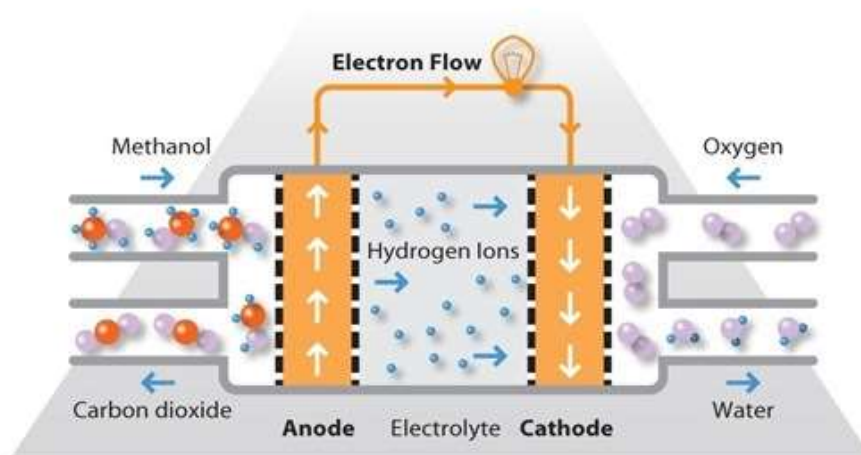
Figure 1.3 Illustration of the working principle of a DMFC

The DMFC operates on catalytic oxidation of methanol with molecular oxygen to form water and carbon dioxide.[27] As depicted in Figure 1.3, the whole reaction is separated into two half reactions taking place on each electrode. On the anode side, methanol is oxidized with the consumption of water to produce carbon dioxide and protons. Through the proton exchange membrane, the formed protons are transported to the cathode, where the reduction of oxygen occurs with protons to form water. The electron transportation driven by the differential potentials between two electrodes provides the energy that powers the connected devices.

In spite of its potential applications in various aspects, the DMFC is mostly limited by a low achievable energy conversion efficiency of only 30% - 40%.[28, 29] This arouses intensive efforts in research to promote its operational efficiency toward the theoretical limit of 97%.[30] Another prohibitive nature of DMFC comes from the heavy use of noble metals, especially platinum, as the catalytic materials. The limited reserve and the corresponding high price significantly increases the overall cost of the setups. In this regard, the search for base metal surrogate that bears comparable efficiency is still ongoing and would be a major focus in future studies.[27]

1.4. Industrial Process of Methane-to-Methanol Conversion

To date, the current industrial process of the methane-to-methanol conversion is accomplished via a two-step process, namely the methane reforming and the methanol synthesis.[31] The methane reforming reaction refers to the chemical transformation of methane in the presence of either water[32-34] or carbon dioxide[35-37] to synthesis gas (often abbreviated as syngas, a mixture of carbon monoxide and hydrogen). Featuring the participation of water in the reaction or not, the reforming process is usually defined as steam or dry reforming.

Both reforming reactions are strongly endothermic in nature under standard conditions.[38] This means, in order to ensure a significant conversion level, a high reaction temperature must be employed. Consequently, the process is highly energy-intensive and has to be operated under a certain scale to gain economic benefits, which precludes some small-scale gas reserves. Typically, Ni or Ni-based alloy catalysts are widely used as the reforming catalysts, while in some cases, noble metal catalysts are preferred due to their enhanced activity and stability.[39, 40]

$$CH_4 + H_2O \rightleftharpoons CO + 3H_2 \qquad \Delta H_r^\circ = 206 \text{ kJ/mol} \qquad (1.5)$$

$$CH_4 + CO_2 \rightleftharpoons 2CO + 2H_2 \qquad \Delta H_r^\circ = 247 \text{ kJ/mol} \qquad (1.6)$$
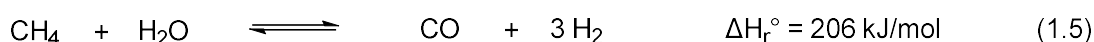
Syngas, the main product of methane reforming, can serve as an intermediate for production of numerous important commodity chemicals, including ammonia,[41] and methanol.[42] It can also be used to produce various hydrocarbon fuels via the Fischer-Tropsch process.[43-46] Among those processes, the methanol production from syngas is pivotal, largely due to the versatile roles methanol plays in the current chemical industry.

The methanol synthesis from syngas can be described by the following equations. From the observation of the overall thermodynamics, it would not be hard to tell that moderate reaction temperatures and relatively high pressures will benefit the desired transformation. Currently, the $Cu/ZnO/Al_2O_3$ catalyst is being almost exclusively used for industrial methanol synthesis.[42] Typically, the reaction is carried out at a temperature range of 200 °C to 300 °C with a pressure range of 50 bar to 150 bar.[31] A stunning selectivity of 99.9% toward methanol can be achieved over the $Cu/ZnO/Al_2O_3$

catalyst with negligible byproducts including some aliphatic hydrocarbons and higher alcohols. Despite the high efficiency and almost specificity in the transformation, the understanding on the exact mechanism over $Cu/ZnO/Al_2O_3$ remains elusive. The nature of the active sites and the function of each constituent are also controversial.

$$CO_2 \;+\; 3\,H_2 \;\rightleftharpoons\; CH_3OH \;+\; H_2O \qquad \Delta H_r\,(298K,\,5\,MPa) = -40.9\,kJ/mol \qquad (1.7)$$

$$CO \;+\; 2\,H_2 \;\rightleftharpoons\; CH_3OH \qquad\qquad\quad \Delta H_r\,(298K,\,5\,MPa) = -90.7\,kJ/mol \qquad (1.8)$$

$$CO_2 \;+\; H_2 \;\rightleftharpoons\; CO \;+\; H_2O \qquad\quad \Delta H_r\,(298K,\,5\,MPa) = 49.8\,kJ/mol \qquad (1.9)$$
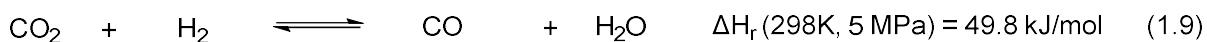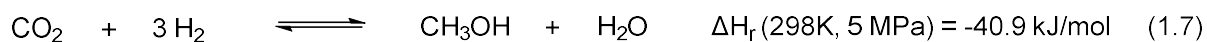
There is, though, a fair degree of agreement on the claim that methanol is primarily synthesized from the carbon dioxide (Equation 1.7) rather than carbon monoxide (Equation 1.8).[42] The conclusion was first inferred from substantial kinetic measurements in early times,[47] and later on further confirmed by isotopic labelling and carefully designed control experiments.[48, 49] Now, it is generally believed that the reaction starts with the formation of surface formate species from carbon dioxide and hydrogen. The following step, which is the most probable rate-determining step, involves the hydrogenation/hydrogenolysis of formate species into surface methoxy species. The surface-bound species then go through a further hydrogen-assisted cleavage, leaving methanol as the final product.[42]

This two-step route for methanol synthesis represents the only process currently available for mass production of methanol. Important as it is, the endothermic nature of the first step determines its practicality limited exclusively in mass gas reserves. Yet in reality, large numbers of reserves appear to be in rather small scale. As a result, a direct methane-to-methanol catalytic system that can be implemented on-site even in small scale would greatly ease off the energy waste from simple flaring and be undoubtedly in need.

1.5. Selective Oxidation of Methane to Methanol

The direct oxidation of methane selectively to methanol, as discussed above, is a promising way to tackle the current dilemma of natural gas utilization. The key, however, lies in the stabilization of formed methanol during the reaction, as reaction conditions capable of oxidizing methane would easily bring methanol to a full combustion, rendering an extremely low selectivity toward methanol even under delicately controlled conversion level. Multiple efforts have been made, but with limited success, to enhance the efficiency and selectivity of the transformation with both homogeneous and heterogeneous catalytic systems.[50, 51]

1.5.1. Metal Salt-Concentrated Sulfuric Acid System

The combination of metal salt and concentrated sulfuric acid was one of earliest successful examples as a homogeneous catalytic system for the selective oxidation of methane to methanol. The use of metal salts as soft oxidants largely prevents a fast and excessive oxidation process. At the same time, the formed methanol quickly turns into methyl ester in the concentrated sulfuric acid medium, which is far less reactive upon oxidation even compared to methane.[50] Taken together, the selectivity toward methanol can stay above 80% even under a significant conversion level.

The first study was initiated by Periana et al. using a $Hg(II)/H_2SO_4$ system, in which an appreciable methane conversion of 50% was reached with 85% selectivity to methyl bisulfate at a moderate temperature of 180 °C.[52] The reaction occurs via an electrophilic displacement of $Hg(OSO_3H)_2$ with methane to form CH_3HgOSO_3H. The intermediate CH_3HgOSO_3H readily decomposes and reacts with H_2SO_4 to release CH_3OSO_3H, SO_2 and Hg_2^{2+}. The catalytic cycle can be closed by a following reoxidation of Hg_2^{2+} by H_2SO_4 to regenerate $Hg(II)$. The net reaction, in this sense, would be the oxidation of methane to methanol with the reduction of sulfuric acid to sulfur oxide. Considering that the industrial process of sulfur dioxide oxidation to sulfuric acid is well established, the integration of this described transformation would lead to a net methane oxidation to methanol with oxygen as terminal oxidant. This would be of great industrial interest, despite the use of highly toxic $Hg(II)$ salts.

Later on, the same group reported a Pt(II)/H$_2$SO$_4$-based system, which increases the one-pass methanol yield up to 70% at a slightly higher reaction temperature of 220 °C.[53] The difficulty associated with using noble metal salts is their irreversible reductions to their metallic forms after reaction with methane. Thus, the key to the construction of an efficient catalytic system is to search for a proper ligand that can stabilize cationic Pt(II) species in the highly acidic and oxidative concentrated sulfuric acid medium without inhibiting its reactive nature. Upon educated screening of various N-based ligands, a dichloro(η-2-[2,2'-bipyrimidyl])platinum(II) complex was identified as the most efficient combination ((bpym)PtCl$_2$, Figure 1.4).
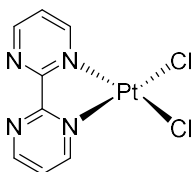
Figure 1.4 Structure of (bpym)PtCl$_2$ complex

With a series of control experiments and isotopic labelling, the authors proposed that the reaction starts with an electrophilic substitution of (bpym)Pt(OSO$_3$H)$_2$ with methane to yield a key Pt^{II}-CH$_3$ species. Unlike the Hg(II) case, the formed Pt^{II}-CH$_3$ species is transient and cannot be directly observed during the reaction. Following that, the Pt^{II}-CH$_3$ species is further oxidized into a Pt(IV) complex by sulfuric acid with release of sulfur dioxide. The formed Pt(IV) complex undergoes a reductive elimination to yield methyl sulfate and completes the catalytic cycle (Figure 1.5). The whole process can be integrated with industrially available sulfuric acid synthesis process as well.
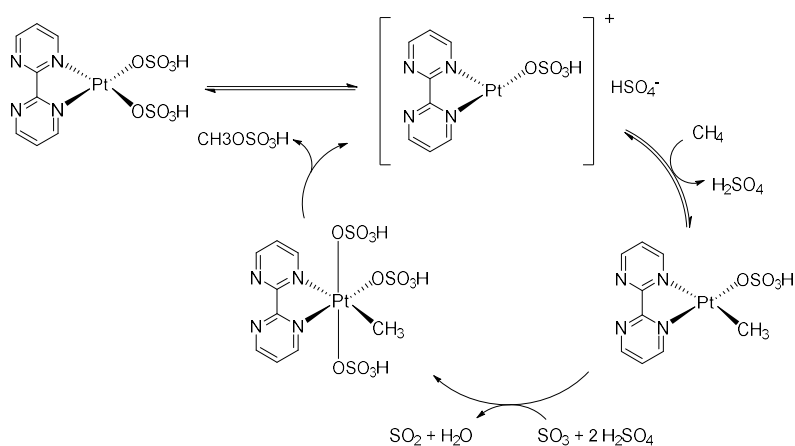
Figure 1.5 Proposed mechanism for (bpym)PtCl$_2$ catalyzed methane oxidation

The versatility of the Periana-Catalytica system was proved later on by its applicability to other transition metal cations, including Pd(II)[54] and Au(III),[55] and even extrapolation to molecular iodide as the soft oxidants.[56] The system marked a major breakthrough in the field of selective oxidation of methane to methanol, as any previously reported system never achieved a methyl product yield of higher than 3%. Nonetheless, the corrosive nature of sulfuric acid and the high cost related to the use of noble metals are the two major problems that would hopefully be resolved in future studies.

1.5.2.   Enzyme-Inspired Cu-Complexes system

In nature, a class of bacteria, named the methanotrophic bacteria, can harness the chemical energy of methane via selective oxidation, thanks to the presence of a particular kind of enzyme called the methane monooxygenase (MMO). There are two types of MMO, namely the soluble MMO (sMMO, Figure 1.6a), which contains di-iron center with an oxo-bridge, and the particulate MMO (pMMO, Figure 1.6b), in which the exact identity of the Cu-based active center remains unclear and yet to be elucidated.[57] The MMO is by far the most efficient system for methane-to-methanol transformation even under ambient conditions.[58] Ideally, we can extract the enzymes from the bacteria and use them directly in the industrial production. This is, as a matter of fact, unrealistic, due to a demandingly delicate environment necessary for enzyme catalysts to realize their potentials.
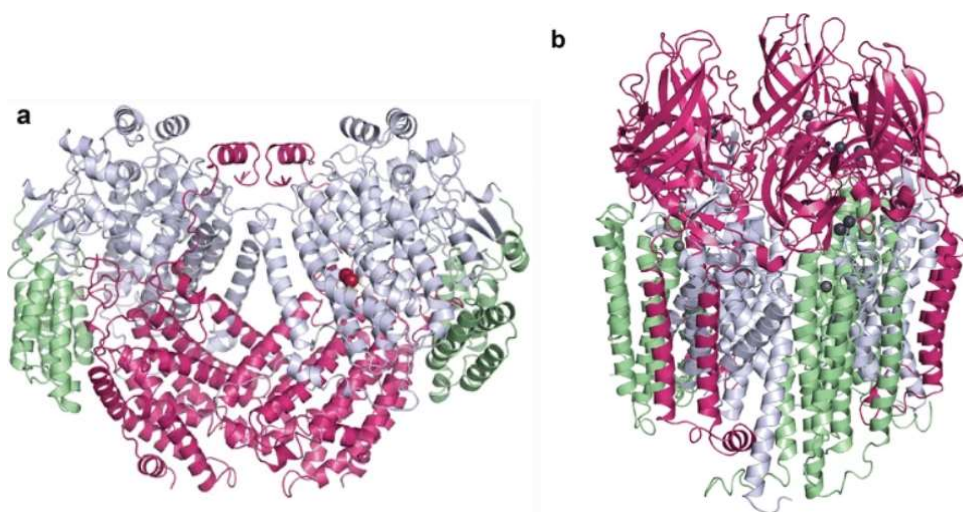
Figure 1.6 Schematic representation of protein structure of (a) sMMO, (b) pMMO[57]

Because of that, research focuses have been directed to designing and assembling Cu-based complexes, which mimic the coordination environment of certain peptide fragments identified as catalytically relevant sections in pMMO. Chan et al. reported a tricopper-based 3,3'-(1,4-diazepane-1,4-diyl)bis[1-(4-ethylpiperazine-1-yl)propan-2-ol] complex ([Cu^{I}Cu^{I}Cu^I(7-N-Etppz)]$^+$), which can almost stoichiometrically transform methane into methanol after being activated under oxygen atmosphere.[59] The complex can be regenerated via treatment with hydrogen peroxide and readily enter the next activation-reaction cycle (Figure 1.7a). It is worth mentioning that the hydrogen peroxide added to the reaction mixture has to be kept under a certain amount, since excessive dosage would trigger an abortive cycling competing with the desired reaction pathway (Figure 1.7b).
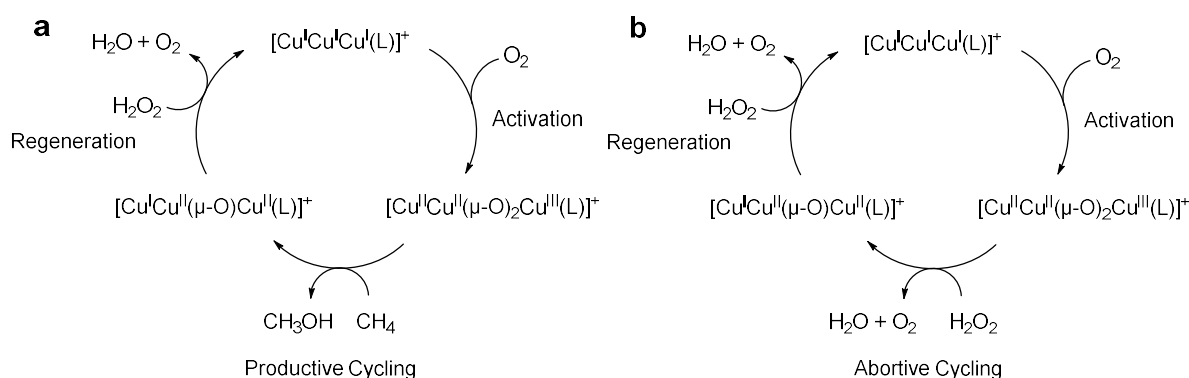
Figure 1.7 [Cu^{I}Cu^{I}Cu^I(7-N-Etppz)]$^+$-mediated (a) productive cycling, (b) abortive cycling

As a homogeneous system, the overall catalytic efficiency is limited by the solubility of reactants in the solvent. By immobilizing the complex onto a mesoporous silica material, not only did the separation/recovery become much easier to handle, but the "over solubility" from the confinement effect can also be taken advantage of to boost the reactivity.[60] Results show that the heterogenized tricopper complex demonstrated a much higher turnover number without mitigating its selectivity. Even with higher amount of hydrogen peroxide in presence, the abortive recycling did not weigh in as significantly as in the free complex case, which largely upgrades the capacity of the

process. The catalyst can be reused for at least three consecutive cycles without obvious loss of intrinsic activity, confirming its heterogeneous nature.

The biomimetic Cu-based complexes exemplify the rational design of catalytic systems based on the understanding of enzyme catalysis. The system demonstrates a remarkable efficiency at ambient temperature, which reflects an accurate portrait of structural features from the corresponding enzyme. The major drawback of the system involves the tedious synthesis procedure of the Cu complexes and the indispensable use of hydrogen peroxide for regeneration of the catalyst. In this regard, the construction of less synthesis-intensive but equally active complexes and the search for a more readily available surrogate for hydrogen peroxide would be the next step in this field.

1.5.3. Cu-zeolite-based system

Zeolite is a class of crystalline aluminosilicate materials,[61] which features a plethora of well-defined structural varieties, as in pores, channels, pockets, cages etc.[62, 63] The dimension of those structural features can be compatible with reacting molecules, thus offering a tailor-made microenvironment for specific chemical transformations, which makes it a perfect candidate for shape-selective catalysis.[64-67] Typical zeolites consist of alumina and silica tetrahedra as building units. The inclusion of alumina into the framework induces negative charges, which can serve as docking sites for cationic species. In this sense, Cu-based cationic species can be introduced into the material via ion-exchange. Combined with the confinement effect led by structures, Cu-zeolite materials are naturally considered as potential biomimetic catalysts for the selective oxidation of methane to methanol.[68, 69]

The first attempt was pioneered by Groothaert et al., in which Cu-exchanged ZSM-5 samples were tested active for the methane-to-methanol oxidation.[70] Different from the enzyme and Cu complexes, Cu-ZSM-5 samples participate in the reaction in a three-step fashion, namely the catalyst activation, the methane reaction, and the product extraction (Figure 1.8). More specifically, the catalyst was first activated in an oxygen flow at 450 °C to ensure the formation of an active bis-(μ-oxo) dicopper cluster, identified by the generation of an ultraviolet-visible (UV-Vis) absorption band centered

at 22700 cm^{-1}. Then, methane was passed over the activated catalyst at a lower reaction temperature of around 200 °C. At the same time, a simultaneous decay of the 22700 cm^{-1} band was observed, which signified the reaction between the formed active clusters and methane. No products, however, was detected during this stage, probably due to the strong absorption of the products on the material. This was later proved by examining the extract after treating the methane-reacted samples with a water/acetonitrile mixture. Methanol was the only product discovered in the extract with a highest amount of 8.2 µmol/g, which only corresponded to less than 5% of the total Cu atoms in the material. In spite of a low population of active species, this study established a standard reaction scheme, which was later widely adopted by the work to follow.
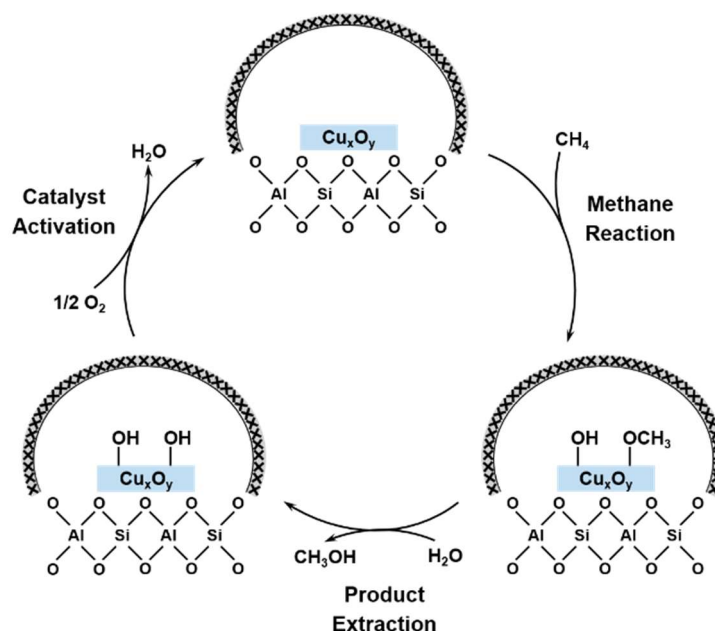
Figure 1.8 Reaction scheme for Cu-zeolite catalyzed selective oxidation of methane to methanol

The identification of catalytically active Cu species has always been a topic of great interest in the field. In this study, the active site associated with the UV-Vis band at 22700 cm^{-1} was first attributed to a bis-(μ-oxo) dicopper cluster according to joint spectroscopic results.[71] A follow-up study aimed at demystifying the active site with resonance enhanced Raman spectroscopy via tuning the laser at this intense absorption feature.[72] The use of isotopically labelled $^{18}O_2$ led to certain shifts sensitive

to specific clusters. Combined with DFT and normal coordinate analysis calculations, the authors confirmed that the active site should be a mono-(µ-oxo) dicopper cluster. With the same technique, the authors later reported the presence of a transient µ-(η^2-η^2)-peroxo dicopper precursor. The precursor was found to be only stable at room temperature, and quickly transform into the active mono-(µ-oxo) dicopper cluster upon heating, which readily took part in the methane oxidation reaction.[73]

Apart from Cu-ZSM-5, Cu-exchanged mordenite (Cu-MOR) was also shown to be active in early studies.[74] The same active clusters as in Cu-ZSM-5 was first proposed for Cu-MOR, due to a similar UV-Vis absorption band observed at 22200 cm^{-1}. Further efforts differentiated the absorption band into two components centered at 21900 cm^{-1} and 23100 cm^{-1}.[75] They were attributed to two mono-(µ-oxo) dicopper sites, very similar in most aspects. There is, though, difference in the reactivity of those two clusters, due to their different locations in the zeolite lattice. By probing the Cu species with a bulky tetrahydrofuran molecule, the authors confirmed that the intrinsically more active cluster is located in the more spatially constrained intersection of side pocket and 8 MR channel, while the less active one is found in the intersection of side pocket and 12 MR channel.[76] The close interaction between the substrate and zeolite lattice is what gave rise to a change in the absorption enthalpy, and accordingly contributed to the higher catalytic activity.

In 2015, a breakthrough in the overall catalytic efficiency was reached on a single-site Cu-MOR system, in which the total oxygenate yield was shown to be one order of magnitude higher than all previously reported literature (160 versus 13 µmol/g).[77] A delicate pH control during the ion exchange was found to be key to ensure a homogeneous Cu speciation in the zeolite. More specifically, the pH of the Cu acetate solution was tuned to 5.7 to maximize the concentration of Cu(OH)$^+$ for higher exchange capacity, while avoiding its further hydrolysis and precipitation before ion-exchange. Catalytic tests show that a constant methane/Cu stoichiometry of 1/3 was achieved irrespective of the Cu concentrations and the Si/Al ratios of parent materials. IR spectroscopy combined with probe molecules confirmed that Cu clusters are preferentially stabilized in the pore mouth of the 8 MR side pockets. EXAFS data compared with simulated spectra from a DFT-optimized structure identified the trinuclear [Cu$_3$(µ-O)$_3$]$^{2+}$ cluster as the active sites.
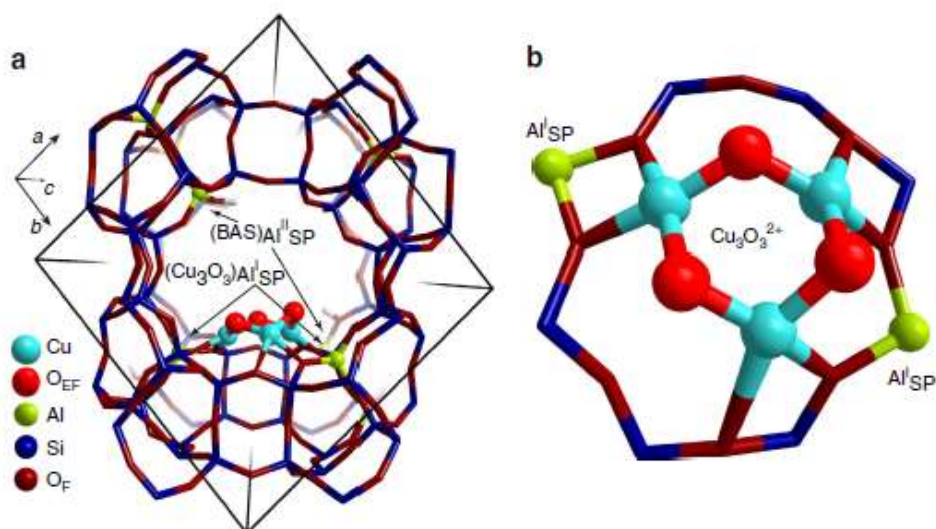
Figure 1.9 Structure and location of the trinuclear $[Cu_3(\mu-O)_3]^{2+}$ cluster in MOR

A follow-up study showed that upon elevated methane pressure of 40 bar, the overall yields of the Cu-MOR series increased by almost 100%, implying that a second active oxygen from the $[Cu_3(\mu-O)_3]^{2+}$ cluster took part in the reaction.[78] DFT calculations illustrated that the overall thermodynamics of utilizing the second oxygen atom from the cluster is favored under an increased methane chemical potential led by higher pressure. The activation of the third oxygen, on the other hand, would be unfavorable even under much higher pressure, consistent with the experimental results.

Parallel to the trimeric species raised for Cu-MOR system, dimeric clusters are also frequently proposed as possible active centers.[79, 80] The presence of spectator species, however, oftentimes lower the average Cu effiencies, thus inhibiting a direct corroboration from the stoichiometry. In this sense, Pappas et al reported a highly-active Cu-MOR sample, which exhibits a Cu efficiency of 0.47, while the other samples from the series still show a typical value of ca. 0.3.[81] By applying a multivariate curve resolution analysis of the measured XANES data, the authors claimed a universal presence of dimeric active sites in the samples, while the difference in Cu efficiencies came from the relative abundance of those sites. The outstandingly high density of active sites for the most active sample was attributed to a synergistic effect of compositional parameters and reaction conditions.
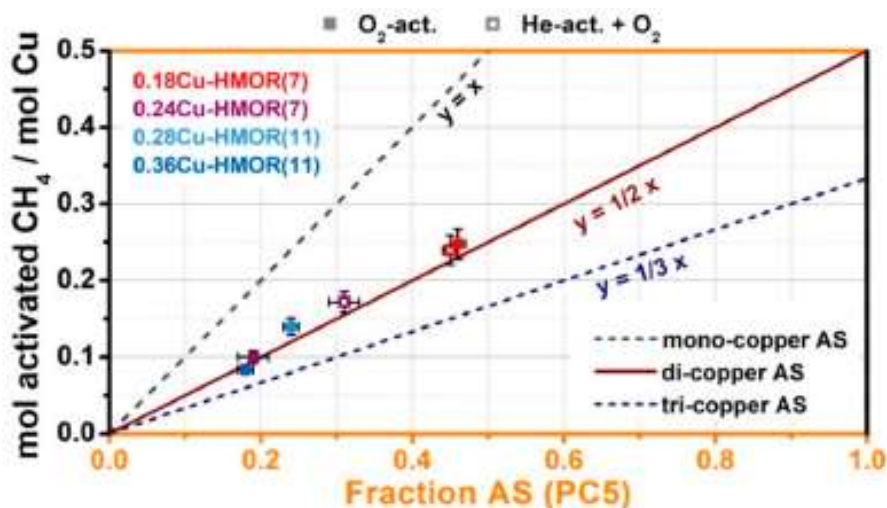
Figure 1.10 Correlation of Cu efficiencies with the principle component identified as the active species

A thorough examination was later-on performed on the Cu-MOR sample showing 0.47 stoichiometry to unravel the underlying factors contributing to its exceedingly high activity.[82] Essentially, the presence of extra-framework Al (EFAl) was found to be strongly correlating with materials showing higher activities. Even though the authors explicitly stated that the exact function that EFAl served in the activity enhancement remained speculative, the consideration of positive effect from EFAl when evaluating the efficiency and active clusters should not be overlooked.

More recently, Lee et al identified a Cu-Al oxo cluster formed in an EFAl-rich MOR via a combination of spectroscopic methods and TDDFT calculations.[83] The authors discovered a Cu-MOR series showing an unprecedented stoichiometry of 0.58. A comprehensive investigation on the parent MOR material showed a noticeably high amount of EFAl species located in the bottom of the side pocket. Both ^{27}Al MAS NMR and Al K-edge XANES were performed on the highly active Cu-MOR series to monitor the change in the states of Al species upon the introduction of Cu species. Due to the paramagnetic effect of Cu(II) species, the decrease of intensity in the tetrahedral Al species observed in ^{27}Al MAS NMR was accompanied by a simultaneous line broadening effect, which made uncertain the determination on the change of states of Al solely based on MAS NMR. With Al K-edge XANES, however, it is clear that part of

the Al species experienced a change of coordination structure from octahedral to tetrahedral, which is the first indication of Al inclusion in the active clusters.
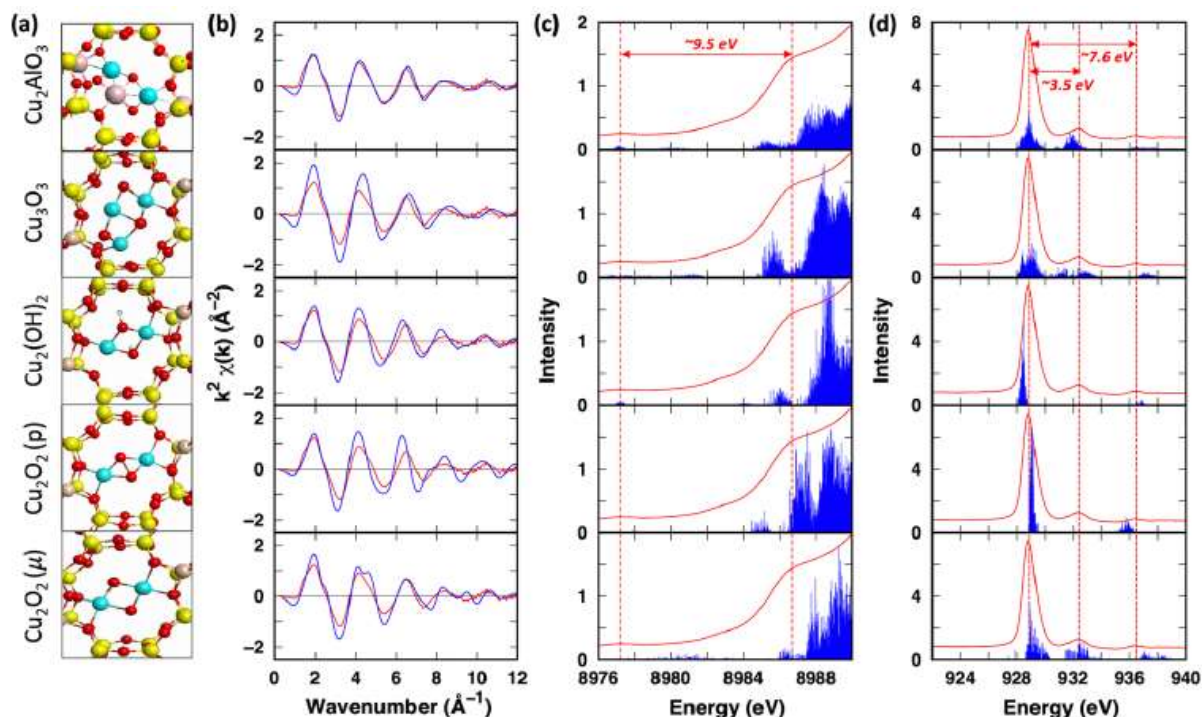
Figure 1.11 Illustration of annealed structures of five selected clusters and the comparison of their simulated spectra with experimental ones

To prove that, further detailed XAS studies were performed on the sample including Cu K-edge HERFD-XANES, conventional Cu K-edge XANES and Cu L_3-edge XANES. The spectroscopic fingerprints from the measured sample were put in comparison with the spectral simulations from five possible structures. All simulated Cu K-edge XANES showed a transition at ΔE greater than 10 eV, while the experimental value was only at 9.5 eV. On the contrary, the Al-containing $[Cu_2AlO_3]^{2+}$ cluster showed transitions at ΔE of ~3.3 and ~7.8 eV in Cu L_3-edge XANES, which matched very well with the experimental values of ~3.5 and ~7.6 eV. No other selected structures demonstrated as good consistency as the $[Cu_2AlO_3]^{2+}$ cluster. Hence, the $[Cu_2AlO_3]^{2+}$ cluster was concluded to be the most possible structure allowing a highly efficient transformation of methane to methanol. Clearly, the presence of EFAl is an indispensable prerequisite for the formation of such cluster.

Apart from ZSM-5 and MOR, many other zeolite frameworks, including MAZ,[84, 85] FER,[86, 87] CHA,[88-92] have also been shown to host various Cu-oxo clusters active for the selective oxidation of methane to methanol. Undoubtedly, the diverse geometries and dimensions of different pore structures play a pivotal role in shaping the active clusters hosted inside. In fact, it should not be overlooked that other factors including the cocations,[93, 94] the framework aluminum distributions,[88] preparation conditions,[95] etc can also influence to different extent the formation of active clusters, as discussed above in the case of EFAl. Therefore, the formation of Cu-oxo clusters should be deemed as a convoluted process, and all contributive factors need to be taken into consideration while evaluating the possible structure.

1.6. Scope of the Thesis

Cu-exchanged zeolites represent a class of materials widely reported to be active for the selective oxidation of methane to methanol. The formation of active Cu-oxo clusters bearing different nuclearities and reactivities is subject to various factors including the zeolite framework and local chemical environment. In this regard, the identification of the active cluster will not only help us understand how the formation of particular clusters is influenced by specific factors, but also pave for a rational adjustment of local structures in exchange for the formation of intrinsically more active clusters.

In the first part, the aim of the study will be looking into the Cu speciation in a series of Cu-FER samples prepared from an optimized ion-exchange procedure. The residual BAS in the samples upon introduction of Cu species will be first examined through IR spectroscopy to gain preliminary information on the nuclearities of exchanged Cu clusters. The use of NO as probe molecule will further help determine the aggregation and distribution of the Cu species hosted in the framework. The identified active species determined from measurements in controlled conditions will be correlated with activity performance at ambient and elevated methane pressure to gain information on the composition of the cluster. The exact identity of the active cluster will be confirmed by the combination of EXAFS fitting and in-situ Raman spectroscopy.

In the second part, the study will be focused on the reactivities of active Cu clusters hosted in an EFAl-rich MOR zeolite under various reaction conditions. The co-existence of a trimeric Cu-oxo cluster and a dimeric Cu-Al-oxo cluster is proposed to account for the activity performance shown at ambient methane pressure. The combination of ab initio thermodynamic analysis and molecular dynamics will be used to search for the most probable cluster and study its reactivity toward methane activation. The distribution will be explained by the Cu-induced interconversion between the two clusters supported by calculations, which will be further corroborated with Cu L_3-edge XANES and in-situ UV-Vis studies. Based on the cluster distribution, the overall activity performance will be derived and compared with the experimental results in the selective oxidation of methane to methanol at elevated pressure and oxidative etherification of methane to ethyl methyl ether.

In the last part, the effect of activity enhancement will be studied on the Cu-FER series through a systematic mild steaming approach. The mild steaming conditions will first be screened to determine how the activity increase is linked to steaming temperature and atmosphere. Upon establishment of the optimal mild steaming condition, the steamed samples will be subject to activity testing at both ambient and elevated methane pressure and compared with the untreated series. The structural change induced by mild steaming will be examined by IR spectroscopy. It is proposed that the EFAl species generated from mild steaming will be integrated into the active Cu-oxo clusters, leading to the formation of Cu-Al-oxo clusters and corresponding activity enhancement observed in steamed series. The generation and presence of Cu-Al-oxo species will be confirmed through IR with NO adsorption and UV-Vis spectroscopic studies.

1.7. References

1. D. Malakoff, *Science*, **2014**, *344*, 1464.

2. R. A. Kerr, *Science*, **2010**, *328*, 1624.

3. M. J. Economides and D. A. Wood, *J. Nat. Gas Sci. Eng.*, **2009**, *1*, 1-13.

4. C. D. Masters, D. H. Root and R. M. Turner, *World conventional crude oil and natural gas; identified reserves, undiscovered resources and futures*, Report 98-468, 1998.

5. M. Ulvestad and I. Overland, *Int. J. Environ. Stud.*, **2012**, *69*, 407-426.

6. R. W. Howarth, *Energy Sci. Eng.*, **2014**, *2*, 47-60.

7. L. Milich, *Glob. Environ. Change*, **1999**, *9*, 179-201.

8. A. K. Jorgenson, *Soc. Forces*, **2006**, *84*, 1779-1798.

9. H. Schwarz, *Angew. Chem. Int. Ed.*, **2011**, *50*, 10096-10115.

10. M. C. Alvarez-Galvan, N. Mota, M. Ojeda, S. Rojas, R. M. Navarro and J. L. G. Fierro, *Catal. Today*, **2011**, *171*, 15-23.

11. B. Wang, S. Albarracín-Suazo, Y. Pagán-Torres and E. Nikolla, *Catal. Today*, **2017**, *285*, 147-158.

12. A. Caballero and P. J. Perez, *Chem. Soc. Rev.*, **2013**, *42*, 8809-8820.

13. O. V. Krylov, *Catal. Today*, **1993**, *18*, 209-302.

14. R. Pitchai and K. Klier, *Catal. Rev.*, **1986**, *28*, 13-88.

15. V. Paunović and J. Pérez-Ramírez, *Catal. Sci. Technol.*, **2019**, *9*, 4515-4530.

16. J. H. Lunsford, *Angew. Chem. Int. Ed.*, **1995**, *34*, 970-980.

17. J. A. Labinger and K. C. Ott, *J. Phys. Chem.*, **1987**, *91*, 2682-2684.

18. J. A. Labinger, *Catal. Lett.*, **1988**, *1*, 371-375.

19. K. Huang and C. T. Maravelias, *Energy Technol.*, **2020**, *8*, 1900650.

20. J. J. Spivey and G. Hutchings, *Chem. Soc. Rev.*, **2014**, *43*, 792-803.

21. M. Xu, C. Mukarakate, D. J. Robichaud, M. R. Nimlos, R. M. Richards and B. G. Trewyn, *Top. Catal.*, **2016**, *59*, 73-85.

22. I. Yarulina, A. D. Chowdhury, F. Meirer, B. M. Weckhuysen and J. Gascon, *Nat. Catal.*, **2018**, *1*, 398-411.

23. M. Stöcker, *Microporous Mesoporous Mater.*, **1999**, *29*, 3-48.

24. L. J. France, P. P. Edwards, V. L. Kuznetsov and H. Almegren, in *Carbon Dioxide Utilisation*, eds. P. Styring, E. A. Quadrelli and K. Armstrong, Elsevier,

Amsterdam, 2015, DOI: https://doi.org/10.1016/B978-0-444-62746-9.00010-4, pp. 161-182.

25. P. Ferri, C. Li, C. Paris, A. Vidal-Moya, M. Moliner, M. Boronat and A. Corma, *ACS Catal.*, **2019**, *9*, 11542-11551.

26. U. Olsbye, S. Svelle, K. P. Lillerud, Z. H. Wei, Y. Y. Chen, J. F. Li, J. G. Wang and W. B. Fan, *Chem. Soc. Rev.*, **2015**, *44*, 7155-7176.

27. P. Joghee, J. N. Malik, S. Pylypenko and R. O'Hayre, *MRS Energy & Sustainability*, **2015**, *2*, 3.

28. P. Majidi, R. M. Altarawneh, N. D. W. Ryan and P. G. Pickup, *Electrochim. Acta*, **2016**, *199*, 210-217.

29. K. Scott and L. Xing, in *Advances in Chemical Engineering*, ed. K. Sundmacher, Academic Press, 2012, vol. 41, pp. 145-196.

30. U. B. Demirci, *J. Power Sources*, **2007**, *169*, 239-246.

31. *Fundamentals of Industrial Catalytic Processes*, **2005**, DOI: https://doi.org/10.1002/9780471730071.ch6, 339-486.

32. J. P. Van Hook, *Catal. Rev.*, **1980**, *21*, 1-51.

33. D. R. Palo, R. A. Dagle and J. D. Holladay, *Chem. Rev.*, **2007**, *107*, 3992-4021.

34. T. L. LeValley, A. R. Richard and M. Fan, *Int. J. Hydrog. Energy*, **2014**, *39*, 16983-17000.

35. D. Pakhare and J. Spivey, *Chem. Soc. Rev.*, **2014**, *43*, 7813-7837.

36. J.-M. Lavoie, *Front. Chem.*, **2014**, *2*, 81.

37. W.-J. Jang, J.-O. Shim, H.-M. Kim, S.-Y. Yoo and H.-S. Roh, *Catal. Today*, **2019**, *324*, 15-26.

38. J. H. Bitter, K. Seshan and J. A. Lercher, *J. Catal.*, **1997**, *171*, 279-286.

39. M.-S. Fan, A. Z. Abdullah and S. Bhatia, *ChemCatChem*, **2009**, *1*, 192-208.

40. Z. Bian, S. Das, M. H. Wai, P. Hongmanorom and S. Kawi, *ChemPhysChem*, **2017**, *18*, 3117-3134.

41. C. D. Demirhan, W. W. Tso, J. B. Powell and E. N. Pistikopoulos, *AIChE J.*, **2019**, *65*, e16498.

42. J. B. Hansen and P. E. Højlund Nielsen, *Handbook of Heterogeneous Catalysis*, **2008**, DOI: https://doi.org/10.1002/9783527610044.hetcat0148, 2920-2949.

43. A. P. Steynberg, in *Studies in Surface Science and Catalysis*, eds. A. Steynberg and M. Dry, Elsevier, 2004, vol. 152, pp. 1-63.

44. C. K. Rofer-DePoorter, *Chem. Rev.*, **1981**, *81*, 447-474.

45. M. E. Dry, *Catal. Today*, **2002**, *71*, 227-241.

46. J. Li, Y. He, L. Tan, P. Zhang, X. Peng, A. Oruganti, G. Yang, H. Abe, Y. Wang and N. Tsubaki, *Nat. Catal.*, **2018**, *1*, 787-793.

47. H. H. Kung, *Catal. Rev.*, **1980**, *22*, 235-259.

48. G. C. Chinchen, P. J. Denny, D. G. Parker, M. S. Spencer and D. A. Whan, *Appl. Catal.*, **1987**, *30*, 333-338.

49. G. Liu, D. Willcox, M. Garland and H. H. Kung, *J. Catal.*, **1985**, *96*, 251-260.

50. B. G. Hashiguchi, S. M. Bischof, M. M. Konnick and R. A. Periana, *Acc. Chem. Res.*, **2012**, *45*, 885-898.

51. L. Tao, I. Lee and M. Sanchez-Sanchez, *Catal. Sci. Technol.*, **2020**, *10*, 7124-7141.

52. R. A. Periana, D. J. Taube, E. R. Evitt, D. G. Löffler, P. R. Wentrcek, G. Voss and T. Masuda, *Science*, **1993**, *259*, 340.

53. R. A. Periana, D. J. Taube, S. Gamble, H. Taube, T. Satoh and H. Fujii, *Science*, **1998**, *280*, 560.

54. R. A. Periana, O. Mironov, D. Taube, G. Bhalla and C. J. Jones, *Science*, **2003**, *301*, 814.

55. C. J. Jones, D. Taube, V. R. Ziatdinov, R. A. Periana, R. J. Nielsen, J. Oxgaard and W. A. Goddard Iii, *Angew. Chem. Int. Ed.*, **2004**, *43*, 4626-4629.

56. R. A. Periana, O. Mirinov, D. J. Taube and S. Gamble, *Chem. Commun.*, **2002**, DOI: 10.1039/B205366G, 2376-2377.

57. M. O. Ross and A. C. Rosenzweig, *J. Biol. Inorg. Chem.*, **2017**, *22*, 307-319.

58. M. H. Sazinsky and S. J. Lippard, in *Sustaining Life on Planet Earth: Metalloenzymes Mastering Dioxygen and Other Chewy Gases*, eds. P. M. H. Kroneck and M. E. Sosa Torres, Springer International Publishing, Cham, 2015, DOI: 10.1007/978-3-319-12415-5_6, pp. 205-256.

59. S. I. Chan, Y.-J. Lu, P. Nagababu, S. Maji, M.-C. Hung, M. M. Lee, I. J. Hsu, P. D. Minh, J. C. H. Lai, K. Y. Ng, S. Ramalingam, S. S. F. Yu and M. K. Chan, *Angew. Chem. Int. Ed.*, **2013**, *52*, 3731-3735.

60. C.-C. Liu, C.-Y. Mou, S. S. F. Yu and S. I. Chan, *Energy Environ. Sci.*, **2016**, *9*, 1361-1374.

61. J. V. Smith, *Zeolites*, **1984**, *4*, 309-310.

62. L. B. McCusker and C. Baerlocher, in *Studies in Surface Science and Catalysis*, eds. J. Ĉejka and H. van Bekkum, Elsevier, 2005, vol. 157, pp. 41-64.

63. Y. Li and J. Yu, *Chem. Rev.*, **2014**, *114*, 7268-7316.

64. J. Weitkamp, S. Ernst and L. Puppe, in *Catalysis and Zeolites: Fundamentals and Applications*, eds. J. Weitkamp and L. Puppe, Springer Berlin Heidelberg, Berlin, Heidelberg, 1999, DOI: 10.1007/978-3-662-03764-5_5, pp. 327-376.

65. M. Dusselier, P. Van Wouwe, A. Dewaele, P. A. Jacobs and B. F. Sels, *Science*, **2015**, *349*, 78.

66. S. M. Csicsery, *Zeolites*, **1984**, *4*, 202-213.

67. N. Y. Chen and W. E. Garwood, *Catal. Rev.*, **1986**, *28*, 185-264.

68. K. T. Dinh, M. M. Sullivan, P. Serna, R. J. Meyer, M. Dincă and Y. Román-Leshkov, *ACS Catal.*, **2018**, *8*, 8306-8313.

69. M. H. Mahyuddin, Y. Shiota, A. Staykov and K. Yoshizawa, *Acc. Chem. Res.*, **2018**, *51*, 2382-2390.

70. M. H. Groothaert, P. J. Smeets, B. F. Sels, P. A. Jacobs and R. A. Schoonheydt, *J. Am. Chem. Soc.*, **2005**, *127*, 1394-1395.

71. M. H. Groothaert, J. A. van Bokhoven, A. A. Battiston, B. M. Weckhuysen and R. A. Schoonheydt, *J. Am. Chem. Soc.*, **2003**, *125*, 7629-7640.

72. J. S. Woertink, P. J. Smeets, M. H. Groothaert, M. A. Vance, B. F. Sels, R. A. Schoonheydt and E. I. Solomon, *Proc. Natl. Acad. Sci.*, **2009**, *106*, 18908-18913.

73. P. J. Smeets, R. G. Hadt, J. S. Woertink, P. Vanelderen, R. A. Schoonheydt, B. F. Sels and E. I. Solomon, *J. Am. Chem. Soc.*, **2010**, *132*, 14736–14738.

74. P. J. Smeets, M. H. Groothaert and R. A. Schoonheydt, *Catal. Today*, **2005**, *110*, 303-309.

75. P. Vanelderen, B. E. Snyder, M. L. Tsai, R. G. Hadt, J. Vancauwenbergh, O. Coussens, R. A. Schoonheydt, B. F. Sels and E. I. Solomon, *J. Am. Chem. Soc.*, **2015**, *137*, 6383-6392.

76. B. E. R. Snyder, P. Vanelderen, R. A. Schoonheydt, B. F. Sels and E. I. Solomon, *J. Am. Chem. Soc.*, **2018**, *140*, 9236-9243.

77. S. Grundner, M. A. C. Markovits, G. Li, M. Tromp, E. A. Pidko, E. J. M. Hensen, A. Jentys, M. Sanchez-Sanchez and J. A. Lercher, *Nat. Commun.*, **2015**, *6*, 7546.

78.   J. Zheng, I. Lee, E. Khramenkova, M. Wang, B. Peng, O. Y. Gutiérrez, J. L. Fulton, D. M. Camaioni, R. Khare, A. Jentys, G. L. Haller, E. A. Pidko, M. Sanchez-Sanchez and J. A. Lercher, *Chem. Eur. J.*, **2020**, *26*, 7563-7567.

79.   G. Brezicki, J. D. Kammert, T. B. Gunnoe, C. Paolucci and R. J. Davis, *ACS Catal.*, **2019**, *9*, 5308-5319.

80.   V. L. Sushkevich, D. Palagin, M. Ranocchiari and J. A. van Bokhoven, *Science*, **2017**, *356*, 523.

81.   D. K. Pappas, A. Martini, M. Dyballa, K. Kvande, S. Teketel, K. A. Lomachenko, R. Baran, P. Glatzel, B. Arstad, G. Berlier, C. Lamberti, S. Bordiga, U. Olsbye, S. Svelle, P. Beato and E. Borfecchia, *J. Am. Chem. Soc.*, **2018**, *140*, 15270-15278.

82.   M. Dyballa, D. K. Pappas, K. Kvande, E. Borfecchia, B. Arstad, P. Beato, U. Olsbye and S. Svelle, *ACS Catal.*, **2019**, *9*, 365-375.

83.   I. Lee, M.-S. Lee, L. Tao, T. Ikuno, R. Khare, A. Jentys, T. Huthwelker, C. N. Borca, A. Kalinko, O. Y. Gutiérrez, N. Govind, J. L. Fulton, J. Z. Hu, V.-A. Glezakou, R. Rousseau, M. Sanchez-Sanchez and J. A. Lercher, *JACS Au*, **2021**, *1*, 1412-1421.

84.   A. J. Knorpp, A. B. Pinar, M. A. Newton, V. L. Sushkevich and J. A. van Bokhoven, *ChemCatChem*, **2018**, *10*, 5593-5596.

85.   A. J. Knorpp, A. B. Pinar, C. Baerlocher, L. B. McCusker, N. Casati, M. A. Newton, S. Checchia, J. Meyet, D. Palagin and J. A. van Bokhoven, *Angew. Chem. Int. Ed.*, **2021**, *60*, 5854-5858.

86.   D. K. Pappas, E. Borfecchia, K. A. Lomachenko, A. Lazzarini, E. S. Gutterød, M. Dyballa, A. Martini, G. Berlier, S. Bordiga, C. Lamberti, B. Arstad, U. Olsbye, P. Beato and S. Svelle, *Top. Catal.*, **2019**, *62*, 712-723.

87.   D. K. Pappas, E. Borfecchia, M. Dyballa, K. A. Lomachenko, A. Martini, G. Berlier, B. Arstad, C. Lamberti, S. Bordiga, U. Olsbye, S. Svelle and P. Beato, *ChemCatChem*, **2019**, *11*, 621-627.

88.   D. K. Pappas, E. Borfecchia, M. Dyballa, I. A. Pankin, K. A. Lomachenko, A. Martini, M. Signorile, S. Teketel, B. Arstad, G. Berlier, C. Lamberti, S. Bordiga, U. Olsbye, K. P. Lillerud, S. Svelle and P. Beato, *J. Am. Chem. Soc.*, **2017**, *139*, 14961-14975.

89. R. Oord, J. E. Schmidt and B. M. Weckhuysen, *Catal. Sci. Technol.*, **2018**, *8*, 1028-1038.

90. B. Ipek, M. J. Wulfers, H. Kim, F. Göltl, I. Hermans, J. P. Smith, K. S. Booksh, C. M. Brown and R. F. Lobo, *ACS Catal.*, **2017**, *7*, 4291-4303.

91. B. Ipek and R. F. Lobo, *Chem. Commun.*, **2016**, *52*, 13401-13404.

92. M. J. Wulfers, S. Teketel, B. Ipek and R. F. Lobo, *Chem. Commun.*, **2015**, *51*, 4447-4450.

93. G. Brezicki, J. Zheng, C. Paolucci, R. Schlögl and R. J. Davis, *ACS Catal.*, **2021**, *11*, 4973-4987.

94. S. Grundner, W. Luo, M. Sanchez-Sanchez and J. A. Lercher, *Chem. Commun.*, **2016**, *52*, 2553-2556.

95. H. V. Le, S. Parishan, A. Sagaltchik, C. Göbel, C. Schlesiger, W. Malzer, A. Trunschke, R. Schomäcker and A. Thomas, *ACS Catal.*, **2017**, *7*, 1403-1412.

2. Speciation of Cu-oxo Clusters in FER for Selective Oxidation of Methane to Methanol

2.1. Abstract

Cu-oxo nanoclusters in Cu-exchanged zeolites catalyze methane oxidation to methanol via a three-step process. Cu-exchanged ferrierite (FER) shows high reactivities to this selective oxidation at both ambient and elevated methane pressures. The IR spectra of adsorbed NO helps differentiating active and inactive sites for the methane oxidation. Correlation of the activity with these species suggests that the active sites are dimeric Cu clusters located in the 8-membered channels of FER and these clusters contain two active O atoms with different reactivities. The combination of in situ UV-Vis, XAS and Raman spectroscopic studies shows that the structure of the active site is a $[Cu_2O_2]^{2+}$ cluster exchanged in FER Al pairs. This cluster is able to oxidize up to two methane molecules at elevated methane chemical potential.

2.2. Introduction

With its high availability and especially with the increasingly available biogenic resources, methane has become a major feedstock for energy carriers and chemicals.[1-3] The direct conversion of methane to methanol, is conceptually a particularly interesting pathway, since it can potentially bypass the synthesis gas step and be integrated in the current industrial infrastructure.[4] However, achieving a high selectivity toward methanol is challenging due to its own high susceptibility to oxidation in comparison to methane, and, thus, special strategies are required to stabilize the methanol formed in the reaction.[5, 6]

Cu-zeolite based catalysts have proven a successful system for the selective oxidation of methane to methanol in a three-stage stepwise process.[7, 8] The key to ensure a high selectivity lies in the formation of methoxy species bound to Cu-oxo clusters, whose limited oxygen availability prevents deep oxidation.[9] However, this poses limitations on the overall methane reaction yields, because it requires a stepwise or chemical looping. In order to enable this route eventually at one operation temperature, it is required to gain fundamental understanding on the nature of active Cu-oxo clusters, the mechanism of methane activation and the stabilization of the product.

To date, various Cu-oxo clusters, mostly dimeric[10-15] and trimeric structures, [16-19] have been proposed, hosted by different zeolite frameworks. Yet, the formation of Cu-oxo clusters is subject to many factors, including the framework aluminum distribution,[19] the presence of co-cations[16, 20] and preparation conditions.[17] This leads to differing activities of Cu ions even for catalytic materials prepared in the same type of framework. In most cases, the coexistence of spectator species increases the complexity of the spectroscopic analysis and the identification of active sites.

Among the wide range of frameworks that have been evaluated, mordenite (MOR)[14, 17, 21] and mazzite (MAZ)[22, 23] are reported to be most effective in terms of hosting a high concentration of active clusters. Studies have demonstrated that those active clusters are selectively accommodated in the 8 membered-ring (MR) structures of the zeolites.[17, 22, 24] This points to a pertinent role of 8 MR in the stabilization of active clusters. In this regard, ferrierite (FER), as an 8 MR containing framework, has also been previously reported to stabilize active clusters for selective oxidation.[25, 26]

Relatively high yields were reported, but the correlation between activity and concentration of Cu exchanged in FER hints at a different speciation in comparison to Cu-MOR.

Therefore, we decided to revisit this material and to investigate the activity in methane oxidation of a series of Cu-FER materials prepared via an ion exchange protocol that minimizes the formation of CuO_x neutral species.[17] In situ spectroscopy of the oxygen activated catalysts allowed us to identify the distribution and nuclearity of the Cu-oxo species. The spectroscopic information combined with activity tests at different chemical potentials shows that a dimeric Cu cluster located in the 8 MR is the active site and that such cluster can utilize up to two active oxygen atoms to convert two CH_4 molecules to methanol.

2.3. Results and Discussions

2.3.1. Methane activation and methanol production over Cu-FER materials

A series of Cu-FER samples with various Cu concentrations were prepared by the ion-exchange of H-form FER, following a previously reported ion-exchange procedure.[17] The physicochemical properties of the samples are compiled in Table A 2.1 in the Supporting Information. The activity in CH_4 oxidation was measured in a typical three-step reaction scheme, including (1) activation of Cu-FER materials in O_2 at 500 °C, (2) reaction with 1 or 40 bar of CH_4 at 200 °C and (3) steam-assisted desorption of formed products at 135 °C. As depicted in Figure 2.1, the activity of Cu-FER samples increases linearly with Cu concentration. It should be noted that the Cu-FER series shows an activity threshold of 150 µmol/g, i.e., samples with loading below this Cu concentration did not show activity both at 1 and 40 bar. This indicates that at low concentrations the most preferred sites for Cu ion exchange lead to inactive species.

Increment of Cu concentration above 150 µmol/g led to a linear increase of activity. This points to a homogeneous speciation with formation of catalytic sites upon increasing the amount of exchanged Cu species. Interestingly, the slope of the activity increase at 1 bar is 0.33. In previous Cu-MOR studies,[16, 17] we have concluded that an increase in yields of 1 mol CH_4 per 3 mol Cu indicates that a trimeric Cu_3O_3 cluster acts as active site, i.e., activation of one methane molecule requires three Cu atoms. Thus, the slope of 0.33 here observed at 1 bar could indicate the formation of similar trimeric Cu species in the FER framework, but only after saturation of some specific exchange sites that lead to inactive Cu species.

When the reaction is performed at a CH_4 pressure of 40 bar, all active samples achieved substantially higher yields than at 1 bar. With a slope of 0.58, the yields are approximately 2-fold higher than the yields at 1 bar. This suggests that the oxidation activity in Cu-FER increases with CH_4 pressure and that one additional CH_4 molecule is activated per cluster. This increase in yields with higher CH_4 pressures is attributed to the higher CH_4 chemical potential, which enables a second oxygen of the Cu-oxo cluster to take part in the reaction.[21]
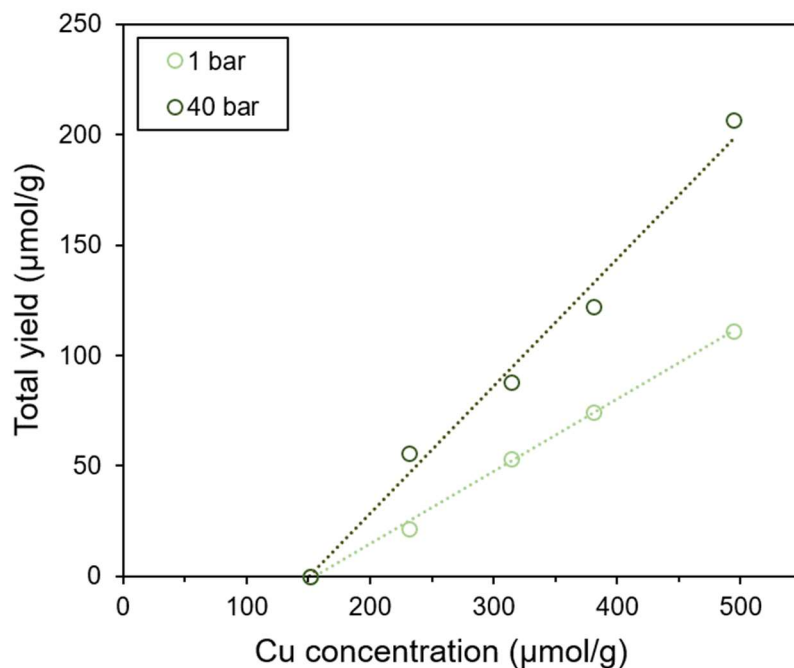
Figure 2.1 Total yield of converted methane amount as a function of Cu concentration at different methane pressures

2.3.2. Activity, nuclearity and local distribution of Cu species in FER framework

A first indication of the structure of the exchanged Cu species in the zeolite can be obtained by quantifying the concentration of Brønsted acid sites (BAS) in the parent H-FER that has disappeared upon Cu introduction. In Figure 2.2a it is observed that the decrease in the intensity of O-H vibration band of Si-OH-Al species is proportional to the increase of Cu loadings. This shows the substitution of protons by ion exchange with Cu cations. The ratio of consumed BAS per introduced Cu cation (consumed BAS/Cu) is defined by the nuclearity and charge of the exchanged Cu clusters. Tri-copper clusters in Cu-MOR consumed 0.69 BAS per Cu,[17] which agrees well with two BAS exchanged by a divalent cluster containing three Cu atoms. Di-copper clusters identified in other zeolites[27, 28] and [Cu(II)-OH]$^+$ monomers[27] have nominal consumed BAS/Cu of 1, while bare Cu(II) cations exchanged in Al pairs consume two BAS per Cu.

Our analysis of Cu-FER series shows that, under dry and oxidized state, all samples have consumed BAS/Cu ratios between 1.1 and 1.3 with an average of ca. 1.2 (Table

A 2.2). Based solely on the changes in activity with Cu loading (Figure 2.1), one can speculate that the lack of activity of Cu-FER at Cu loadings under 150 µmol/g is related to the exchange of Cu(II) as bare ions in Al pairs, which are regarded as inactive in the reaction of CH_4 to CH_3OH.[25, 27, 29] Then, at higher loadings, the increase in CH_4 reacted with Cu loading with a slope of ca. 0.33 could be related to the dominant formation of trimeric clusters in analogy to Cu-MOR. However, the consumed BAS/Cu ratio of an inactive Cu-FER with 150 µmol/g of Cu is near 1, indicating that Cu is exchanged in different structures and not as a majority of bare Cu(II) ions in Al pairs. The formation of [Cu(II)-OH]$^+$ monomers would give a BAS/Cu of 1, but its existence can be ruled out from the absence of a characteristic IR band at 3650 cm^{-1}.[27] Therefore, the average value of 1.2 consumed BAS per Cu, regardless of the Cu loading, is tentatively assigned to the formation of a majority of di-copper clusters (nominal consumed BAS/Cu of 1) with ca. 10 - 20 % of bare Cu(II) cations stabilized by Al pairs (nominal consumed BAS/Cu of 2). In any case, this experimental evidence already points to the fact that Cu speciation in FER is different from the speciation in Cu-MOR.
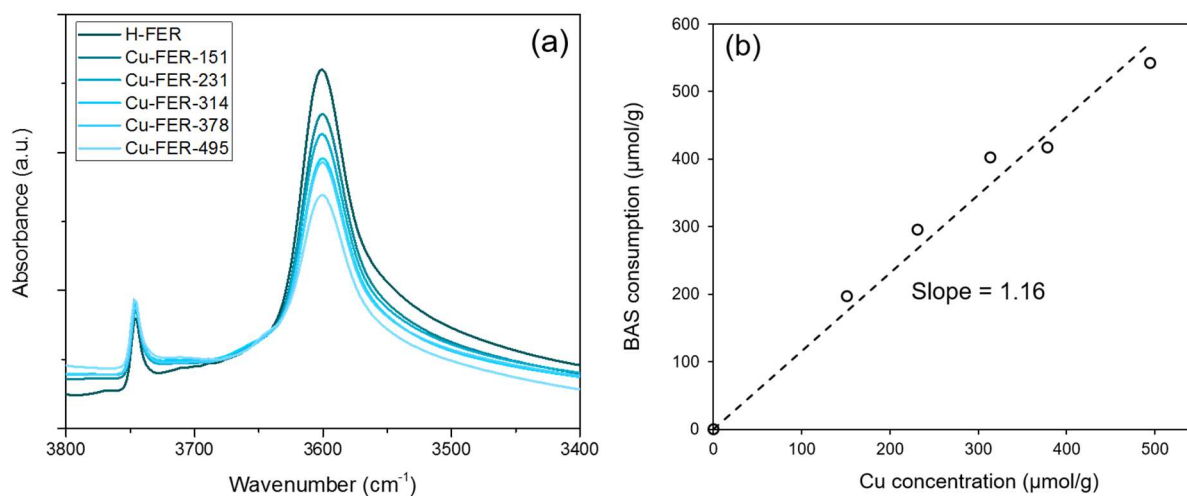

Figure 2.2 (a) Changes in the intensity O-H IR band of of Si-OH-Al species with increasing Cu concentrations in Cu-FER samples treated in O$_2$ after activation in vacuum; (b) Correlation of BAS consumption with different Cu concentrations

2.3.3. Identification of spectroscopic features of active Cu species and its location in FER framework

The aggregation and oxidation states of Cu species can be probed by IR spectroscopy of adsorbed NO (at 77 K). Yet, a typical IR measurement involves an activation procedure under vacuum at elevated temperature. This thermal treatment in vacuum or inert gas leads to an autoreduction process of at least a fraction of Cu(II) species to Cu(I).[30, 31] Therefore, an additional oxidative treatment of the samples must be applied prior to the NO adsorption in the IR cell, to ensure that the oxidation state and position of Cu species approach those on the working catalyst.

Figure 3a shows the IR spectra of the Cu-FER series with NO adsorption bands in the region of 1750 - 2000 cm^{-1}. The absorption bands of mono- and dinitrosyl species on Cu(I) appear typically at 1809 and 1824 cm^{-1}.[32] The absence of absorption features in that region confirms that the O_2 treatment in the in situ IR cell successfully reoxidized the Cu(I) species that were generated during activation (Figure A 2.1). The shoulder peak at 1879 cm^{-1} corresponds to NO absorbed on surface hydroxyl groups on the zeolite, in agreement with literature[33] and our own adsorption of NO on H-FER reference (Figure A 2.2). The main NO absorption band on Cu-FER samples consists of two main components at 1911 cm^{-1} and 1901 cm^{-1}. These bands were previously assigned to NO adsorbed on Cu(II)-oxo[34, 35] and monomeric Cu(II)[36-38] species. The weak band at 1960 cm^{-1} has been attributed by some authors to oligomeric Cu-oxo clusters active in CH_4 oxidation[36-38] while in other reports it was attributed to NO adsorbed on bare Cu(II) cations.[34] Based on the consumed BAS/Cu ratios (Figure 2.2b and Table A 2.2), and the changes in activity with Cu loading in Cu-FER (Figure 2.1), we attribute the bands at 1911 and 1901 cm^{-1} to NO adsorbed on two different oligomeric Cu(II)-oxo species. Consistently, we assign the weaker feature at 1960 cm^{-1} to bare Cu(II) cations exchanged in Al pairs in agreement with Valyon et al.[34] As a reference, we have measured NO adsorption on a Cu-exchanged AEI that was shown to contain only Cu monomers. With this material, we only detected a major absorption band at 1950 cm^{-1} and a minor one at 1930 cm^{-1} (Figure A 2.3).

Deconvolution of the NO adsorption bands on Cu(II) species for Cu-FER samples with different Cu loading allows quantifying the contribution of each site in Figure 2.3b. The first conclusion is that the NO adsorbed on Cu(II)-oxo bands at 1911 and 1901 cm^{-1}

and NO on bare Cu(II) cations band at 1960 cm^{-1} coexist in all samples. The band at 1911 cm^{-1} becomes predominant already at a Cu loading of 230 µmol/g, indicating that this Cu(II)-oxo is the majority species. Figure 2.3b also shows that the intensity of the 1911 cm^{-1} band increased more rapidly with Cu concentration than the other bands. With the distribution of each species derived from NO IR, we can calculate the BAS/Cu based on the population and nuclearity of each species, assuming that the two Cu(II)-oxo species responsible for the 1911 and 1901 cm^{-1} bands are both dimeric in nature and exchange with a BAS/Cu ratio of 1. The value calculated based on these assumptions amounts to an average of 1.1, matching well the experimental data from integration of the Si-OH-Al region (Table A 2.2).

Based on the increase of activity observed with Cu loading and the concomitant increasing relative contribution of the NO bands at 1900 - 1910 cm^{-1}, we hypothesize that these two Cu(II)-oxo species are related to the clusters active in CH$_4$ oxidation. In order to test this hypothesis, we exposed the oxygen-treated Cu-FER samples to CH$_4$ in the in situ IR cell prior to a typical NO adsorption experiment. NO adsorption IR spectra of CH$_4$-reacted samples are shown in Figure 2.3c – 2.3e. The samples with activities in CH$_4$ oxidation, Cu-FER-310 and Cu-FER-500, showed an important decrease of the intensity of the band at 1911 cm^{-1} after CH$_4$ exposure, while all the other bands of NO on Cu(II) species were not affected. At the highest Cu loadings and activities, the appearance of a band at 1811 cm^{-1} is observed for NO absorbed on Cu(I) species. Such Cu(I) species are generated via the reaction of the active Cu-oxo cluster with CH$_4$. These in situ IR spectra provide evidence that the Cu(II) species with NO adsorption band at 1911 cm^{-1} are the active sites for CH$_4$ oxidation, and it is consistent with our attribution of this band to a Cu(II)-oxo species.

In good agreement, we did not observe differences in the NO-IR spectra obtained before and after CH$_4$ reaction for the inactive Cu-FER-150 sample. Furthermore, the NO adsorption IR spectra for the Cu-FER samples measured after treatment in vacuum show that autoreduction causes a dramatic decrease of the band at 1911 cm^{-1}, while the band at 1901 cm^{-1} is less affected (Figure A 2.1). Since the autoreduction process is often related to more labile, redox active oxygen,[39, 40] this observation supports the attribution of the vibration band at 1911 cm^{-1} as indication for active Cu-oxo clusters.
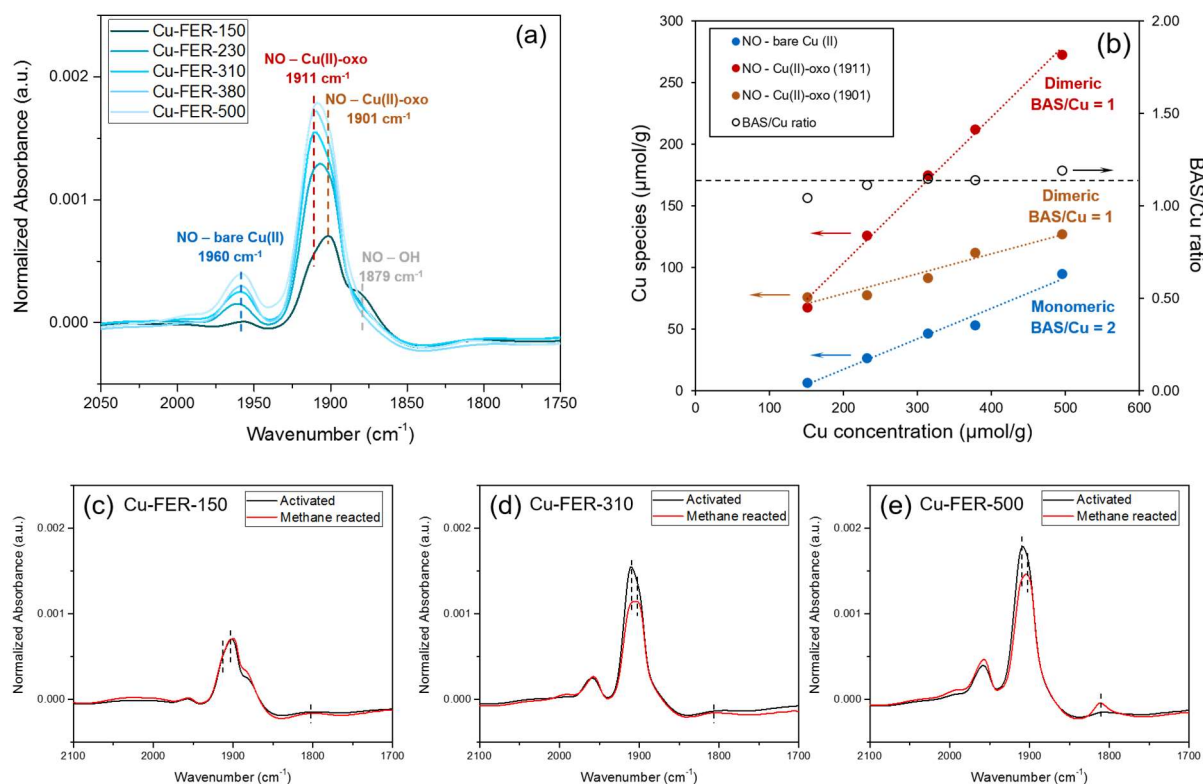
Figure 2.3 (a) Differential IR spectra of Cu-FER samples with NO adsorption; (b) changes in concentration of the different Cu(II) species identified and quantified by NO-IR, with increasing Cu concentrations in FER; comparison of IR spectra with NO adsorption before and after methane reaction of (c) Cu-FER-150; (d) Cu-FER-310; (e) Cu-FER-500

Further differentiation between active and inactive Cu(II) species in FER was provided by in-situ UV-Vis spectroscopy during CH_4 reaction (Figure 2.4). The band centered at 12000 cm^{-1} is generally associated with the d-d transition of Cu(II) species due to its d^9 electronic configuration.[41, 42] In the difference spectra obtained by subtracting the spectra of the oxygen activated sample, it can be seen that CH_4 has not led to any decrease in the UV-Vis absorption in this position for the inactive Cu-FER-150 sample. Conversely, all other Cu-FER materials are active in CH_4 oxidation and in good agreement they show a decrease in the absorption band between 10000 to 17000 cm^{-1}, indicating reduction of a fraction of Cu(II) to Cu(I) upon reaction with CH_4. In addition, the differential spectra also show a decrease in the absorption bands at 27000 and 39000 cm^{-1}. While the decrease in 39000 cm^{-1} occurs for all samples, the band at

27000 cm^{-1} is only visible for those Cu-FER materials that show activity. In good agreement, the active Cu-oxo species in Cu-MOR have been reported to absorb UV-Vis light at approximately 31000 cm^{-1}.[17, 43, 44]

A close examination of Cu-FER-150 UV-Vis spectra showed that, similar to the active Cu-FER counterparts, a band at 27000 cm^{-1} is generated during activation in O$_2$ (Figure A 2.4). However, this band remained unchanged upon exposure to CH$_4$. This again points to a Cu speciation in Cu-FER-150 similar to the rest of the Cu-FER series, in spite of its lack of activity. We speculate that the observed interaction with CH$_4$ of Cu species in Cu-FER-150 leading to the decrease of the absorption at 39000 cm^{-1} is a non-oxidative process that either generates coke or regenerates CH$_4$ upon contact with steam. Although the broadness of the UV-Vis absorption bands does not allow a reliable quantification, a qualitative assessment of the spectra shows that the decrease in intensity of the band centered at 27000 cm^{-1} is proportional to yields of CH$_4$ oxidized with increasing Cu loadings in Cu-FER series.
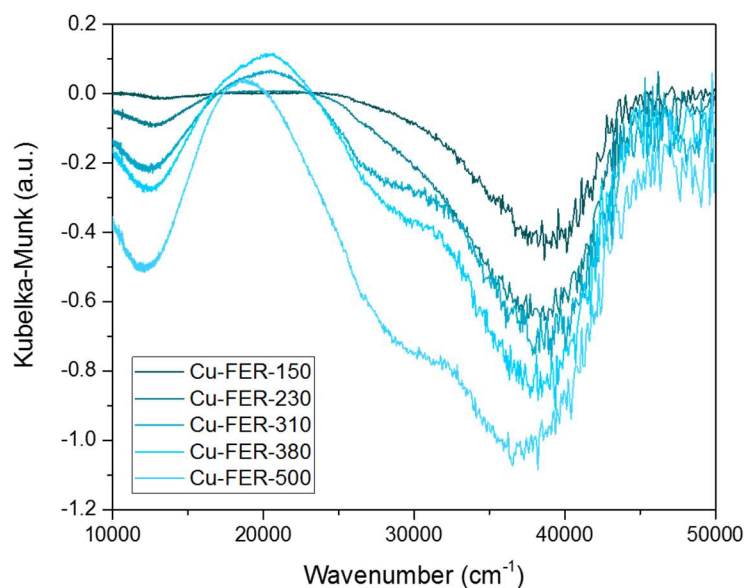

Figure 2.4 In-situ UV-Vis difference spectra of oxygen activated Cu-FER series after exposure to CH$_4$ flow at 200 °C for 30 min

In order to determine the location in the FER framework of the Cu active species associated to the NO-IR band at 1911 cm^{-1}, we investigated the changes caused upon Cu exchange on the OH IR band of bridging hydroxyl groups in H-FER. It is known that

the position of the IR bands of BAS in FER differs depending on their location.[45] (Figure A 2.5). The distribution of the introduced Cu species can be inferred by deconvoluting the difference spectra of the OH region for each Cu-FER sample. Figure 2.5a shows that the exchange of BAS in each position takes place progressively with increasing Cu amounts. Quantitative analysis shows that about 50 % of the Cu species has been exchanged in the 8 MR pores, and roughly 30% and 20% are located in the 10 and 6 MR respectively. Note that the inactive Cu-FER-150 showed a similar distribution of Cu species than the active samples with higher loadings. Therefore, we conclude that there are not any preferential exchange sites in FER at low Cu concentrations. This in turn points to the fact that the absence of activity in CH_4 oxidation of Cu-FER-150 is not directly caused by a geometry associated to particular T-sites in the framework.

The analysis of the changes in the OH vibration region upon Cu ion exchange has shown that more than 50% of the introduced Cu species are located in the 8 MR of FER framework (Figure 2.5a). In Figure 2.5b we have plotted the concentration of active Cu(II)-oxo species - based on the quantification of the NO band at 1911 cm^{-1} - versus the concentration of consumed BAS in 8 MR – based on the decrease of the sum of the OH vibrations at 3600 and 3587 cm^{-1} with Cu loading. A linear correlation with a slope close to 1 is observed. Thus, we conclude that the NO-IR band at 1911 cm^{-1} corresponds to the only active Cu(II)-oxo species in FER, and that the active site is located in the 8 MR.

Figure 5c shows the correlation between the yield of converted CH_4 at 1 and 40 bars and the deduced concentration of active Cu(II)-oxo species in 8 MR (NO band at 1911 cm^{-1}). An offset is still observed, indicating that ca. 70 µmol/g of the Cu(II)-oxo species with NO IR band at 1911 cm^{-1} do not lead to CH_4 oxidation either at 1 or at 40 bar. Based on our spectroscopic evidence, we conclude that these inactive species are a fraction of the dimeric Cu(II)-oxo species that either are inaccessible or are subject to local environment effects that hinder their reactivity. Above this Cu concentration threshold, a linear correlation is observed between activity at 1 bar of CH_4 and the concentration of Cu(II)-oxo species in 8 MR pores, with a stoichiometry, derived from the slope, of 1 CH_4 molecule activated per 2 Cu cations (Figure 2.5c). This is consistent with a dimeric Cu cluster with one active O atom. Upon increasing the pressure to 40 bar, the slope doubled to almost one CH_4 molecule per Cu or, in other words, that two

CH_4 molecules are activated per di-copper cluster. These results are evidence of the presence of a second oxygen bridge in the Cu-oxo cluster that is only active under a high CH_4 chemical potential.[21]

From the distribution of Cu species in the framework with increasing Cu concentrations, we conclude that the exchangeability of all 6, 8 and 10 MR is similar, without one site being preferred at low Cu loadings. We concluded from NO adsorption, however, that the active Cu-oxo species are located in 8 MR sites. It seems that the most exchangeable 8 MR sites in FER form inactive Cu-oxo species and, once those sites are occupied, ion exchange of protons in additional 8 MR positions with Cu(II) leads to the formation of active di-copper clusters.
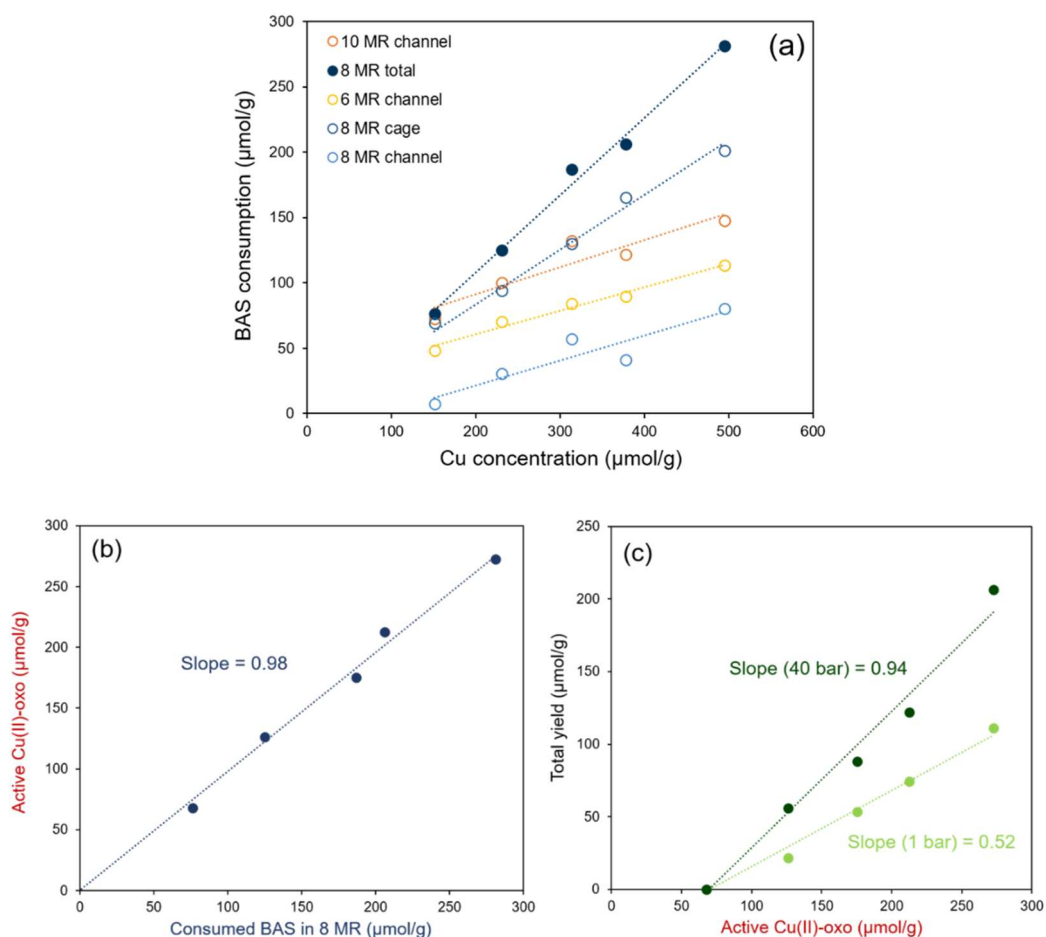

Figure 2.5 (a) Distribution of BAS consumption in each position, based on the deconvolution of remaining O-H bands after Cu exchange; (b) correlation of active Cu(II)-oxo species, as determined from IR of NO adsorption, with BAS consumption in

8 MR; (c) correlation of the total yield at different pressure with active Cu(II)-oxo species as determined from IR of NO adsorption

2.3.4. Structural features of active Cu-oxo species in FER

EXAFS at the Cu K-edge on relevant samples of the Cu-FER series is used to determine the structure of the active Cu clusters. With the information on the nuclearity and distribution of Cu species inferred from in situ IR, we have fixed the average coordination numbers of the Cu-Al path and Cu-Cu path to reduce the number of fitting parameters (Table A 2.3). The fitting results show that the Cu-FER samples, irrespective of the Cu concentrations, have an average coordination number of 3.5 - 3.6 for the Cu-O path (Table 1). This is consistent with the results of the adsorption of NO, which also point to similar proportions of the different Cu species in the whole range of Cu concentrations.

Table 2.1 Comparison of structural parameters for Cu-O path in Cu-FER derived from Cu K-edge EXAFS fitting data[a]

Sample	R (Å)	σ^2	CN
Cu-FER-150	1.95 (±0.01)	0.006 (±0.001)	3.53 (±0.28)
Cu-FER-310	1.96 (±0.01)	0.007 (±0.001)	3.63 (±0.28)
Cu-FER-500	1.94 (±0.01)	0.006 (±0.001)	3.53 (±0.22)

[a] See Figure A 2.6 and Table A 2.4 for detailed information

In situ Raman spectra of the O_2-activated Cu-FER samples (Figure 2.6) showed characteristic bands at 430 cm^{-1} and 480 cm^{-1}, which are assigned to the T-O-T bending vibrations of FER 5 MR and 4 MR, respectively.[46] The additional bands at 601 cm^{-1} and 780cm^{-1} with Cu-containing samples are in very good agreement with reported symmetric and asymmetric stretching vibrations of the Cu-O bond from a tight Cu-O-Cu angle (less than 100°).[11, 28, 47] Taking into account the presence of 2 oxygen

atoms in the active cluster determined from the activities at 40 bar CH_4, we propose that the active species is a bis-(μ-oxo) di-copper cluster, in which two oxo-bridges effectively bring closer the two Cu atoms, resulting in a tight Cu-O-Cu angle. In such configuration, the active Cu cluster appears to be tetra-coordinated. Given that we have estimated that ca. 50 % of the exchanged Cu in FER is forming active species (Figure 2.3b), the average coordination number of 3.5 from the EXAFS fitting indicates that the majority of the inactive Cu(II)-oxo species (associated to NO band at 1901 cm^{-1}) are tri-coordinated. Fewer neighboring oxygen atoms are expected to contribute to a relatively higher electron density of Cu in a tri-coordinated Cu(II)-oxo cluster, which would in turn explain a red shift of ca. 10 cm^{-1} in the vibration band of absorbed NO to the position at 1901 cm^{-1} linked to inactive Cu-oxo species. This is the case because a stronger π back donation to the antibonding orbitals from the more electron dense species causes a weakening of the N-O bond.[48]
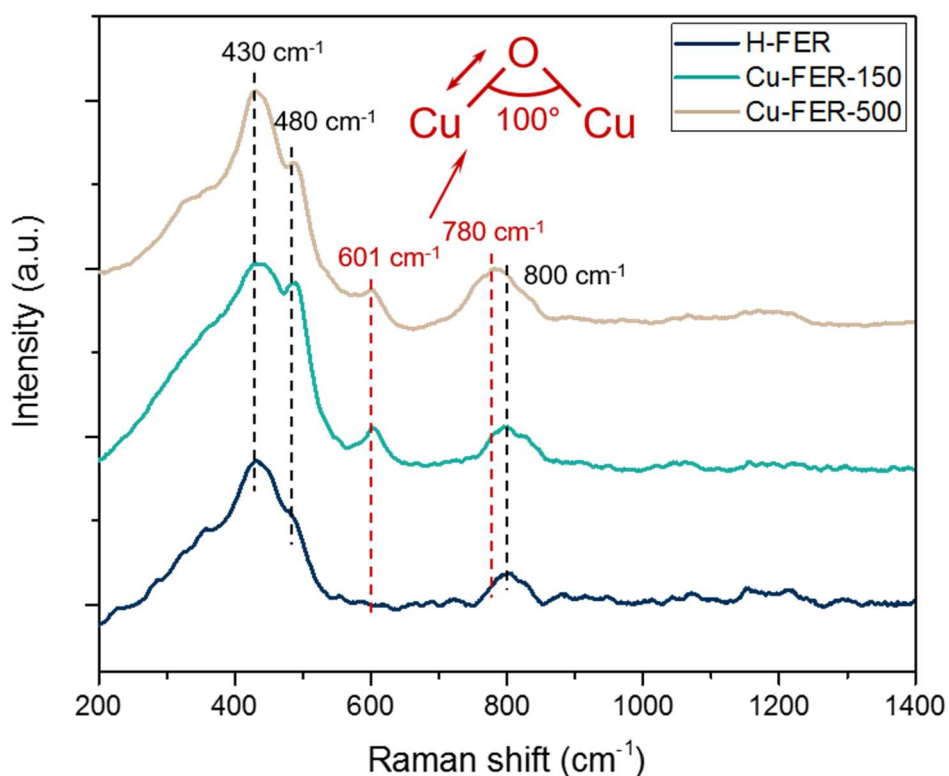

Figure 2.6 In situ Raman spectra of H-/Cu-FER measured at 200 °C after O_2 activation at 500 °C for 1 h

Based on all these spectroscopic information and the activity development of Cu-FER with increasing Cu loadings, we propose that Cu inactive species in Cu-FER are bare Cu(II) ions exchanged in Al pairs and mono-(μ-oxo) di-copper cluster with a small angle, caused probably by the highly constrained environment in FER.[28, 49] Conversely, the active species responsible for CH_4 conversion to CH_3OH in Cu-FER are di-copper clusters with two bridging oxygen atoms. We propose a resonance structure between a (μ-η^2:η^2) peroxo di-copper and a bis-(μ-oxo) di-copper cluster, similar to what Henson et al observed,[50] as shown in Figure 2.7.

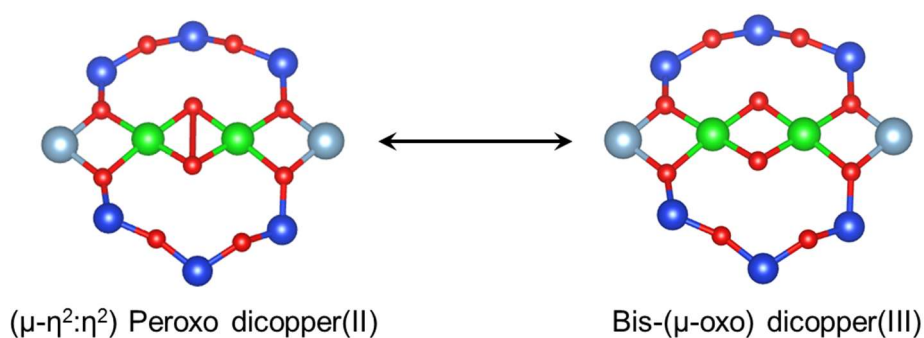(μ-η^2:η^2) Peroxo dicopper(II)   Bis-(μ-oxo) dicopper(III)

Figure 2.7 Proposed resonance structures of dimeric Cu-oxo clusters in the FER framework

Both in situ IR of NO adsorption and UV-vis show that there is not a redox interaction with CH_4 for samples with Cu loadings ≤ 150 μmol/g, in spite of containing Cu(II)-oxo species in 8-MR positions. We hypothesize that at low Cu loadings, the 8 MR positions that are preferred for the exchange of Cu(II) ions are structurally inactive or inaccessible for H_2O to hydrolyze and generate CH_3OH. Therefore, although these sites interact with CH_4, it reacts back to gas CH_4 in downstream steps. Once these 8 MR positions have been filled, Cu(II)-oxo species in active 8 MR are exchanged and their concentration increases linearly with Cu loading.

2.4. Conclusions

Cu exchanged FER zeolite was found to host three different Cu species in its pore structure; only one of them active in the CH_4 oxidation to MeOH. The combination of different in-situ spectroscopies together with the activity measurements at different CH_4 pressures allowed us to induce that the active species has a distinctive adsorbed NO vibration band at 1911 cm^{-1}. EXAFS and Raman spectroscopies in combination with the activity results at high pressures indicate that the active species is a bis-(μ-oxo) di-copper / (μ-$η^2$:$η^2$) peroxo di-copper cluster with Cu-O-Cu angles of 100° that can activate up to two CH_4 molecules per cycle. In general, Cu-FER is less active than Cu-MOR counterpart because this active cluster coexist with Cu species exchanged in 10 and 6 MR, which are not active in CH_4 oxidation.

Overall, the study shows how the combination of in-situ spectroscopies on oxidatively activated Cu zeolites allows identifying the structure and location of active species even in presence of inactive Cu-exchanged sites. In particular, IR of NO adsorption of a CH_4 activated sample revealed additional information that enable differentiation of the key species co-existing in Cu-FER materials.

2.5. Experimental Section

2.5.1. Preparation of Cu-FER samples.

Commercial available NH_4-FER (Si/Al = 9) was purchased from Tosoh Corporation. The corresponding H-FER was obtained by calcination of NH_4-FER in synthetic air flow (100 mL/min) at 550°C (10 K/min) for 6 h.

Cu-FER samples were prepared by aqueous ion exchange of H-FER with copper acetate solution under controlled conditions.[17] Typically, Cu^{2+}-exchange was carried out by dispersing 2 g of H-FER at ambient temperature in 120 mL of an aqueous solution of copper acetate (Sigma Aldrich, 99.99%) with desired concentration for 20 h. The pH of the solution was adjusted with aqueous solution of nitric acid (0.2 M) and kept to 5.5 - 6.0 during the Cu-exchange. After the exchange, the sample was separated from the suspension by centrifugation and rinsed four times with double deionized water followed by an intervening centrifugation step after each rinse cycle. The centrifugate was dried at 110 °C for 24 h and labelled as Cu-FER-x (x denotes its Cu content as in x $\mu mol_{Cu}/g_{catalyst}$). All Cu-FER samples were calcined in synthetic air flow at 500 °C (100 mL/min) for 2 h prior to IR and XAS measurements. The contents of Si, Al, Na and Cu were measured by atomic absorption spectroscopy (AAS) on a UNICAM 939 AA spectrometer after dissolution in boiling hydrofluoric acid.

2.5.2. Testing of activity for selective oxidation of methane.

The activity of the Cu-FER samples for the selective oxidation of methane to methanol was tested in a three-step reaction scheme. Typically, 50 mg of Cu-FER (250 - 400 µm) sample was packed in a stainless steel plug flow reactor with a 4-mm inner diameter. First, the sample was activated at 500 °C in O_2 flow for 1 h, cooled down to 200 °C and then flushed with He. In the next step, CH_4 was flowed over the sample at 200 °C for 3 h. Finally, the sample was flushed with He and cooled to 135 °C and subjected by a steam-assisted product desorption with 20 % H_2O in He. Reaction products were identified and quantified with a QMG 220 M1, PrismaPlus (Pfeiffer Vacuum) online MS (mass spectrometer) with a C-SEM detector by monitoring the m/z signals of 31, 44 and 46 for CH_3OH, CO_2 and $(CH_3)_2O$. $(CH_3)_2O$ was considered from

the condensation of two CH_3OH molecules and therefore the equivalent. The sum of all detected products was taken as the total yield.

2.5.3. In-situ infrared (IR) spectroscopy.

The IR spectra were recorded on a Vertex 70 spectrometer (Bruker Optics) with a resolution of 4 cm^{-1}. All samples for IR spectroscopy were pressed as self-supporting wafers with a density of ca. 10 mg/cm^2 and activated in vacuum (1.0×10^{-7} mbar) at 450 °C with a heating rate of 10 K/min for 1 h. After that, 200 mbar of synthetic air was introduced and kept in the IR cell for another 1 h for oxidative treatment of the samples. Then, the samples were allowed to cool down naturally to 40 °C before the synthetic air was evacuated again for measurement. For the measurements of NO adsorption, the samples were fully cooled down with liquid nitrogen and the IR spectra were recorded after the dosage of NO (0.01 mbar). In case of the measurements with methane reaction, the samples were allowed to cool down naturally to 200 °C instead before evacuation. Next, 10 mbar of methane was introduced and kept for 1 h to react with the activated samples. Similar NO adsorption procedure was then applied after evacuating the methane.

2.5.4. In-situ ultraviolet-visible (UV-Vis) spectroscopy.

The UV-vis spectra were measured on an Avantes AvaSpec 2048 spectrometer equipped with a high-temperature optical fiber (Avantes FCR-7UV400-2ME-HTX). The sample (250 - 400 μm) was placed in a quartz tube with square optical-grade quartz windows. The intensity of the diffuse reflectance UV-vis is shown as the Kubelka-Munk function, defined as $F(R) = (1 - R)^2 / 2R$, where $R = R_s/R_r$, R_s and R_r refer to the signal intensity of the sample and reference, respectively. The reference spectra was taken on the parent H-FER sample. The samples were first activated in synthetic air (16 mL/min) at 450 °C with a heating rate of 10 K/min for 1 h. Then the samples were cooled down to 200 °C and flushed with He (10 mL/min) for 0.5 h, followed by contact with CH_4 flow (16 mL/min) for 1 h. The spectra were recorded periodically with a certain time interval to monitor the changes through time.

2.5.5.   In-situ X-ray absorption spectroscopy.

X-ray absorption spectra were measured in beamline P65 at PETRA III of DESY in Hamburg, Germany. The electron energy was 6 GeV with a beam current of 100 mA. The beam size at the sample was 200 × 300 μm. Around 10 mg of the sample was sandwiched between quartz wools and packed in a quartz capillary reactor (1 mm outer diameter and 0.02 mm wall thickness) and placed on top of a gas blower for controlled heating. A double-crystal Si(111) monochromator was used to control the incident photon energy, and the spectra were recorded with fluorescence detector and ionization chamber detectors in the transmission mode. To suppress higher harmonics in the incident beam, the monochromator was detuned to 70% of the maximum peak intensity. Thermal activation of the samples was performed in a flow of 10% O_2 in He at 500 °C for 1 h with a heating rate of 10 K/min. After the activation, the samples were cooled down to 100 °C in the same flow for measurement. The gas flow over the samples was controlled by Bronkhorst mass-flow controllers. A Supelco 5A moisture trap was installed in the O_2/He gas line to eliminate the remaining moisture in the gas.

2.5.6.   In-situ Raman spectroscopy.

The Raman spectra were measured with a Renishaw inVia Reflex Raman System. The excitation wavelength of 532 nm for visible Raman measurements was provided by the Renishaw RL532C, Class 3B laser source. The laser power was kept below 1 mW to avoid laser-induced sample degradation during the measurement. The samples (250 - 400 μm) were placed in a quartz tube sandwiched between quartz wools. Prior to measurement, the samples were first activated in synthetic air (16 mL/min) at 450 °C with a heating rate of 10 K/min for 1 h. The spectra were then recorded after the samples were allowed to cool down to 200 °C.

2.6. Acknowledgements

2.7. Appendix

Table A 2.1 Physicochemical properties of Cu-FER samples

Sample	Cu acetate conc. (M)	Si/Al	Cu/Al	Na/Al	Cu conc. (wt%)	Cu conc. (μmol/g)
Cu-FER-150	0.0025	9	0.09	0.002	0.96	151
Cu-FER-230	0.005	9	0.13	0.002	1.47	231
Cu-FER-310	0.00625	9	0.18	0.002	2.00	314
Cu-FER-380	0.0075	9	0.22	0.001	2.40	378
Cu-FER-500	0.01	9	0.32	0.001	3.14	495

Table A 2.2 BAS consumption of Cu-FER samples in each position of the FER framework

Cu conc. (μmol/g)	BAS consumption (μmol/g)				Total BAS consumption (μmol/g)	BAS/Cu
	10 MR channel	8 MR cage	8 MR channel	6 MR channel		
0	0	0	0	0	0	-
151	72	69	7	48	196	1.30
231	100	94	31	70	295	1.28
314	132	130	57	84	403	1.28
378	121	165	41	90	417	1.10
495	148	201	80	114	543	1.10

Table A 2.3 Fitting parameters determined from NO-IR

Sample	CN_{Cu-Al}	CN_{Cu-Cu}
Cu-FER-151	1.05	0.95
Cu-FER-314	1.15	0.85
Cu-FER-495	1.19	0.81

Table A 2.4 Structural parameters for Cu in Cu-FER derived from fitting the experimental spectra to FEFF9 theoretical models

Cu-FER-150

Path	R (Å)	σ^2	CN	ΔE
Cu-O	1.95 (±0.01)	0.006 (±0.001)	3.53 (±0.28)	-6.97 (±0.85)
Cu-Al	2.76 (±0.01)	0.002 (±0.001)	<u>1.05</u>	-"-
Cu-Cu	3.04 (±0.01)	0.004 (±0.001)	<u>0.95</u>	-"-

Cu-FER-310

Path	R (Å)	σ^2	CN	ΔE
Cu-O	1.96 (±0.01)	0.007 (±0.001)	3.63 (±0.28)	-5.10 (±0.85)
Cu-Al	2.75 (±0.02)	0.005 (±0.002)	<u>1.15</u>	-"-
Cu-Cu	3.04 (±0.02)	0.008 (±0.003)	<u>0.85</u>	-"-

Cu-FER-500

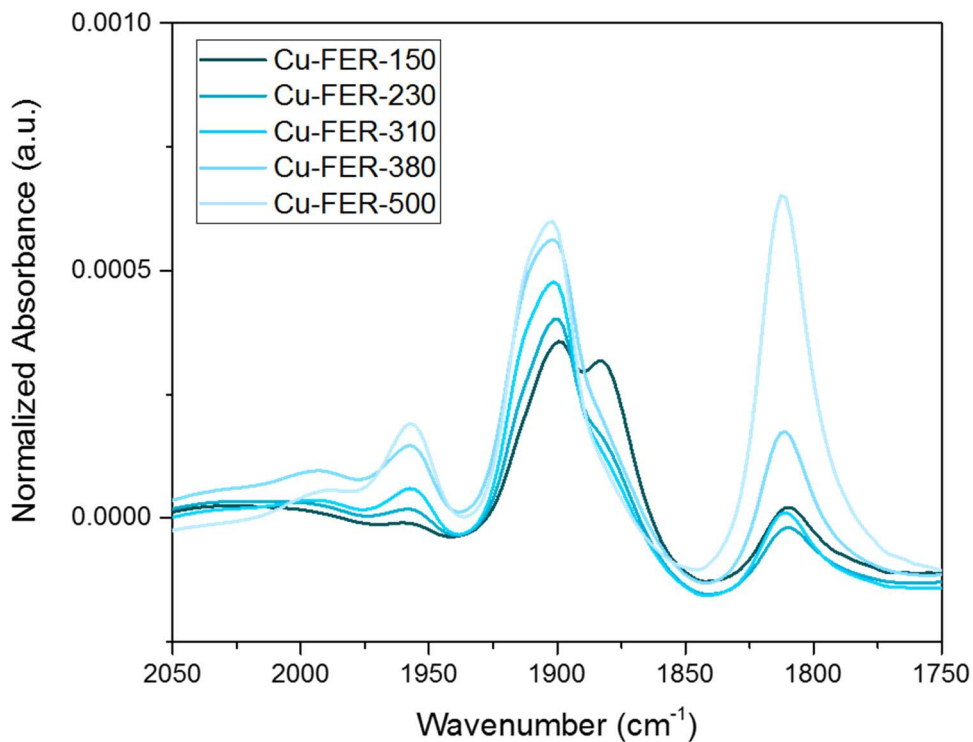| Path	R (Å)	σ^2	CN	ΔE
Cu-O	1.94 (±0.01)	0.006 (±0.001)	3.53 (±0.22)	-5.06 (±0.58)
Cu-Al	2.73 (±0.01)	0.006 (±0.002)	<u>1.19</u>	-"-
Cu-Cu	3.02 (±0.03)	0.010 (±0.003)	<u>0.81</u>	-"-

Figure A 2.1 Differential IR spectra of Cu-FER samples with NO adsorption after activation under vacuum condition
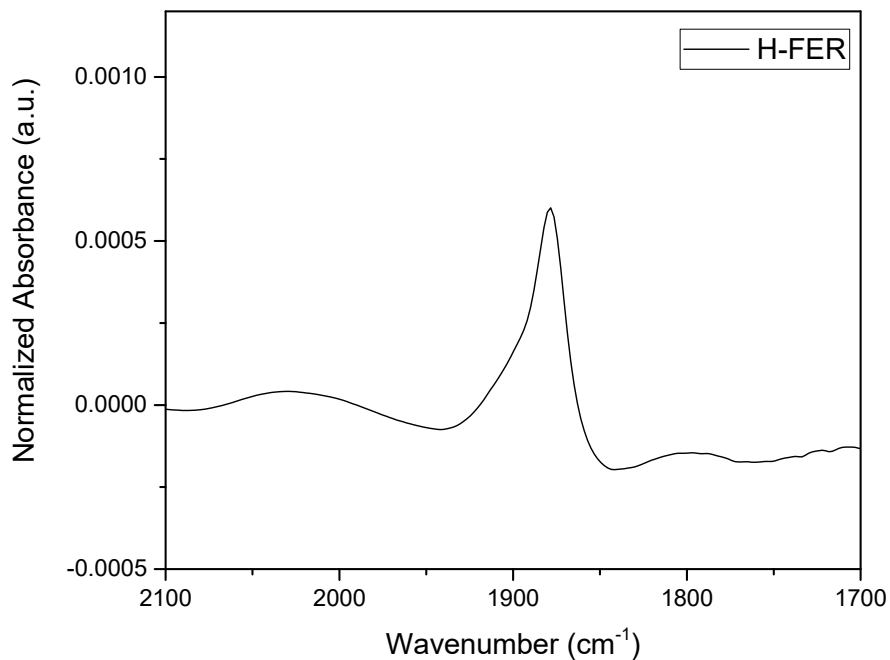

Figure A 2.2 Differential IR spectra of H-FER sample with NO adsorption
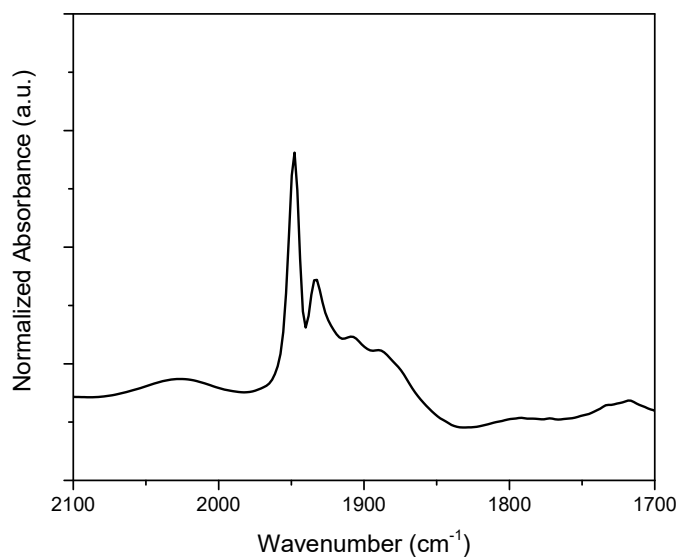
Figure A 2.3 Differential IR spectra of Cu-AEI sample with NO adsorption

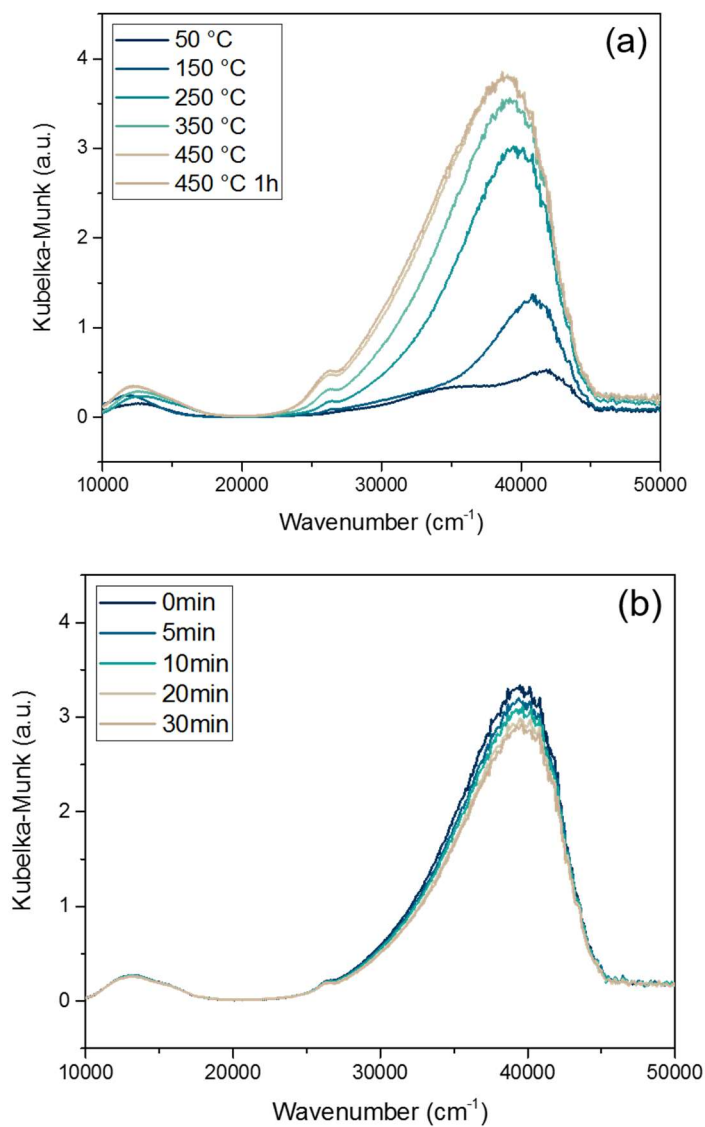**Figure A 2.4** In situ UV-Vis spectra of Cu-FER-151 during (a) activation in oxygen, (b) methane reaction
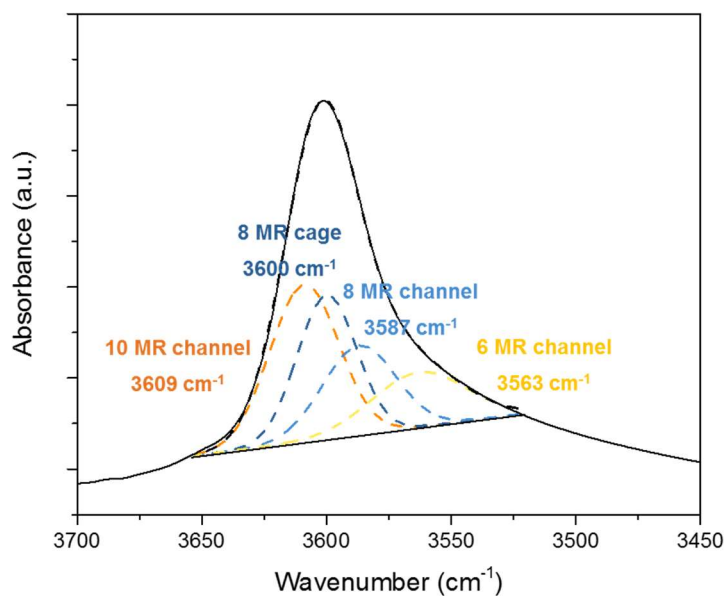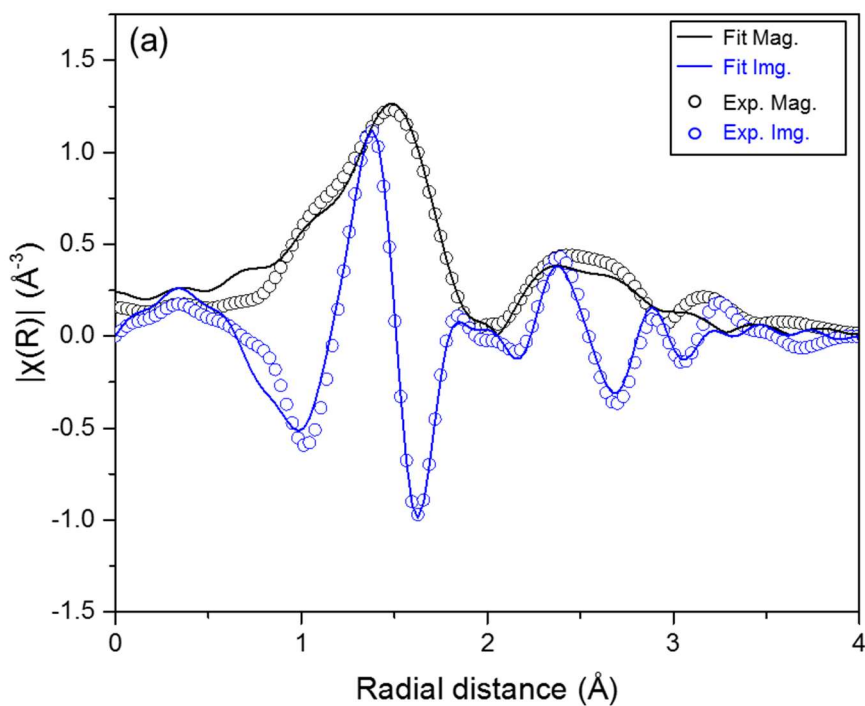

Figure A 2.5 Deconvolution of the O-H bands from Si-OH-Al species in different locations of the FER framework[45]
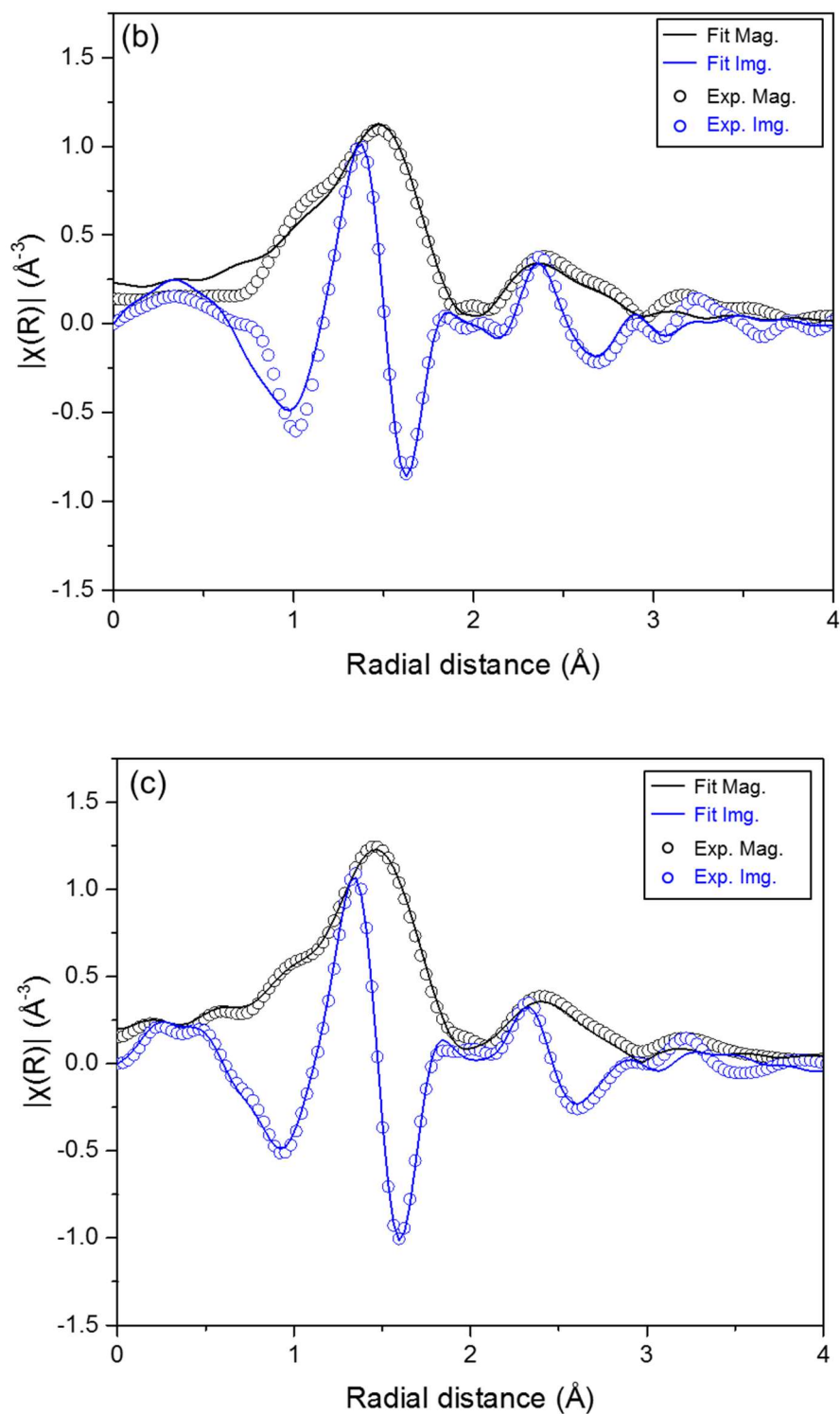
Figure A 2.6 k^2-weighted Cu K-edge Mag[χ(R)] and Img[χ(R)] spectra of (a) Cu-FER-150, (b) Cu-FER-310, and (c) Cu-FER-500 and the corresponding FEFF fits

2.8. References

1.   D. Malakoff, *Science*, **2014**, *344*, 1464.

2.   R. A. Kerr, *Science*, **2010**, *328*, 1624.

3.   A. Caballero and P. J. Perez, *Chem. Soc. Rev.*, **2013**, *42*, 8809-8820.

4.   G. A. Olah, *Angew. Chem. Int. Ed.*, **2005**, *44*, 2636-2639.

5.   R. A. Periana, D. J. Taube, S. Gamble, H. Taube, T. Satoh and H. Fujii, *Science*, **1998**, *280*, 560.

6.   H. Schwarz, *Angew. Chem. Int. Ed.*, **2011**, *50*, 10096-10115.

7.   M. Ravi, M. Ranocchiari and J. A. van Bokhoven, *Angew. Chem. Int. Ed.*, **2017**, *56*, 16464-16483.

8.   L. Tao, I. Lee and M. Sanchez-Sanchez, *Catal. Sci. Technol.*, **2020**, *10*, 7124-7141.

9.   M. Dyballa, K. Thorshaug, D. K. Pappas, E. Borfecchia, K. Kvande, S. Bordiga, G. Berlier, A. Lazzarini, U. Olsbye, P. Beato, S. Svelle and B. Arstad, *ChemCatChem*, **2019**, *11*, 5022-5026.

10.   M. H. Groothaert, P. J. Smeets, B. F. Sels, P. A. Jacobs and R. A. Schoonheydt, *J. Am. Chem. Soc.*, **2005**, *127*, 1394-1395.

11.   J. S. Woertink, P. J. Smeets, M. H. Groothaert, M. A. Vance, B. F. Sels, R. A. Schoonheydt and E. I. Solomon, *Proc. Natl. Acad. Sci.*, **2009**, *106*, 18908-18913.

12.   P. Vanelderen, B. E. Snyder, M. L. Tsai, R. G. Hadt, J. Vancauwenbergh, O. Coussens, R. A. Schoonheydt, B. F. Sels and E. I. Solomon, *J. Am. Chem. Soc.*, **2015**, *137*, 6383-6392.

13.   G. Brezicki, J. D. Kammert, T. B. Gunnoe, C. Paolucci and R. J. Davis, *ACS Catal.*, **2019**, *9*, 5308-5319.

14.   D. K. Pappas, A. Martini, M. Dyballa, K. Kvande, S. Teketel, K. A. Lomachenko, R. Baran, P. Glatzel, B. Arstad, G. Berlier, C. Lamberti, S. Bordiga, U. Olsbye, S. Svelle, P. Beato and E. Borfecchia, *J. Am. Chem. Soc.*, **2018**, *140*, 15270-15278.

15.   E. M. C. Alayon, M. Nachtegaal, A. Bodi, M. Ranocchiari and J. A. van Bokhoven, *Phys. Chem. Chem. Phys.*, **2015**, *17*, 7681-7693.

16.   S. Grundner, W. Luo, M. Sanchez-Sanchez and J. A. Lercher, *Chem. Commun.*, **2016**, *52*, 2553-2556.

17.   S. Grundner, M. A. C. Markovits, G. Li, M. Tromp, E. A. Pidko, E. J. M. Hensen, A. Jentys, M. Sanchez-Sanchez and J. A. Lercher, *Nat. Commun.*, **2015**, *6*, 7546.

18.   T. Ikuno, S. Grundner, A. Jentys, G. Li, E. Pidko, J. Fulton, M. Sanchez-Sanchez and J. A. Lercher, *J. Phys. Chem. C*, **2019**, *123*, 8759-8769.

19.   M. A. C. Markovits, A. Jentys, M. Tromp, M. Sanchez-Sanchez and J. A. Lercher, *Top. Catal.*, **2016**, *59*, 1554-1563.

20.   V. L. Sushkevich and J. A. van Bokhoven, *Catal. Sci. Technol.*, **2018**, *8*, 4141-4150.

21.   J. Zheng, I. Lee, E. Khramenkova, M. Wang, B. Peng, O. Y. Gutiérrez, J. L. Fulton, D. M. Camaioni, R. Khare, A. Jentys, G. L. Haller, E. A. Pidko, M. Sanchez-Sanchez and J. A. Lercher, *Chem. Eur. J.*, **2020**, *26*, 7563-7567.

22.   A. J. Knorpp, A. B. Pinar, C. Baerlocher, L. B. McCusker, N. Casati, M. A. Newton, S. Checchia, J. Meyet, D. Palagin and J. A. van Bokhoven, *Angew. Chem. Int. Ed.*, **2021**, *60*, 5854-5858.

23.   A. J. Knorpp, A. B. Pinar, M. A. Newton, V. L. Sushkevich and J. A. van Bokhoven, *ChemCatChem*, **2018**, *10*, 5593-5596.

24.   B. E. R. Snyder, P. Vanelderen, R. A. Schoonheydt, B. F. Sels and E. I. Solomon, *J. Am. Chem. Soc.*, **2018**, *140*, 9236-9243.

25.   D. K. Pappas, E. Borfecchia, M. Dyballa, K. A. Lomachenko, A. Martini, G. Berlier, B. Arstad, C. Lamberti, S. Bordiga, U. Olsbye, S. Svelle and P. Beato, *ChemCatChem*, **2019**, *11*, 621-627.

26.   D. K. Pappas, E. Borfecchia, K. A. Lomachenko, A. Lazzarini, E. S. Gutterød, M. Dyballa, A. Martini, G. Berlier, S. Bordiga, C. Lamberti, B. Arstad, U. Olsbye, P. Beato and S. Svelle, *Top. Catal.*, **2019**, *62*, 712-723.

27.   D. K. Pappas, E. Borfecchia, M. Dyballa, I. A. Pankin, K. A. Lomachenko, A. Martini, M. Signorile, S. Teketel, B. Arstad, G. Berlier, C. Lamberti, S. Bordiga, U. Olsbye, K. P. Lillerud, S. Svelle and P. Beato, *J. Am. Chem. Soc.*, **2017**, *139*, 14961-14975.

28.   B. Ipek, M. J. Wulfers, H. Kim, F. Göltl, I. Hermans, J. P. Smith, K. S. Booksh, C. M. Brown and R. F. Lobo, *ACS Catal.*, **2017**, *7*, 4291-4303.

29.   M. Dyballa, D. K. Pappas, E. Borfecchia, P. Beato, U. Olsbye, K. P. Lillerud, B. Arstad and S. Svelle, *Microporous Mesoporous Mater.*, **2018**, *265*, 112-122.

30.   V. L. Sushkevich, A. V. Smirnov and J. A. van Bokhoven, *J. Phys. Chem. C*, **2019**, *123*, 9926-9934.

31.   F. Amano, T. Tanaka and T. Funabiki, *J. Mol. Catal. A Chem.*, **2004**, *221*, 89-95.

32.   V. Zdravkova, N. Drenchev, E. Ivanova, M. Mihaylov and K. Hadjiivanov, *J. Phys. Chem. C*, **2015**, *119*, 15292-15302.

33.   A. Penkova, K. Hadjiivanov, M. Mihaylov, M. Daturi, J. Saussey and J. C. Lavalley, *Langmuir*, **2004**, *20*, 5425-5431.

34.   J. Valyon and W. K. Hall, *J. Phys. Chem.*, **1993**, *97*, 1204-1212.

35.   P. Xie, T. Pu, G. Aranovich, J. Guo, M. Donohue, A. Kulkarni and C. Wang, *Nat. Catal.*, **2021**, *4*, 144-156.

36.   V. L. Sushkevich, D. Palagin and J. A. van Bokhoven, *Angew. Chem. Int. Ed.*, **2018**, *57*, 8906-8910.

37.   V. L. Sushkevich, M. Artsiusheuski, D. Klose, G. Jeschke and J. A. van Bokhoven, *Angew. Chem. Int. Ed.*, **2021**, *60*, 15944-15953.

38.   V. L. Sushkevich and J. A. van Bokhoven, *ACS Catal.*, **2019**, *9*, 6293-6304.

39.   E. Borfecchia, K. A. Lomachenko, F. Giordanino, H. Falsig, P. Beato, A. V. Soldatov, S. Bordiga and C. Lamberti, *Chem. Sci.*, **2015**, *6*, 548-563.

40.   G. Turnes Palomino, P. Fisicaro, S. Bordiga, A. Zecchina, E. Giamello and C. Lamberti, *J. Phys. Chem. B*, **2000**, *104*, 4064-4073.

41.   F. Giordanino, P. N. Vennestrom, L. F. Lundegaard, F. N. Stappen, S. Mossin, P. Beato, S. Bordiga and C. Lamberti, *Dalton Trans.*, **2013**, *42*, 12741-12761.

42.   R. Oord, J. E. Schmidt and B. M. Weckhuysen, *Catal. Sci. Technol.*, **2018**, *8*, 1028-1038.

43.   H. V. Le, S. Parishan, A. Sagaltchik, C. Göbel, C. Schlesiger, W. Malzer, A. Trunschke, R. Schomäcker and A. Thomas, *ACS Catal.*, **2017**, *7*, 1403-1412.

44.   Y. Kim, T. Y. Kim, H. Lee and J. Yi, *Chem. Commun.*, **2017**, *53*, 4116-4119.

45.   V. L. Zholobenko, D. B. Lukyanov, J. Dwyer and W. J. Smith, *J. Phys. Chem. B*, **1998**, *102*, 2715-2721.

46.   Y. Suzuki, T. Wakihara, K. Itabashi, M. Ogura and T. Okubo, *Top. Catal.*, **2008**, *52*, 67.

47.   Q. Guo, F. Fan, D. A. J. M. Ligthart, G. Li, Z. Feng, E. J. M. Hensen and C. Li, *ChemCatChem*, **2014**, *6*, 634-639.

48. C. Lamberti, A. Zecchina, E. Groppo and S. Bordiga, *Chem. Soc. Rev.*, **2010**, *39*, 4951-5001.

49. M. H. Mahyuddin, A. Staykov, Y. Shiota, M. Miyanishi and K. Yoshizawa, *ACS Catal.*, **2017**, *7*, 3741-3751.

50. M. J. Henson, P. Mukherjee, D. E. Root, T. D. P. Stack and E. I. Solomon, *J. Am. Chem. Soc.*, **1999**, *121*, 10332-10345.

3. Influence of Cu Concentration on Equilibrium of Cu-(Al-)oxo Cluster Speciation in Mordenite for Oxidative Transformations of Methane

3.1. Abstract

Cu-exchanged in a mordenite material rich in extra-framework Al species (Cu-Al-MOR) shows the highest activity per Cu in methane oxidation. The activities of Cu-Al-MOR in methane oxidation and oxidative etherification of methane indicate two speciation regions marked by Cu concentrations. Ab initio thermodynamic analysis and molecular dynamics identified a $[Cu_2AlO_3(OH)]^{2+}$ cluster able to oxidize two methane molecules per cluster at ambient pressure, coexisting with the conventional $[Cu_3O_3]^{2+}$ cluster. The two clusters are shown able to interconvert in the EFAl-rich MOR depending on the concentration of Cu species. The yields derived from the distribution of two clusters are in good agreement with the experimental values for methane oxidation at elevated pressure and oxidative etherification of methane. The Cu L_3-edge XANES and UV-Vis spectra provide experimental evidence in support of the co-presence of two clusters.

3.2. Introduction

The utilization of methane as feedstock for various industrially relevant chemicals has attracted enormous attention, especially with the increasing number of discovered gas reserves around the world.[1-3] Among the different transformation routes, the direct conversion of methane to methanol represents one of the most enticing yet challenging pathways, due to the rather harsh reaction conditions required to overcome the activation barrier of methane, incurring low selectivity towards methanol owing to its higher susceptibility to deep oxidation.[4, 5]

Inspired by the naturally occurring particulate methane monooxygenases (pMMO),[6-9] copper-exchanged zeolites have shown great promise for a highly selective transformation of methane to methanol through a three-stage process that can use oxygen from air as oxidant. Multiple zeolite topologies have been shown to accommodate active cationic Cu-oxo clusters in paired Al sites for the transformation, among which mordenite (MOR) is arguably the most widely studied zeolite. Spectroscopic characterization of these materials has led to different and at times conflicting proposals of the geometry of the active sites in zeolites. Mostly dimeric or trimeric Cu-oxo clusters are shown to be active in Cu-MOR.[10-20] Numerous material and synthesis parameters have been identified as relevant in directing the structure of Cu-oxo clusters, including the presence of other cations in the parent zeolite,[15, 21] the distribution of the framework aluminum[22, 23] and the ion exchange procedure.[11, 24] The ability of Cu-oxo clusters to activate CH_4 also depends on geometry and size of the pores as well as local environment.[12, 22, 25-27]

Recently, the presence of extra-framework Al (EFAl) has been found to increase the activity of Cu-MOR materials.[24, 28] The combination of spectroscopic and computational studies linked the origin of such activity increase to the formation of active Cu-Al-oxo clusters by reaction of the Cu ions with EFAl species located near the bottom of the 8 MR side pockets.[28] The proposed $[Cu_2AlO_3]^{2+}$ cluster has a higher productivity per Cu than clusters formed with only Cu.

In this chapter, we continue to investigate the origin of the high reactivity of Cu-Al-oxo clusters hosted by MOR topology. Studies at a wider range of methane pressures have determined the upper limit of active oxygen atoms that active clusters can utilize to

convert CH_4 into products. We use reaction with ethanol as an alternative way to extract methyl groups generated from CH_4 activation. This strategy constitutes a novel pathway to generate methyl-based ether compounds from CH_4 and, in addition, it yields information on the reactivity and location of the CH_x- surface intermediates. In our study, catalytic tests are combined with ab initio thermodynamic analysis (aiTA), molecular dynamics (MD) and spectroscopic methods including in situ UV-Vis and X-ray absorption. Our analysis reveals a dynamic equilibrium between active Cu-oxo and active Cu-Al-oxo cluster structures, depending on the Cu concentration and availability of EFAl.

3.3. Results and Discussions

3.3.1. Activity performance of Cu-Al-oxo clusters hosted in MOR

In our previous study, we have prepared a highly active Cu-MOR series with a capacity to activate 0.58 molecules of CH_4 per Cu, in a typical three-stage process of selective methane oxidation at 1 bar. This higher Cu efficiency (Cu_{eff}, defined as the molar ratio of converted methane to the total Cu content) is attributed to the formation of highly efficient Al-containing clusters by reaction of exchanged Cu ions with EFAl species entrained in the zeolite pores.[28] On the other hand, it has been shown that Cu-MOR materials can reach significantly higher Cu_{eff} under high methane pressures (ca. 40 bar).[13, 17, 29] This has been attributed to the fact that, at high CH_4 chemical potential, a second oxygen atom from a Cu-oxo active cluster can take part in methane oxidation.[10, 17] In order to determine whether the reactivity of Cu-Al-oxo clusters could be increased at high CH_4 chemical potentials, we tested the activity of an EFAl-containing Cu-MOR series (designated Cu-Al-MOR) at 40 bar and compare it to activity at 1 bar. As shown in Figure 3.1, the total yields achieved at 40 bar of methane pressure increased by at least 10%. However, this increase is significantly smaller than the 100% activity increase that we achieve for Cu-MOR materials containing solely $[Cu_3O_3]^{2+}$ clusters.[16, 17] This catalytic behavior of Cu-Al-MOR series shows in the first place that the effect of CH_4 chemical potential on Cu-Al-oxo clusters are different from (the effect) on $[Cu_3O_3]^{2+}$ clusters. It should be noted that even though Cu-Al-MOR samples with low to medium Cu concentrations have a limited increase of activity (10% - 40%) from 1 bar to 40 bar, the sample with highest Cu loading, and its higher methanol yield correspondingly, showed an increase of nearly 100 %. Such difference is a first indication that the Cu speciation in presence of trapped EFAl might vary in a non-linear manner with Cu concentrations.
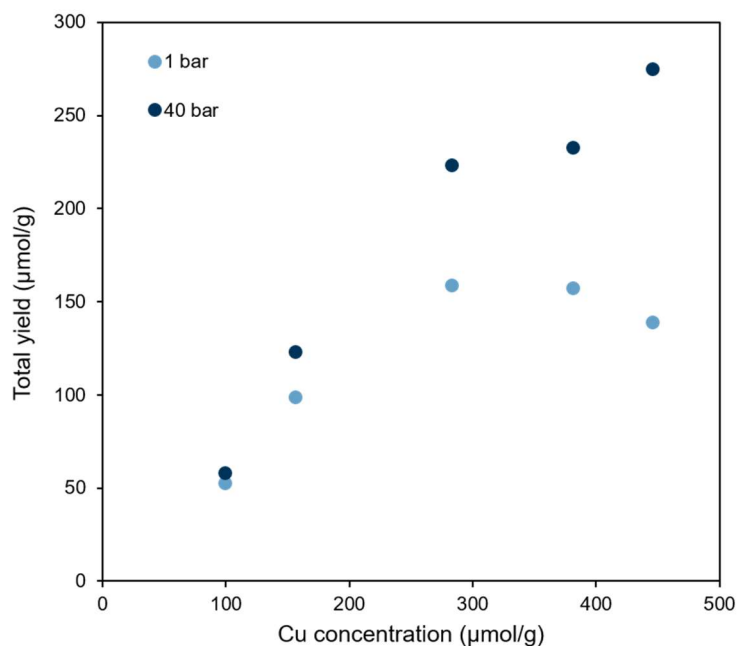
Figure 3.1 Total yields achieved on Cu-Al-MOR series at 1 or 40 bar of methane pressure

Methane-loaded Cu-Al-MOR samples were subjected to a treatment with ethanol instead of water, in order to determine the nature and reactivity of surface activated CH_x groups. In such way, we show that ethyl methyl ether (EME), an important asymmetrical ether, can be produced from methane and ethanol. Figure 3.2(b) shows that EME yield increased monotonically with Cu concentrations up to ca. 380 µmol/g with a 100% selectivity. Interestingly, EME yields are approximately 75% of the total methanol yields up to Cu loadings of 300 µmol/g and then approximately 100% for Cu loadings above 300 µmol/g. Based on this, we speculate that surface intermediates formed at low Cu loadings have different nature or locations, leading to different reactivities with EtOH and H_2O. This observation, in agreement with the activity increase at high CH_4 chemical potentials, indicates that Cu speciation changes with Cu concentration for the Cu-Al-MOR series, unlike Cu-MOR materials in the absence of EFAl where speciation is constant.[16] In particular, our results point to two different Cu speciation regions demarcated by a Cu concentration of ca. 300 µmol/g.
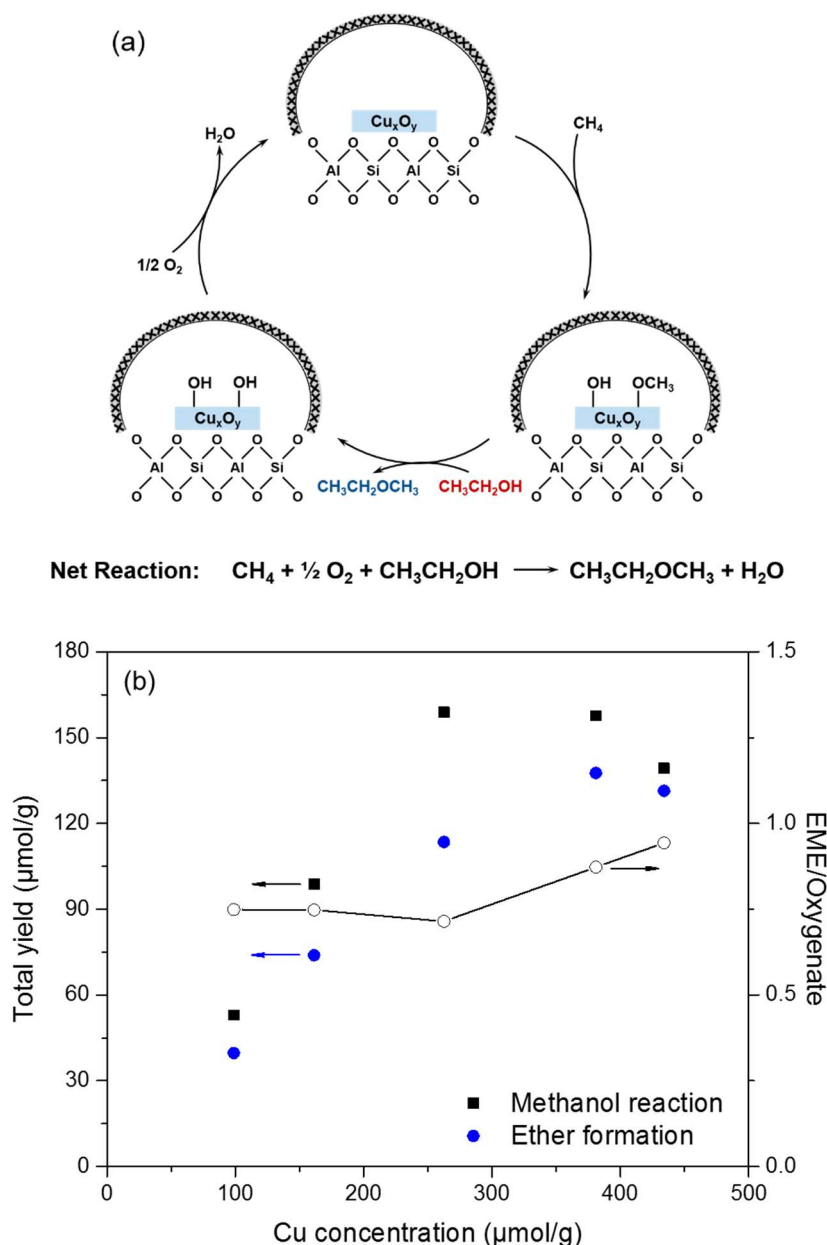
Figure 3.2 (a) Reaction scheme of EME formation from methane and ethanol; (b) EME yields achieved on Cu-Al-MOR series and the ratio if normalized to methanol yields

Based on our previous studies on Cu clusters in MOR, we hypothesize that Cu-Al-MOR materials can accommodate both Cu-Al-oxo and Cu-oxo clusters.[17, 28] Here, we hypothesize that the activity of Cu-Al-MOR materials is the result of the sum of different concentrations of clusters with structures of $[Cu_2AlO_3]^{2+}$[28] and $[Cu_3O_3]^{2+}$,[16] and these concentrations are affected differently by the availability of Cu contents in the system.

A mild increase of activity with CH_4 pressure as seen for low Cu loading samples in Figure 3.1 can be explained by a larger proportion of the $[Cu_2AlO_3]^{2+}$ cluster type, because this cluster has already reached its activity upper limit at 1 bar, with the ability to activate two CH_4 molecules.[28] Conversely, it is known that $[Cu_3O_3]^{2+}$ clusters activate 1 CH_4 molecule at 1 bar[16] and 2 CH_4 molecules at 40 bar.[17] Based on these reaction stoichiometries, and assuming that only these two types of clusters participate in the reaction, the concentrations of the two clusters can be determined from the total Cu contents in each material and the total yields at 1 bar. As shown in Figure 3.3, materials with Cu concentrations below 300 µmol/g contain approximately 50 % of each type of cluster, while at higher Cu concentrations the proportion of $[Cu_3O_3]^{2+}$ significantly increases, at expenses of the $[Cu_2AlO_3]^{2+}$ cluster.
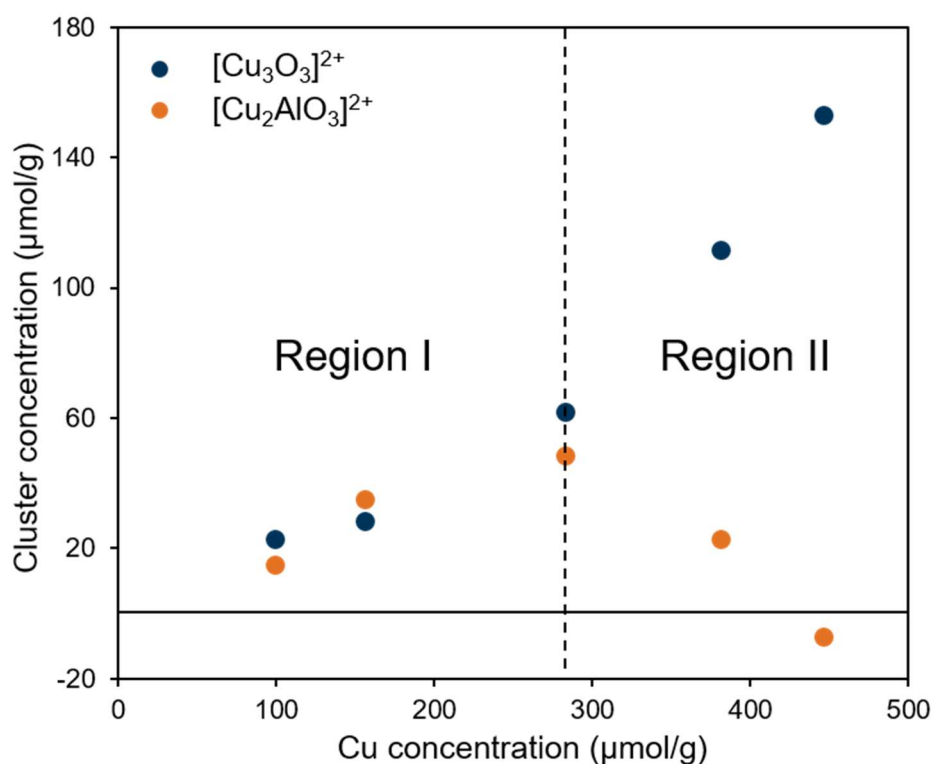

Figure 3.3 The distribution of $[Cu_3O_3]^{2+}$ and $[Cu_2AlO_3]^{2+}$ clusters in Cu-Al-MOR materials

Based on this cluster distribution, the EME results in Figure 3.2 points to a limited reactivity of $[Cu_2AlO_3]^{2+}$ cluster with ethanol. This will be further discussed in the following section.

3.3.2. Ab initio thermodynamics and molecular dynamics predictions on nuclearity and reactivity of active Cu clusters in MOR

To rationalize and theoretically support the experimentally observed concentration dependency, the DFT-based aiTA was conducted to establish the correlation between the thermodynamic stability of the Cu-oxo and Cu-Al-oxo clusters at different Cu concentrations. The stability of the respective models and their potential reactivity towards the sequential activation of several methane molecules were studied utilizing the periodic spin-polarized calculations at the PBE-D3(BJ) level of theory, where active sites were stabilized by the negatively charged aluminum in the side pocket of mordenite.

The pure Cu-oxo species were represented by the $[Cu_3O_3]^{2+}$ trimeric cluster configuration recently determined with the expert bias-free computational procedure.[30] Its aluminum-based counterpart was constructed assuming a Cu_2Al core and overall +2 charge. Two stoichiometries were considered, namely, the $[Cu_2AlO_3]^{2+}$, proposed earlier, and an alternative $[Cu_2AlO_3(OH)]^{2+}$ cation. The formal electronic state of the Cu centers in the latter species appeared to provide a more favorable reactivity for sequential 2-electron oxidation of 2 CH_4 molecules. To determine the most stable geometries of these cationic complexes, an exhaustive configurational search was carried out using the combination of the low-mode molecular dynamics (LMMD) and machine-learning clustering algorithm k-medoids approach.[30-32] (see details on LMMD and Clustering in the Experimental section) The results of this procedure are depicted in Figure 3.4, which presents the structurally distinct geometries of the active sites extracted from the trajectories $[Cu_2AlO_3(OH)]^{2+}$ (a) and $[Cu_2AlO_3]^{2+}$ (b) with their corresponding energies with respect to the initial configurations. The range of structures obtained indicates the variety of structures that can be sampled by using the LMMD method, while the global minima with the respective energies of -0.28 eV for $[Cu_2AlO_3(OH)]^{2+}$ and -0.42 eV for the $[Cu_2AlO_3]^{2+}$ were utilized for further analysis.
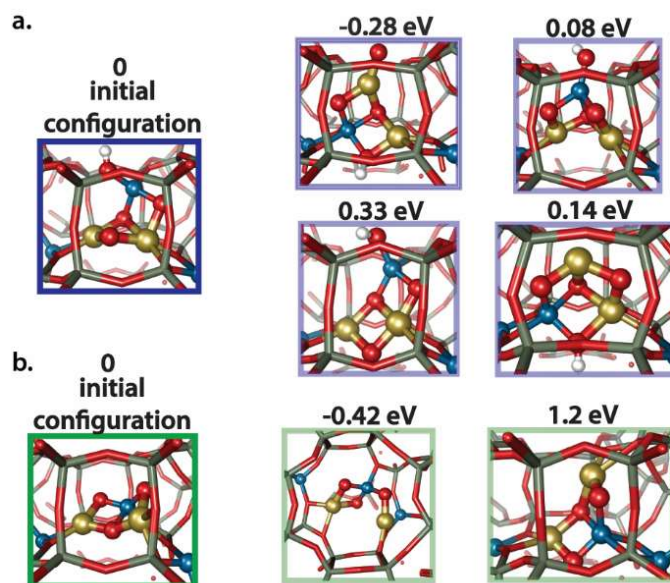
Figure 3.4 The structurally distinct configurations were obtained from the clustering of the $[Cu_2AlO_3(OH)]^{2+}$ (a) and $[Cu_2AlO_3]^{2+}$ (b) LMMD trajectories. The extracted geometries were optimized, with their energies evaluated with respect to the initial configuration. The relative energies are displayed in eV

The thermodynamic limitations of the methane activation on pure trimeric $[Cu_3O_3]^{2+}$/MOR were earlier shown by Zheng et al.[17] Both experimental and theoretical results indicated that the activation of the first methane molecule over a trimer is strongly exergonic at all methane chemical potentials, while the second methane molecule requires elevated pressure (40 bar) for favorable thermodynamics. The intrinsic oxidation reactivity of the low-lying Cu-Al-oxo cationic complexes was assessed by considering the computed Gibbs free energy of their 2-electron reduction and CH_4 oxidation to CH_3OH:

$$Cu_2AlO_n + x \cdot CH_4 \rightarrow Cu_2AlO_{n-x} + x \cdot CH_3OH$$
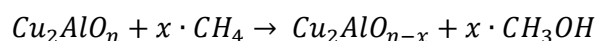
where Cu_2AlO_n is either $[Cu_2AlO_3(OH)]^{2+}$ or $[Cu_2AlO_3]^{2+}$ species, x is the number of oxygen atoms removed from the active sites upon methane oxidation. To simplify the model, here we do not consider the surface intermediates. The Cu_2AlO_{n-x} are the partially reduced extra-framework configurations formed after the sequential methane oxidation and product methanol desorption. Figure 3.5a and b present Gibbs free energy diagrams for the sequential CH_4 oxidation by $[Cu_2AlO_3(OH)]^{2+}$ or $[Cu_2AlO_3]^{2+}$,

respectively. The computational results convincingly demonstrate that the reactivity of the latter is limited to 1 CH_4 oxidation per Cu site, which is in contrast with the experimental observations. However, the alternative hydroxylated cluster $[Cu_2AlO_3(OH)]^{2+}$ can favorably oxidize up to two methane molecules per complex. Furthermore, the aiTA suggests that both oxidation steps are thermodynamically favorable already at near-ambient pressure suggesting its higher reactivity compared to the pure Cu-oxo trimer. We can assume that the formation of the $[Cu_2AlO_3(OH)]^{2+}$ stoichiometry at certain Cu concentrations is responsible for higher reactivity. To support this hypothesis, we have theoretically computed the concentrations of Cu required to form $[Cu_2AlO_3(OH)]^{2+}$ composition at the constant concentration of EFAl species in the system.
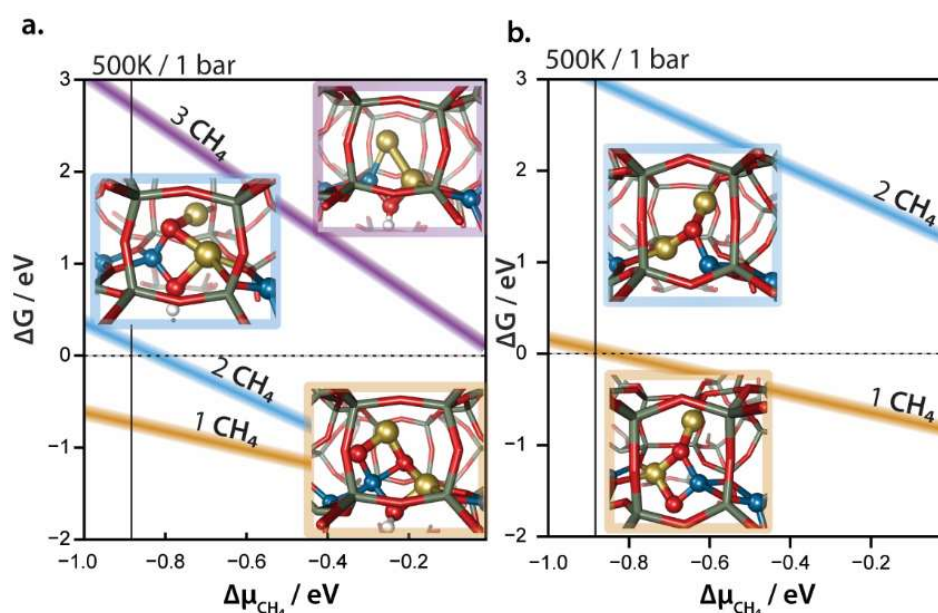

Figure 3.5 The computed Gibbs free energies of the formation of the active site intermediates occur after methane activation and methanol desorption. (a) The thermodynamic favorability of the formation of the intermediates after 1 (yellow line), 2 (blue line) and 3 (purple line) methane molecules activation over $[Cu_2AlO_3(OH)]^{2+}$. (b) The thermodynamic favorability of the formation of the intermediates after 1 (yellow line) and 2 (blue line) methane molecules activation over $[Cu_2AlO_3]^{2+}$

To theoretically analyze the Cu-concentration dependencies of the different extra-framework complexes in MOR zeolite, a new model has been developed and

integrated within the ab initio thermodynamic analysis framework. Conventionally, the aiTA approach operates within the ideal gas approximation, which is not applicable in this case. The new model introduced here treats the extra-framework cations as the defects in the solid-state[33, 34] providing thus a framework for the evaluation of the associated "defect" formation energy and configurational entropy contributions. The stability of the extra-framework cationic ensembles was computed with the reference to bulk CuO, H-MOR and EFAl-containing MOR structures (see details on aiTA in the Experimental section). For the latter, $Al_2O_2^{2+}$, $AlOH^{2+}$ and $Al_2O_4H_4^{2+}$ species at the same 8MR site of MOR were considered as the probable EFAl species in the MOR zeolite.

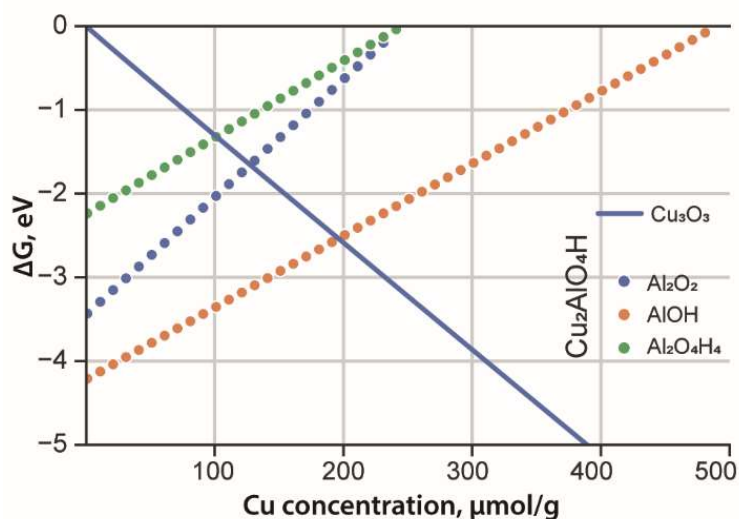**Figure 3.6** The aiTA diagram on the stability of the $[Cu_2AlO_3(OH)]^{2+}$ cluster formed from different Al_2O_2, $AlOH$ and $Al_2O_4H_4$ species (scatter plots) and pure $[Cu_3O_3]^{2+}$ cluster (line plot) as a function of the Cu concentration

Figure 3.6 presents the change of the intrinsic stability of the Cu-Al-oxo ($[Cu_2AlO_3(OH)]^{2+}$) and Cu-oxo ($[Cu_3O_3]^{2+}$) trimer cationic complexes in MOR pores as the function of Cu concentration. At the concentrations of Cu up to 100-200 µmol/g (depending on the assumed EFAl structure), the formation of the Cu-Al-oxo species thermodynamically prevails the formation of the pure Cu-oxo clusters. However, the increase of Cu amount in the catalyst leads to the stabilization of a single Cu-Al-oxo configuration, produced from the mononuclear AlOH species. After this concentration

point, the formation of the $[Cu_3O_3]^{2+}$ becomes more energetically preferred, which correlates with the experimental results in Figure 3, where the Cu-oxo cluster becomes dominating in the concentration range from 200 to 300 µmol/g.

Based on aiTA calculations, that $[Cu_3O_3]^{2+}$ clusters activate 1 CH_4 molecule at 1 bar and 2 CH_4 molecules at 40 bar, and that $[Cu_2AlO_3(OH)]^{2+}$ clusters activate 2 CH_4 molecules already at 1 bar, the concentrations of $[Cu_2AlO_3(OH)]^{2+}$ and $[Cu_3O_3]^{2+}$ clusters determined for the Cu-Al-MOR series as in Figure 3, together with the activity shown at 1 bar, predict well the activity at 40 bar (Figure 3.7). Figure 3.7a shows an excellent correlation between the overall yield achieved experimentally and the yield predicted by the cluster distribution (Figure 3.3), assigning 2 O reactivity to each of the clusters at 40 bar.

Likewise, we have previously induced that, in the case of ethanol scavenging experiments, lower EME yields obtained at low Cu loadings are linked to the Cu-Al-oxo cluster. We hypothesize that the ethanol molecule would only scavenge one of the two activated methane from the $[Cu_2AlO_3(OH)]^{2+}$ cluster on average, while hydrolysis will yield all the two CH_3OH molecules. In that case, both $[Cu_3O_3]^{2+}$ and $[Cu_2AlO_3(OH)]^{2+}$ structures are expected to form one EME molecule per cluster after reaction at 1 bar. We correlated the deduced EME yields based on this assumption with the experimental results and found again a very good fit (Figure 3.7b). These results show that the two-cluster model agrees well with the activity performances in various conditions.
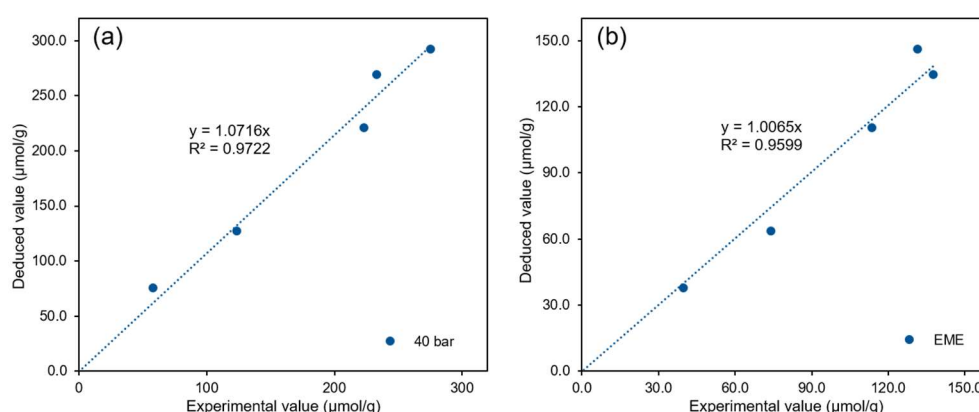

Figure 3.7 (a) Correlation of the methanol yields achieved at 40 bar and the deduced value from the cluster distribution; (b) correlation of the EME yields achieved at 40 bar and the deduced value from the cluster distribution

3.3.3. Spectroscopic evidences on the cluster distributions

In order to support the proposed cluster distribution, we examined the differences observed in the Cu L_3-edge X-ray absorption near edge structure (XANES) of O_2 activated Cu-Al-MOR samples with different Cu loadings. The main peak appearing at 929 eV corresponds to 2p to 3d dipole transitions of Cu(II) species. The position of the satellite feature that arises from the mixing of Cu 3d orbitals with 2p orbitals from the oxygen ligands generally reveals more information on the local chemical environment of the Cu species hosted in each material.[35, 36] While the Cu-Al-MOR-160 and Cu-Al-MOR-280 both show a satellite peak at a ΔE value of 3.5 eV, the satellite feature for Cu-Al-MOR-450 appears at a ΔE value of 3.2 eV (Figure 3.8). In our previous work, the satellite peak for the simulated spectra of both $[Cu_2AlO_3]^{2+}$ homologue and $[Cu_3O_3]^{2+}$ appears at ΔE value of 3.3 eV, while $[Cu_3O_3]^{2+}$ cluster has shown an additional satellite feature at ca. ΔE 2.0 eV. Therefore, we propose that the shift towards lower energies of the satellite peak with increasing Cu loading is indicative of a larger contribution of $[Cu_3O_3]^{2+}$ clusters, in good agreement with the prediction in Figure 3.3.
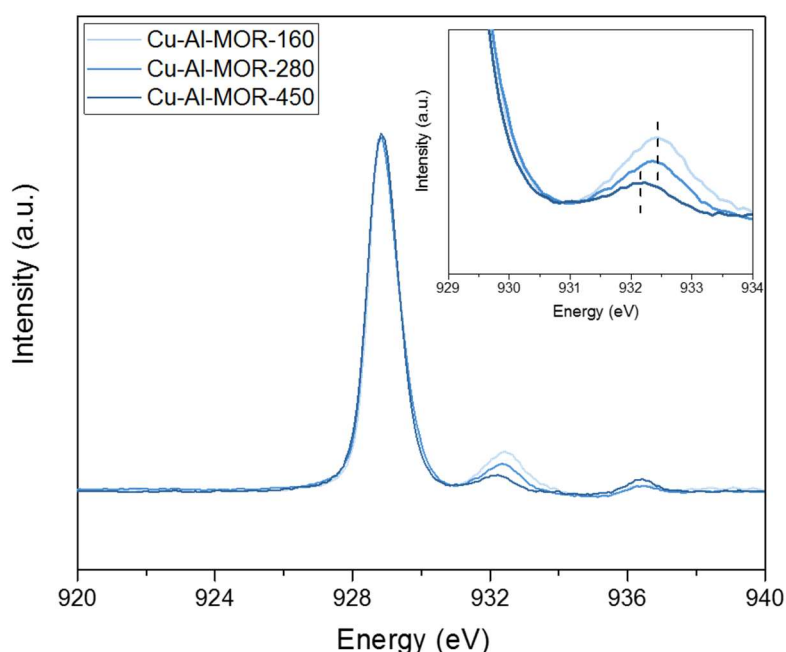

Figure 3.8 Cu L_3-edge XANES of Cu-MOR samples activated in O_2 at 450 °C for 1 h (Intensities of the main edge were made the same for better visualization.)

We also monitor Cu-Al-MOR upon CH_4 exposure by in situ UV-Vis spectroscopy. The differential spectra obtained by subtracting the spectra of the oxygen activated sample show decreases in the absorption bands centered at 29000 and 39000 cm^{-1} (Figure 3.8a and Figure A 3.1), which are attributed to the charge transfer of extra-framework[11, 16, 37] and framework oxygen ligands to Cu species.[38, 39] The relative contribution of these two absorptions changes with Cu loading and CH_4 activation. Correlating the area ratio of both bands with Cu loading shows that the peak ratio remains roughly constant for materials with Cu concentrations below 300 µmol/g, while it increases with Cu concentrations (Figure 3.8b). This correlates with the CH_4 oxidation activity at 1 bar on one hand, and implies a different speciation of Cu in Cu-Al-MOR materials with Cu concentrations above 300 µmol/g, in good agreement with our proposal of cluster distribution in Figure 3.3.
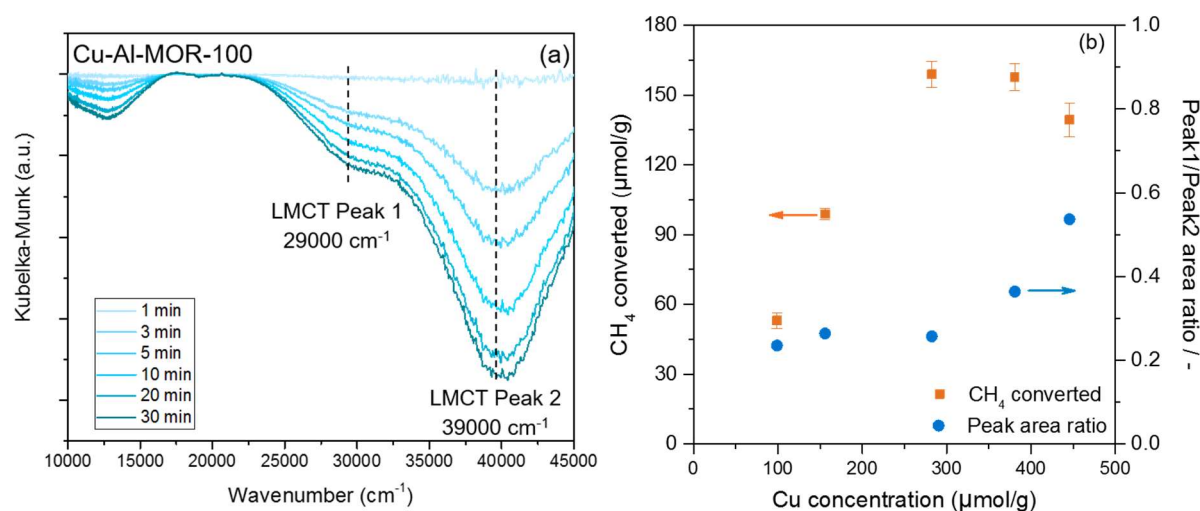

Figure 3.9 In-situ UV-Vis difference spectra of oxygen activated Cu-Al-MOR-100 after to CH_4 exposure at 200 °C for 30 min; (b) the peak area ratio of the decrease of two LMCT bands from UV-vis absorption spectra upon activation of methane at 1 bar as a function of Cu concentration in MOR

3.4. Conclusions

A series of highly active Cu-Al-MOR samples have been tested for the CH_4 oxidation at elevated CH_4 pressure. Their synthetic potential has been expanded further to the preparation of EME by simply replacing the scavenge agent with ethanol. The aiTA combined with MD identified an Al-containing $[Cu_2AlO_3(OH)]^{2+}$ cluster as active in CH_4 oxidation, with up to two CH_4 molecules being oxidized per cluster at 200 °C under 1 bar of CH_4 pressure. A thermodynamic equilibrium has been found between the formation of $[Cu_2AlO_3(OH)]^{2+}$ and $[Cu_3O_3]^{2+}$ clusters as a function of Cu concentrations during the ion exchange with MOR zeolite. Based on activity and total Cu concentration, we have calculated the proportion of each type of Cu-(Al-)oxo cluster formed in MOR with different Cu concentrations. Spectroscopic characterization supported the presence of the two clusters. The role of EFAl has been thus identified, which will hopefully aid the discovery of more reactive Cu-zeolite materials.

3.5. Experimental Section

3.5.1. Preparation of Cu-Al-MOR samples.

Commercial available NH_4-MOR (Si/Al = 10) was purchased from Clariant. The corresponding H-FER was obtained by calcination of NH_4-MOR in synthetic air flow (100 mL/min) at 550°C (10 K/min) for 6 h.

Cu-Al-MOR samples were prepared by aqueous ion exchange of H-MOR with copper acetate solution under controlled conditions.[16] Typically, Cu^{2+}-exchange was carried out by dispersing 2 g of H-MOR at ambient temperature in 120 mL of an aqueous solution of copper acetate (Sigma Aldrich, 99.99%) with desired concentration for 20 h. The pH of the solution was adjusted with aqueous solution of nitric acid (0.2 M) and kept to 5.5 - 6.0 during the Cu-exchange. After the exchange, the sample was separated from the suspension by centrifugation and rinsed four times with double deionized water followed by an intervening centrifugation step after each rinse cycle. The centrifugate was dried at 110 °C for 24 h. All Cu-Al-MOR samples were calcined in synthetic air flow at 500 °C (100 mL/min) for 2 h prior to IR and XAS measurements. The contents of Si, Al, Na and Cu were measured by atomic absorption spectroscopy (AAS) on a UNICAM 939 AA spectrometer after dissolution in boiling hydrofluoric acid.

3.5.2. Testing of activity for selective oxidation of methane.

The activity of the Cu-Al-MOR samples for the selective oxidation of methane to methanol was tested in a three-step reaction scheme. Typically, 50 mg of Cu-Al-MOR (250 - 400 μm) sample was packed in a stainless steel plug flow reactor with a 4-mm inner diameter. First, the sample was activated at 500 °C in O_2 flow for 1 h, cooled down to 200 °C and then flushed with He. In the next step, CH_4 was flowed over the sample at 200 °C for 3 h. Finally, the sample was flushed with He and cooled to 135 °C and subjected by a steam-assisted product desorption with 20 % H_2O in He. Reaction products were identified and quantified with a QMG 220 M1, PrismaPlus (Pfeiffer Vacuum) online MS (mass spectrometer) with a C-SEM detector by monitoring the m/z signals of 31, 44 and 46 for CH_3OH, CO_2 and $(CH_3)_2O$. $(CH_3)_2O$ was considered from the condensation of two CH_3OH molecules and therefore the equivalent. The sum of all detected products was taken as the total yield.

3.5.3. In-situ ultraviolet-visible (UV-Vis) spectroscopy.

The UV-vis spectra were measured on an Avantes AvaSpec 2048 spectrometer equipped with a high-temperature optical fiber (Avantes FCR-7UV400-2ME-HTX). The sample (250 - 400 µm) was placed in a quartz tube with square optical-grade quartz windows. The intensity of the diffuse reflectance UV-vis is shown as the Kubelka-Munk function, defined as $F(R) = (1 - R)^2 / 2R$, where $R = R_s/R_r$, R_s and R_r refer to the signal intensity of the sample and reference, respectively. The reference spectra was taken on the parent H-MOR sample. The samples were first activated in synthetic air (16 mL/min) at 450 °C with a heating rate of 10 K/min for 1 h. Then the samples were cooled down to 200 °C and flushed with He (10 mL/min) for 0.5 h, followed by contact with CH_4 flow (16 mL/min) for 1 h. The spectra were recorded periodically with a certain time interval to monitor the changes through time.

3.5.4. In-situ X-ray absorption spectroscopy.

X-ray absorption spectra at Cu L-edge were measured at the Swiss Light Source (SLS) of the Paul Scherrer Institut (Villigen, Swiss) on PHOENIX II. The photon source is an elliptical undulator and monochromatic light was generated by a planar grating monochromator. Energy calibration was achieved by setting an inflection point of a measured Al-foil to 1559.6 eV. The samples were pressed into self-supporting pellets with a thickness of ca. 0.5 mm and placed into a multi-pellet holder. The samples were first activated in 1 % O_2 in Ar at 800 mbar at 450°C with a heating rate of 10 K/min for 1 h and then cooled down to room temperature. The measurements were performed before and after thermal activation in vacuum (1.0×10^{-4} mbar). All measurements were carried out in fluorescence mode and the incoming I_0 was measured as total electron yield signal taken from a 0.5 µm thin polyester foil coated with 50 nm of Ni. The described I_0 detector was held 1 m upstream of the sample in the beamline vacuum of ca. 10^{-6} mbar. X-ray fluorescence signal was detected by a one-element energy dispersive Silicon drift diode (DSS, manufacturer KeteK, Germany). The introduced gases were further dried by using Supelco 5A Moisture trap. ATHENA software was used during the background processing.

3.5.5. Ab initio low-mode molecular dynamics.

The configurational space of the extra-framework Cu-Al-oxo bimetallic species was sampled using the low-mode molecular dynamics (LMMD) approach by dragging the systems along the low curvature and enhancing the conformational alteration.[30-32] Fully periodic simulations were performed using the CP2K software package with the Quickstep module and orbital transformation.[40-44] The parameters of the mordenite structure were set to: a = b = 13.648, c = 15.015 Å and the Si/Al ratio were set to 23 giving two Al framework species in the model. The generalized gradient approximation (PBE) was used to describe the exchange-correlation energy,[45] with empirical correction by Grimme.[46-48] The periodic Poisson solver in combination with the Goedecker-Teter-Hutter pseudopotentials were used.[49-51] A plane-wave basis set was utilized with a cutoff of 450 Ry and a relative cutoff of 30 Ry; a Gaussian basis set TZV2P-MOLOPT-SR-GTH was used for describing Cu atoms and a TZV2P-MOLOPT-SR-GTH basis set was used for describing Si, Al, O and H atoms. The simulations were running for 5 ps with a time step of 0.5 fs at temperatures of 923 K. and 723 K. The convergence criterion was set to 10e-5 a.u.

3.5.6. Clustering.

A clustering algorithm was used to extract the structurally distinct configurations from the LMMD trajectories.[52] The clustering was utilized based on an unsupervised machine learning algorithm – k-medoids as implemented in scikit-learn.[53] This method minimizes a sum pairwise dissimilarities between structures and centers of the cluster. Every 50th step of each trajectory was included in the clustering procedure and the silhouette index was used for determining the optimal number of clusters.
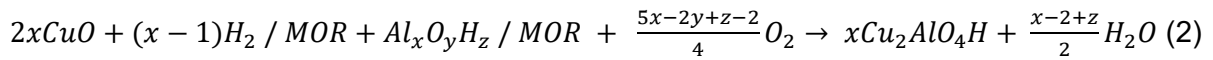
3.5.7. Ab initio thermodynamic analysis.

Ab initio thermodynamic analysis aims to reveal the correlation between the Cu concentrations and Cu-Al-oxo bimetallic cluster occurrence. To investigate the difference in stability of the pure Cu-oxo and Cu-Al-oxo clusters at different Cu concentrations, we have studied the formation of both types of clusters as point defects

as we can not utilize ideal gas approximation for solids. At the fixed (T, p) conditions, the Gibbs free energy change is defined by the value of the defect formation energy and configurational entropy stabilizing the effect:

$$\Delta G = (n\Delta H^f - TS^{conf})/N , \tag{1}$$

where ΔH^f is the formation energy of the defect ($[Cu_2AlO_4H]^{2+}$ or $[Cu_3O_3]^{2+}$) which is obtained directly from the electronic structure calculations and proportional to the number of defects, S^{conf} is a configurational entropy. $n = c^{Cu}N_a$ is the number of defects present in 1 g of catalyst, which can be derived from the experimental concentrations of c^{Cu} in a range of [0, 500] (µmol/g). N is the number of the unit cells calculated for 1 g of catalyst considering the molar weight of the used computational model: $N = 1 \cdot N_a/M(unit\ cell)$. The equilibria and the enthalpy of the $[Cu_2AlO_4H]^{2+}$ formation are defined in (1) and (2):

$$2xCuO + (x-1)H_2 / MOR + Al_xO_yH_z / MOR + \frac{5x-2y+z-2}{4}O_2 \rightarrow xCu_2AlO_4H + \frac{x-2+z}{2}H_2O \tag{2}$$

$$\Delta H^f_{Cu_2AlO_4H} = xCu_2AlO_4H + \frac{x-2+z}{2}H_2O - 2xCuO - (x-1)H_2 / MOR - Al_xO_yH_z / MOR -$$
$$\frac{5x-2y+z-2}{4}O_2 \tag{3}$$

The equilibria and the enthalpy change for a $[Cu_3O_3]^{2+}$ cluster can be expressed as follows:

$$3CuO + H_2 / MOR + 0.5O_2 \rightarrow Cu_3O_3 + H_2O \tag{4}$$

$$\Delta H^f_{Cu_3O_3} = Cu_3O_3 + H_2O - 3CuO - H_2 / MOR - 0.5O_2 \tag{6}$$

where $Al_xO_yH_z$ is the extra-framework species amongst AlOH, Al_2O_2, $Al_2O_4H_4$ and H_2O, CuO, H_2/MOR are the electronic energies of water, copper oxide and parent mordenite.

The configurational entropy, which results from the disorder caused by the defects, can be written as

$$S^{conf} = k_b \ln\frac{(N+n)!}{N!n!} \tag{7}$$

Applying the Stirling formula for n, N values >> 1, $(lnN! = NLnN - N)$ which gives

$$S^{conf} = k_b N \left[\ln\left(1 + \frac{n}{N}\right) + \frac{n}{N}\ln\left(1 + \frac{N}{n}\right)\right] \tag{8}$$

The configurational entropy change for the $[Cu_3O_3]^{2+}$ can be expressed as dependent on the experimental concentration of the Cu via the equation: $n = c^{Cu}N_a$. Therefore, the final expression for the Gibbs free energy change for the $[Cu_2AlO_4H]^{2+}$ combines the eq.(6, 8) and gives:

$$\Delta G_{Cu_3O_3} = \left(\Delta H^f_{Cu_3O_3}(c^{Cu}N_a) - T\left(k_bN\left[\ln\left(1 + \frac{c^{Cu}N_a}{N}\right) + \frac{c^{Cu}N_a}{N}\ln\left(1 + \frac{N}{c^{Cu}N_a}\right)\right]\right)\right)/N$$

Assuming that the Gibbs free energy of the $[Cu_2AlO_4H]^{2+}$ formation depends not only on the concentration of Cu ions but also on the concentration of extra-framework aluminum species, the number of defects per gram of catalyst was defined as $n = \frac{1}{x} \cdot c^{Al}N_a - c^{Cu}N_a$, where the coefficient x reflects the number of Al in the extra-framework aluminum species, that are involved in the formation of a defect. The concentration of the EFAl (c^{Al}) was taken from the experimental results on the total amount of LAS that equals 490 µmol/g. The final equation for the Gibbs free energy of $[Cu_2AlO_4H]^{2+}$ formation in the presence of various EFAl species can be expressed as:

$$\Delta G_{Cu_2AlO_4H} = \left(\Delta H^f_{Cu_2Al\ _4H}\left(\frac{1}{x} \cdot c^{Al}N_a - c^{Cu}N_a\right)\right.$$

$$- T\left(k_bN\left[\ln\left(1 + \frac{\frac{1}{x} \cdot c^{Al}N_a - c^{Cu}N_a}{N}\right) + \frac{\frac{1}{x} \cdot c^{Al}N_a - c^{Cu}N_a}{N}\ln(1\right.\right.$$

$$\left.\left.\left. + \frac{N}{\frac{1}{x} \cdot c^{Al}N_a - c^{Cu}N_a}\right)\right]\right)\right)/N$$

3.6. Acknowledgements

3.7. Appendix

Table A 3.1 Physicochemical properties of Cu-FER samples

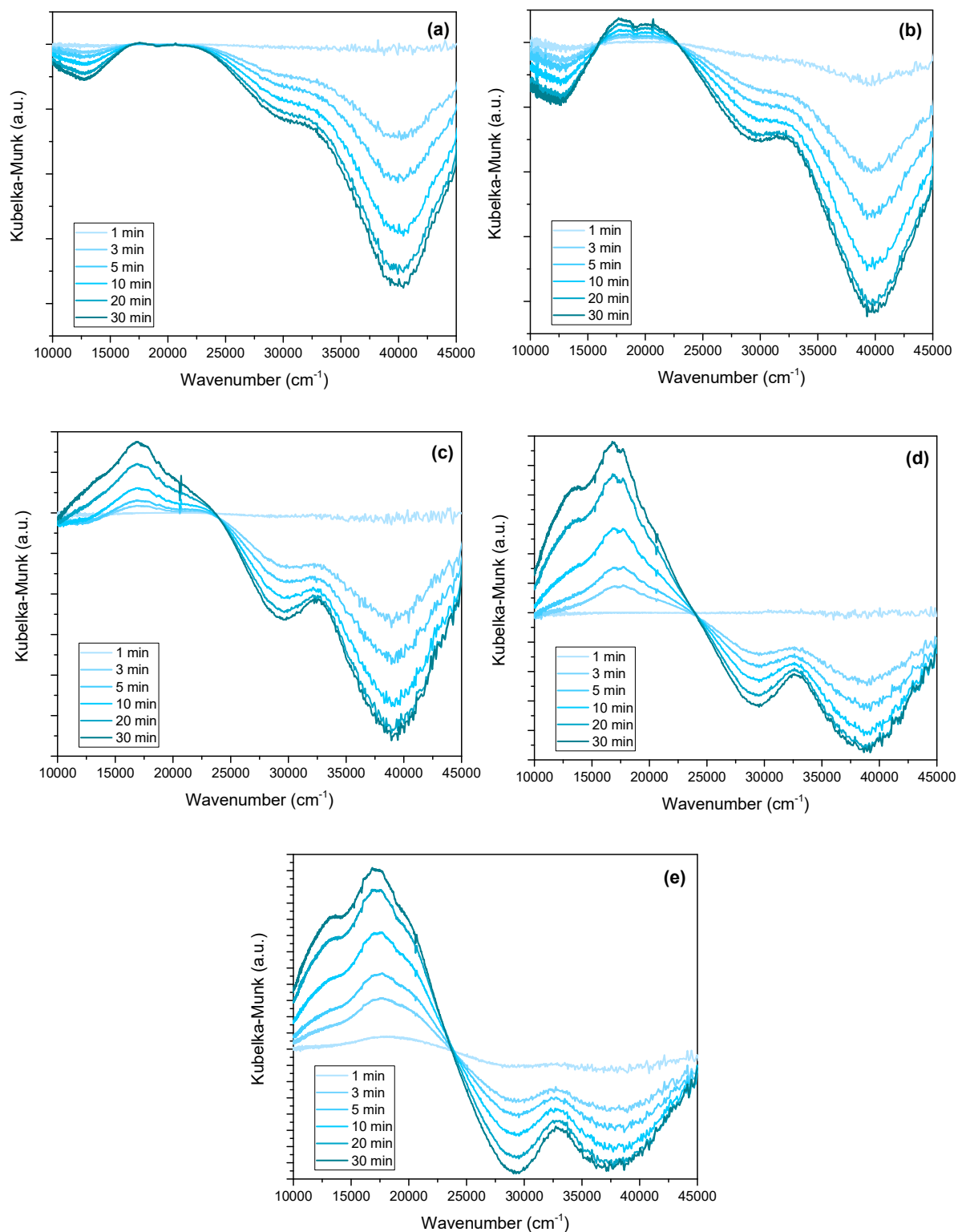| Sample	Cu conc. (µmol/g)	Si/Al after Cu exchange (-)	Cu conc. after Na back-exchange (µmol/g)	Not back-exchanged Cu (%)
Cu-Al-MOR-100	99	9.6	6.3	6.4
Cu-Al-MOR-160	155	9.4	10	6.4
Cu-Al-MOR-280	283	9.3	20	7.0
Cu-Al-MOR-380	381	10.2	25	6.6
Cu-Al-MOR-450	446	9.4	32	7.1

Figure A 3.1. In-situ UV-Vis difference spectra of oxygen activated (a) Cu-Al-MOR-100; (b) Cu-Al-MOR-160; (c) Cu-Al-MOR-280; (d) Cu-Al-MOR-380; (e) Cu-Al-MOR-450 after exposure to CH_4 flow at 200 °C for 30 min

3.8. References

1. D. Malakoff, *Science*, **2014**, *344*, 1464.

2. R. A. Kerr, *Science*, **2010**, *328*, 1624.

3. A. Caballero and P. J. Perez, *Chem. Soc. Rev.*, **2013**, *42*, 8809-8820.

4. R. A. Periana, D. J. Taube, S. Gamble, H. Taube, T. Satoh and H. Fujii, *Science*, **1998**, *280*, 560.

5. H. Schwarz, *Angew. Chem. Int. Ed.*, **2011**, *50*, 10096-10115.

6. A. C. Rosenzweig, *Handbook of Metalloproteins*, **2004**, DOI: https://doi.org/10.1002/0470028637.met232.

7. M. O. Ross and A. C. Rosenzweig, *J. Biol. Inorg. Chem.*, **2017**, *22*, 307-319.

8. M. H. Sazinsky and S. J. Lippard, in *Sustaining Life on Planet Earth: Metalloenzymes Mastering Dioxygen and Other Chewy Gases*, eds. P. M. H. Kroneck and M. E. Sosa Torres, Springer International Publishing, Cham, 2015, DOI: 10.1007/978-3-319-12415-5_6, pp. 205-256.

9. E. I. Solomon, D. E. Heppner, E. M. Johnston, J. W. Ginsbach, J. Cirera, M. Qayyum, M. T. Kieber-Emmons, C. H. Kjaergaard, R. G. Hadt and L. Tian, *Chem. Rev.*, **2014**, *114*, 3659-3853.

10. M. H. Mahyuddin, T. Tanaka, Y. Shiota, A. Staykov and K. Yoshizawa, *ACS Catal.*, **2018**, *8*, 1500-1509.

11. H. V. Le, S. Parishan, A. Sagaltchik, C. Göbel, C. Schlesiger, W. Malzer, A. Trunschke, R. Schomäcker and A. Thomas, *ACS Catal.*, **2017**, *7*, 1403-1412.

12. B. E. R. Snyder, P. Vanelderen, R. A. Schoonheydt, B. F. Sels and E. I. Solomon, *J. Am. Chem. Soc.*, **2018**, *140*, 9236-9243.

13. G. Brezicki, J. D. Kammert, T. B. Gunnoe, C. Paolucci and R. J. Davis, *ACS Catal.*, **2019**, *9*, 5308-5319.

14. D. K. Pappas, A. Martini, M. Dyballa, K. Kvande, S. Teketel, K. A. Lomachenko, R. Baran, P. Glatzel, B. Arstad, G. Berlier, C. Lamberti, S. Bordiga, U. Olsbye, S. Svelle, P. Beato and E. Borfecchia, *J. Am. Chem. Soc.*, **2018**, *140*, 15270-15278.

15. S. Grundner, W. Luo, M. Sanchez-Sanchez and J. A. Lercher, *Chem. Commun.*, **2016**, *52*, 2553-2556.

16.   S. Grundner, M. A. C. Markovits, G. Li, M. Tromp, E. A. Pidko, E. J. M. Hensen, A. Jentys, M. Sanchez-Sanchez and J. A. Lercher, *Nat. Commun.*, **2015**, *6*, 7546.

17.   J. Zheng, I. Lee, E. Khramenkova, M. Wang, B. Peng, O. Y. Gutiérrez, J. L. Fulton, D. M. Camaioni, R. Khare, A. Jentys, G. L. Haller, E. A. Pidko, M. Sanchez-Sanchez and J. A. Lercher, *Chem. Eur. J.*, **2020**, *26*, 7563-7567.

18.   K. D. Vogiatzis, G. Li, E. J. M. Hensen, L. Gagliardi and E. A. Pidko, *J. Phys. Chem. C*, **2017**, *121*, 22295-22302.

19.   N. K. Dandu, J. A. Reed and S. O. Odoh, *J. Phys. Chem. C*, **2018**, *122*, 1024-1036.

20.   V. L. Sushkevich, D. Palagin, M. Ranocchiari and J. A. van Bokhoven, *Science*, **2017**, *356*, 523.

21.   V. L. Sushkevich and J. A. van Bokhoven, *Catal. Sci. Technol.*, **2018**, *8*, 4141-4150.

22.   M. A. C. Markovits, A. Jentys, M. Tromp, M. Sanchez-Sanchez and J. A. Lercher, *Top. Catal.*, **2016**, *59*, 1554-1563.

23.   D. K. Pappas, E. Borfecchia, M. Dyballa, I. A. Pankin, K. A. Lomachenko, A. Martini, M. Signorile, S. Teketel, B. Arstad, G. Berlier, C. Lamberti, S. Bordiga, U. Olsbye, K. P. Lillerud, S. Svelle and P. Beato, *J. Am. Chem. Soc.*, **2017**, *139*, 14961-14975.

24.   M. Dyballa, D. K. Pappas, K. Kvande, E. Borfecchia, B. Arstad, P. Beato, U. Olsbye and S. Svelle, *ACS Catal.*, **2019**, *9*, 365-375.

25.   L. Tao, I. Lee and M. Sanchez-Sanchez, *Catal. Sci. Technol.*, **2020**, *10*, 7124-7141.

26.   M. H. Mahyuddin, A. Staykov, Y. Shiota, M. Miyanishi and K. Yoshizawa, *ACS Catal.*, **2017**, *7*, 3741-3751.

27.   M. A. Newton, A. J. Knorpp, V. L. Sushkevich, D. Palagin and J. A. van Bokhoven, *Chem. Soc. Rev.*, **2020**, *49*, 1449-1486.

28.   I. Lee, M.-S. Lee, L. Tao, T. Ikuno, R. Khare, A. Jentys, T. Huthwelker, C. N. Borca, A. Kalinko, O. Y. Gutiérrez, N. Govind, J. L. Fulton, J. Z. Hu, V.-A. Glezakou, R. Rousseau, M. Sanchez-Sanchez and J. A. Lercher, *JACS Au*, **2021**, *1*, 1412-1421.

29. P. Tomkins, A. Mansouri, S. E. Bozbag, F. Krumeich, M. B. Park, E. M. Alayon, M. Ranocchiari and J. A. van Bokhoven, *Angew. Chem. Int. Ed.*, **2016**, *55*, 5467-5471.

30. E. V. Khramenkova, M. G. Medvedev, G. Li and E. A. Pidko, *J. Phys. Chem. Lett.*, **2021**, *12*, 10906-10913.

31. M. G. Medvedev, M. V. Panova, G. G. Chilov, I. S. Bushmarinov, F. N. Novikov, O. V. Stroganov, A. A. Zeifman and I. V. Svitanko, *Mendeleev Commun.*, **2017**, *27*, 224-227.

32. M. G. Medvedev, A. A. Zeifman, F. N. Novikov, I. S. Bushmarinov, O. V. Stroganov, I. Y. Titov, G. G. Chilov and I. V. Svitanko, *J. Am. Chem. Soc.*, **2017**, *139*, 3942-3945.

33. C. Sutton and S. V. Levchenko, *Front. Chem.*, **2020**, *8*, 757.

34. L. Bukonte, T. Ahlgren and K. Heinola, *J. Appl. Phys.*, **2017**, *121*, 045102.

35. M. F. Qayyum, R. Sarangi, K. Fujisawa, T. D. P. Stack, K. D. Karlin, K. O. Hodgson, B. Hedman and E. I. Solomon, *J. Am. Chem. Soc.*, **2013**, *135*, 17417-17431.

36. R. Sarangi, N. Aboelella, K. Fujisawa, W. B. Tolman, B. Hedman, K. O. Hodgson and E. I. Solomon, *J. Am. Chem. Soc.*, **2006**, *128*, 8286-8296.

37. M. J. Wulfers, S. Teketel, B. Ipek and R. F. Lobo, *Chem. Commun.*, **2015**, *51*, 4447-4450.

38. F. Giordanino, P. N. Vennestrom, L. F. Lundegaard, F. N. Stappen, S. Mossin, P. Beato, S. Bordiga and C. Lamberti, *Dalton Trans.*, **2013**, *42*, 12741-12761.

39. G. Brezicki, J. Zheng, C. Paolucci, R. Schlögl and R. J. Davis, *ACS Catal.*, **2021**, *11*, 4973-4987.

40. U. Borštnik, J. VandeVondele, V. Weber and J. Hutter, *Parallel Comput.*, **2014**, *40*, 47-58.

41. O. Schütt, P. Messmer, J. Hutter and J. VandeVondele, *Electronic Structure Calculations on Graphics Processing Units*, **2016**, DOI: https://doi.org/10.1002/9781118670712.ch8, 173-190.

42. J. VandeVondele and J. Hutter, *J. Chem. Phys.*, **2003**, *118*, 4365-4369.

43. M. Frigo and S. G. Johnson, *Proc. IEEE*, **2005**, *93*, 216-231.

44. J. Hutter, M. Iannuzzi, F. Schiffmann and J. VandeVondele, *Wiley Interdiscip. Rev. Comput. Mol. Sci.*, **2014**, *4*, 15-25.

45.   J. P. Perdew, K. Burke and M. Ernzerhof, *Phys. Rev. Lett.*, **1996**, *77*, 3865-3868.

46.   S. Grimme, J. Antony, S. Ehrlich and H. Krieg, *J. Chem. Phys.*, **2010**, *132*, 154104.

47.   S. Grimme, S. Ehrlich and L. Goerigk, *J. Comput. Chem.*, **2011**, *32*, 1456-1465.

48.   J. VandeVondele, M. Krack, F. Mohamed, M. Parrinello, T. Chassaing and J. Hutter, *Comput. Phys. Commun.*, **2005**, *167*, 103-128.

49.   M. Krack, *Theor. Chem. Acc.*, **2005**, *114*, 145-152.

50.   S. Goedecker, M. Teter and J. Hutter, *Phys. Rev. B*, **1996**, *54*, 1703-1710.

51.   C. Hartwigsen, S. Goedecker and J. Hutter, *Phys. Rev. B*, **1998**, *58*, 3641-3662.

52.   H.-S. Park and C.-H. Jun, *Expert Syst. Appl.*, **2009**, *36*, 3336-3341.

53.   F. Pedregosa, G. Varoquaux, A. Gramfort, V. Michel, B. Thirion, O. Grisel, M. Blondel, P. Prettenhofer, R. Weiss, V. Dubourg, J. Vanderplas, A. Passos, D. Cournapeau, M. Brucher, M. Perrot and É. Duchesnay, *J. Mach. Learn. Res.*, **2011**, *12*, 2825–2830.

4. Activity Enhancement from Formation of Cu-Al-oxo Clusters in FER via Mild Steaming

4.1. Abstract

Steaming is a most common way of adjusting the Al content and generating extra-framework (EFAl) species in zeolite materials. The presence of EFAl in zeolite have been recently shown to induce the formation of Cu-Al-oxo clusters that efficiently convert methane into methanol at ambient pressure. In this study, we demonstrate that an optimized mild steaming protocol can enhance the activity performance of Cu-exchanged FER materials. The structural changes led by mild steaming are studied by IR spectroscopy. Probing the materials with NO adsorption hints at the formation of $[Cu_2AlO_3(OH)]^{2+}$ clusters as a result of the reaction of EFAl species (in form of AlO(OH)) and active $[Cu_2O_2]^{2+}$ clusters in FER. The proposal is supported by in-situ UV-Vis spectroscopy measurements. The co-existence of $[Cu_2AlO_3(OH)]^{2+}$ and $[Cu_2O_2]^{2+}$ clusters is responsible for the activity performance observed for different methane pressures.

4.2. Introduction

Over the past decade, much research spotlight has been focused on Cu-exchanged zeolite materials since the discovery of their outstanding selectivity for the selective oxidation of methane to methanol.[1] Tremendous efforts have been made so far to resolve the actual structures of the active Cu clusters hosted in the zeolite frameworks.[2-4] Despite all these endeavors, the formation and speciation of active Cu clusters are still only partially understood. The existing studies showed that only particular Cu-oxo clusters structures are relevant to catalysis and their formation depends on the convoluted effect of various contributing factors related to the hosting materials.[2, 5, 6] Furthermore, the ubiquitous presence of spectator species also interferes with the identification of active species.[5]

The zeolite topology is widely considered the dominating determinant on the Cu speciation.[2] There are, however, increasing experimental evidences that point to the possibility of forming different Cu clusters in the same type of zeolite framework depending on other synthesis parameters and material properties. The most noticeable example is Cu-exchanged mordenite (Cu-MOR), for which the propositions of dimeric[7-12] or trimeric[7, 8, 13-17] Cu-oxo clusters are almost equally prevalent. A more recent study also shows that port sizes of the parent MOR can also lead to different reactivities of the exchanged Cu species.[18] This leads to a critical assessment of other important properties in the hosting materials that potentially shape the formation of active clusters.[14, 19] In this regard, the active role of extra-framework aluminum (EFAl) species has been recently highlighted by several studies.[20, 21] Dyballa et al. found a strong tie between more active Cu-MOR materials and higher populations of EFAl.[20] More recently, Lee et al. reported a highly active Cu-MOR series, in which the formation of Cu-Al-oxo clusters was proposed from a direct interaction of EFAl with exchanged Cu species.[21] Despite all studies hitherto focusing exclusively on Cu-MOR, it is reasonable to presume that the positive role of EFAl in formation of intrinsically more active Cu species could be also found in other zeolite frameworks.

Steaming is a conventional way of adjusting the Al content and generating EFAl species in zeolite via inducing dealumination at certain T-sites through hydrolysis.[22] By tuning the steaming conditions, the dealumination can happen to a certain extent

without undermining the overall zeolite structure.[23, 24] Based on these leads, we developed a mild steaming approach in order to generate moderate concentrations of EFAl within the pores of a FER material. In Chapter 2, we have shown that the pristine FER generates $[Cu_2O_2]^{2+}$ active clusters in 50-55 % upon ion exchange, and these active clusters co-exist with a 45-50 % of Cu in inactive structures. In this chapter, we investigate the effect of mild steaming on the activity of Cu-FER samples for selective methane oxidation. With in situ spectroscopic studies, we aim to observe the changes introduced in zeolite structure after mild steaming and connect them to the changes in Cu speciation. To gain more information on the structure of the exchanged Cu species, the steamed samples are probed with NO adsorption. This allows identifying the interaction of Cu with the EFAl generated by steaming and determining the structure of the Cu-(Al)-oxo active species.

4.3. Results and Discussions

4.3.1. Optimization of the steaming conditions

The Cu-FER series investigated in this work was prepared via a pH-adjusted ion-exchange procedure that hinders the formation of CuO_x precipitates (Table A 4.1).[13] The Cu speciation and activity performance in a typical three-stage methane oxidation were well studied in Chapter 2. To initiate our study, we chose a middle Cu-loading sample (Cu-FER-310) and subject it to steaming. It should be noted that steaming of a metal-exchanged zeolite usually generates less EFAl than steaming the H-form. In a way, the exchanged Cu ions protect some of the Al T-sites from being detached from the framework. We note that steaming on H-FER resulted in difficulty on Cu ion exchange, likely due to the higher lability of Al pairs in H-form zeolites leading to a significantly lower concentration of exchange sites for the formation of active multinuclear Cu clusters and/or the generation of relatively large concentrations of EFAl hampering the diffusion of species during ion exchange.[20, 25, 26]

We started with subjecting the sample to a 10% H_2O/He flow at 500 °C for 1 h (Figure 4.1a, condition 1). The subsequent activity test showed an increase of overall yield from 53.3 to 71.8 µmol/g compared to the untreated counterpart, corresponding to a net increase of nearly 35%. Repetitive reaction cycles proved that the activity enhancement was stable for at least 5 reaction cycles (Figure A 4.1). Taking into account that in every reaction cycle we have determined the stoichiometric amount of CH_4 reacted on this material, the prominent increase in methanol yields is a clear sign of the existence of a larger concentration of active Cu-oxo bridges. This indicates that a structural transformation from an inactive structure into an active one has taken place. Alternatively, the increase of yields can also be the result of the formation of an active cluster with a larger number of active oxygen species per Cu. An extension of steaming time from one to two hours did not lead to any further increase in activity (Figure 4.1a, condition 2), indicating the transformation in structure already reached its thermodynamic equilibrium after one hour. In the next step, we went on to investigate the optimal steaming temperature. As shown in Figure 4.1b, starting from 300 °C the mild steaming already resulted in an activity increment of 17%, which means a significant fraction of Cu species already went through the structural transformation.

The overall yields increased monotonically with steaming temperature up to 500 °C and leveled off with higher temperature. This allowed us to conclude that the formation of active species in a steamed material has reached its thermodynamic equilibrium at 500 °C after one hour.

Interestingly, if the mild steaming procedure was applied to a sample that had already went through a complete reaction cycle (Figure 4.1a, condition 3), no increase in activity could be observed in the following reaction cycle. Likewise, if 10% O_2 was introduced alongside the steam during the treatment (Figure 4.1a, condition 4), the steamed sample did not show any increased activity. These experimental evidences pointed to the fact that the generation of highly active sites takes place in non-oxidative atmospheres on a fresh sample (that is, a sample that was never exposed to any thermal treatment at high temperature (> 100 °C)). Previously, it was shown that the mobility of Cu(I) generated during autoreduction is essential in the process of reorganization of Cu species.[27-29] This species is formed by auto-reduction of Cu(II) species (attached by active oxygen ligands), which typically happens at high temperature under non oxidative atmosphere.[30, 31] The presence of O_2 in thermal treatments partially inhibits the formation of Cu(I), so we envision that a high population of Cu(I) generated during mild steaming is indispensable for the formation of Cu species leading to higher activity. Moreover, the reaction behavior of the sample appeared to be established in the first thermodynamic equilibrium. Once the reorganization of Cu species happened at high temperature (regardless of steaming or reaction), the overall activity would already be determined and not scrambled again from the subsequent reaction steps.
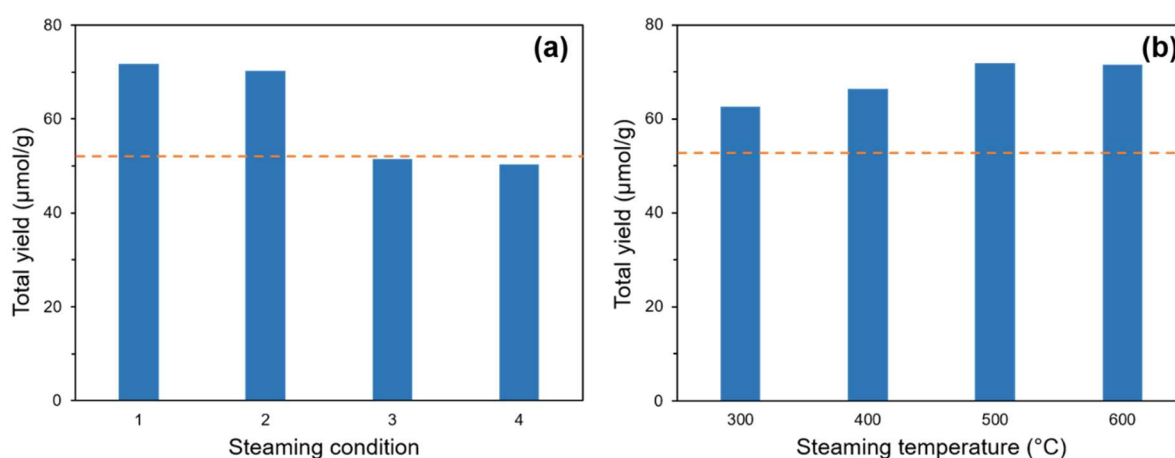
Figure 4.1 (a) Activity measured for samples after treatment in different steaming conditions (condition 1: steaming at 500 °C in 10% H_2O/He for 1 h; condition 2: steaming at 500 °C in 10% H_2O/He for 2 h; condition 3: steaming at 500 °C in 10% H_2O/He for 1 h after one standard reaction cycle; condition 4: steaming at 500 °C in 10% H_2O/10% O_2/He for 1 h); (b) activity measured for samples after steaming in 10% H_2O/He for 1 h at different temperatures (Dashed orange line represents the activity of untreated sample)

4.3.2. Activity enhancement effect of mild steaming

Having established the optimal steaming condition, we performed the mild steaming on the whole Cu-FER series and measured the activities of the steamed samples for selective methane oxidation at ambient methane pressure (Figure 4.2). Compared to the untreated samples, the steamed samples showed, within the typical data dispersion of this type of measurements, a proportional increase in activity across all Cu concentrations. This is a clear indication that the structural transformation leading to activity enhancement took place in the whole Cu-FER series irrespective of the concentration of Cu available. Note that the slope for the activity after steaming remained unchanged at 0.33, suggesting that the level of activity increment is the same for the whole series.
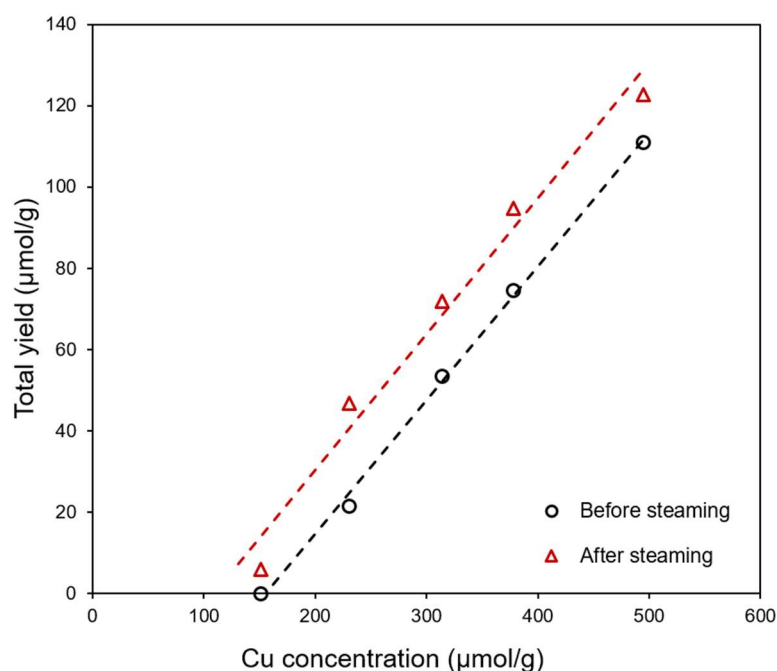
Figure 4.2 Comparison of total yields of selective methane oxidation at ambient methane pressure on Cu-FER samples before and after mild steaming

It was previously shown that at high CH_4 chemical potentials, a second oxygen in the Cu-oxo cluster structures become active in CH_4 oxdiation.[11, 15, 32] Inspired by this, we measured the activity of steamed samples under 40 bar of methane pressure and compared it with the activity under 1 bar. Contrary to what we expected, the steamed series did not show any increase in the methanol yields with 40 bar of methane pressure (Figure 4.3). It seemed that the activity enhancement arising from mild steaming only take effect at ambient methane pressure, while at elevated methane pressure no noticeable difference in activity could be observed after steaming.
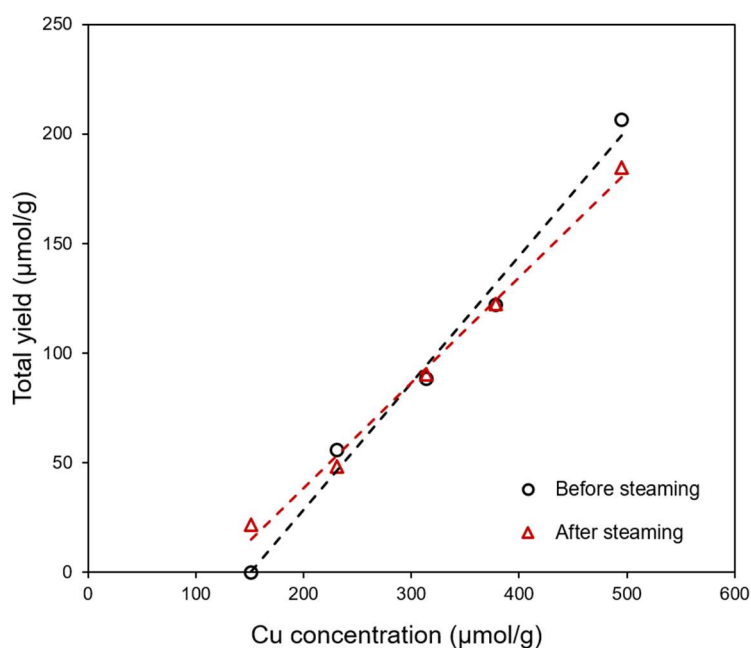

Figure 4.3 Comparison of total yields of selective methane oxidation at ambient methane pressure on Cu-FER samples before and after mild steaming

To follow response of both series to the change of methane pressure, we measured the activities under different methane pressures on a high Cu-loading sample (Cu-FER-500) before and after mild steaming. To account for the variation of total concentration of active sites in each of the series, we have normalized the yields to the values achieved respectively at highest pressure. As depicted in Figure 4.4, the

activities for both samples showed a strong pressure dependency at the lower range, while quickly converged at the higher range, following a logarithmic dependency on the methane pressure. For the untreated Cu-FER series, we identified a bis-(μ-oxo) dicopper cluster ($[Cu_2O_2]^{2+}$) as the active species through comprehensive spectroscopic studies in Chapter 2. The cluster was shown to activate one CH_4 molecule at ambient pressure and an additional one at 40 bar due to the increased methane chemical potential. Yet, the number of CH_4 molecules activated per cluster is still limited by the active oxygen species available in the cluster. In view of these experimental results, we propose that the interaction between steam-induced EFAl (in form of AlO(OH)) and $[Cu_2O_2]^{2+}$ formed a similar Al-containing $[Cu_2AlO_3(OH)]^{2+}$ cluster as identified in EFAl-rich MOR in Chapter 3, which is able to activate a second methane molecule even at ambient methane pressure. This is what led to the activity enhancement observed for the steamed series tested at 1 bar. However, the formation of the $[Cu_2AlO_3(OH)]^{2+}$ cluster did not increase the overall oxidation capacity, which is given by the maximum yield measured at high chemical potentials. This explains why we did not see any significant differences in the methanol yields at 40 bar for the steamed and unsteamed series (Figure 4.3).
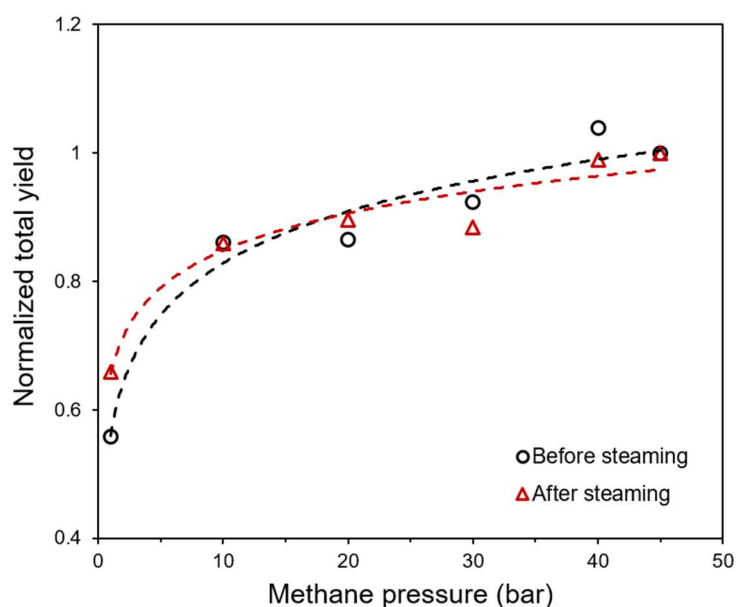

Figure 4.4 Comparison of total yields normalized to 45 bar of selective methane oxidation at different methane pressures on Cu-FER-500 before and after mild steaming (See Table A 4.2 for detailed values for total yields)

4.3.3. Identification of the interaction between formed EFAl and Cu species

In order to test our hypothesis, we first checked the change in Si-OH-Al species by examining its characteristic O-H vibration band of the Si-OH-Al species in the IR spectra. Figure 4.5a shows the O-H band of H-/Cu-FER samples after mild steaming (See Figure A 4.2 for the untreated H-/Cu-FER series). Systematic decrease in the intensity of O-H vibration band can be observed for all samples along with the appearance of a new absorption feature at 3650 cm^{-1}, which can be attributed to the O-H groups attached to EFAl species.[33] These spectral changes are interpreted as the detachment of incorporated Al species from the zeolite framework after the mild steaming process. The average value of consumed BAS per Cu reveals important information on the nuclearity of exchanged Cu species. Compared to the untreated Cu-FER series having an average BAS/Cu of 1.16, the series after steaming showed instead a much lower BAS/Cu of 0.89 regardless of the Cu loading (Figure 4.5b). This is interpreted as a majority of dimeric species (nominal consumed BAS/Cu of 1) residing in the FER framework. The lower ratio could be due to the transformation of bare Cu(II) cations stabilized by Al pairs into other exchanged species (decrease from a nominal consumed BAS/Cu of 2 to a BAS/Cu of 1, on average) or generation of neutral Cu species (nominal consumed BAS/Cu of 0).

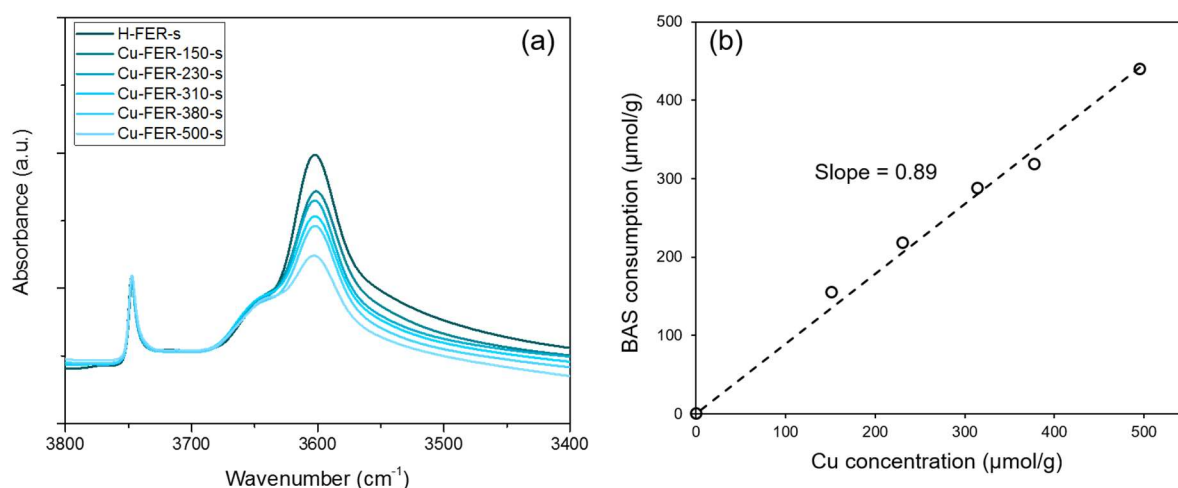**Figure 4.5** (a) Changes in the intensity O-H IR band of Si-OH-Al species with increasing Cu concentrations in steamed Cu-FER samples treated in O$_2$ after activation in vacuum; (b) Correlation of BAS consumption with different Cu concentrations

Next, we probed the steamed materials with low-temperature NO adsorption with IR spectroscopy, since the vibration frequencies of an absorbed NO molecule reveal information on the aggregation and oxidation states of the corresponding Cu species. Note that the activation procedure prior to an IR measurement requires heating up a sample under vacuum condition, which induces the autoreduction of certain Cu(II) species to Cu(I).[30, 31] It is, therefore, indispensable to include an oxidative treatment to the samples before the NO exposure, to reoxidize the autoreduced Cu species and ensure the probed species identical to those in the working catalyst.
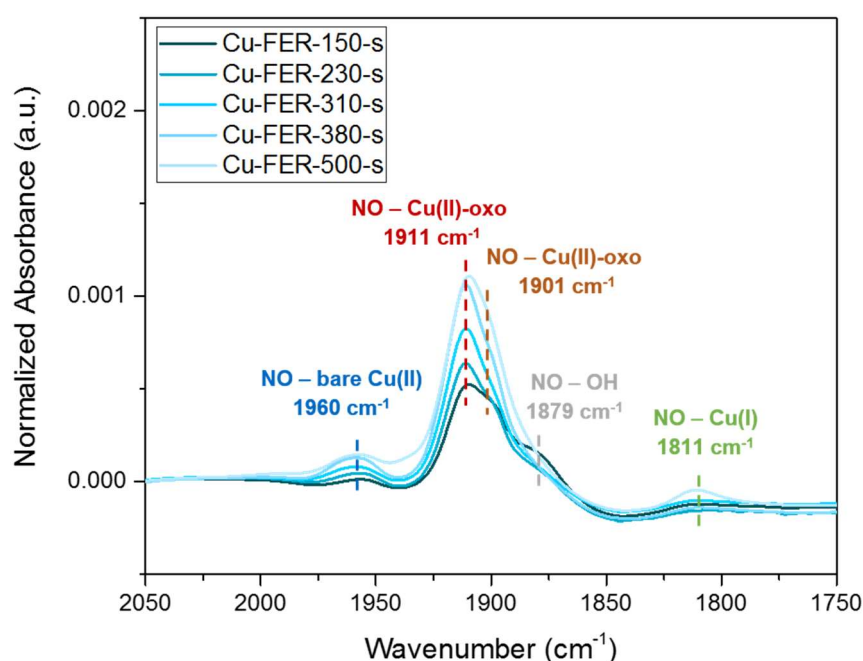

Figure 4.6 Differential IR spectra of Cu-FER samples with NO adsorption after mild steaming

The NO adsorption patterns on the steamed Cu-FER series can be seen in Figure 4.6 (See Figure A 4.3 for the NO adsorption pattern on untreated Cu-FER series). Overall, the absorption features are fairly similar between the two series, despite some differences in the intensity of certain species. We have established in our previous work that the high wavenumber band at 1960 cm^{-1} is attributed to the NO adsorbed bare Cu(II) cations. The main band in the region of 1930-1860 cm^{-1}, on the other hand, is composed of NO adsorbed on two types of Cu(II)-oxo species centered respectively

at 1911 cm^{-1} and 1901 cm^{-1} and NO adsorbed on surface hydroxyl groups of the zeolite at 1879 cm^{-1}. In combination with methane exposure, the band at 1911 cm^{-1} was identified to be the fingerprint of catalytically active $[Cu_2O_2]^{2+}$ cluster. One additional feature at 1811 cm^{-1} exclusively to the steamed series is attributed to a mononitrosyl absorbed on Cu(I) species, which means, unlike the untreated samples, a small concentration of Cu(I) species generated during mild steaming cannot be reoxidized from the oxidative treatment.
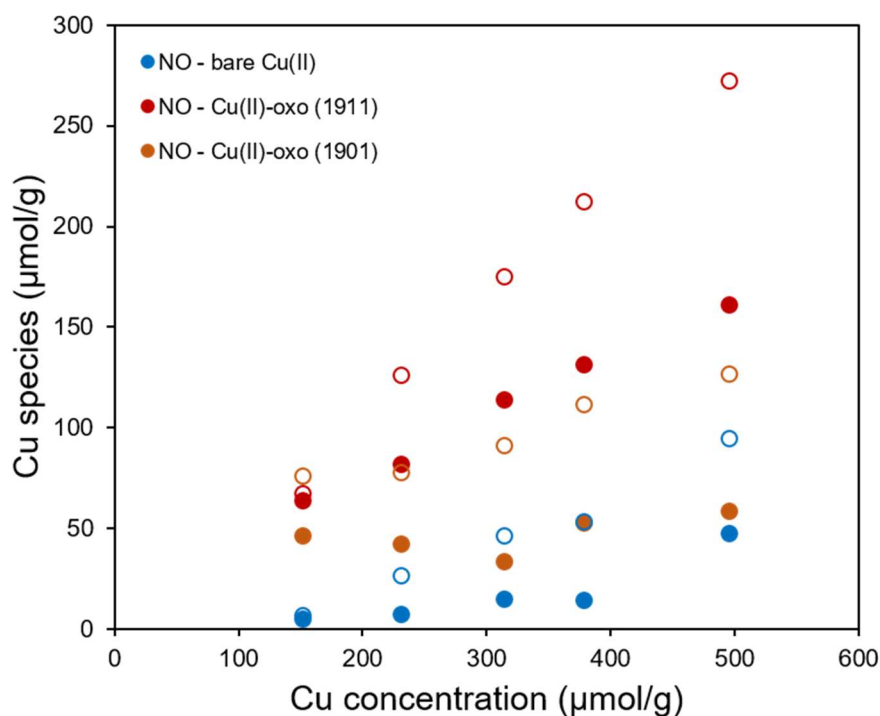

Figure 4.7 Distribution of each Cu species in steamed Cu-FER determined by IR with NO adsorption; hollow circles with corresponding colors represent the same species in the untreated series

Quantitative information of each species in the steamed samples can be obtained from the deconvolution of the NO adsorption bands (Figure 4.7). In comparison to the untreated samples, almost all absorption features related to Cu(II) species became less intense. However, the intensity of the active $[Cu_2O_2]^{2+}$ clusters (NO band at 1911 cm^{-1}) appeared to be less affected than that of the other inactive ones, making it the dominant species for all steamed samples. Based on the molar extinction coefficient calculated from untreated samples, we can quantify the concentration of the active

$[Cu_2O_2]^{2+}$ clusters for each sample and in turn the CH_4 to Cu stoichiometry of the reaction, from the total methanol yields. Table 4.1 summarized the numeric information on the net changes of related Cu species in the steamed samples with respect to the untreated one. The results showed that the active $[Cu_2O_2]^{2+}$ clusters determined from NO adsorption cannot fully account for the activities achieved on each sample.

Table 4.1 Net changes in concentration and percentage of Cu species in steamed Cu-FER series with respect to untreated series determined from deconvolution of NO adsorption bands

Cu conc. (μmol/g)	Net changes in concentration (μmol/g) / in percentage		
	bare Cu(II)	Cu(II)-oxo (1911)	Cu(II)-oxo (1901)
151	-1.3 / -19%	-3.4 / -5%	-29.7 / -39%
231	-19.0 / -71%	-44.0 / -35%	-35.5 / -45%
314	-31.5 / -67%	-61.0 / -35%	-57.6 / -63%
378	-38.6 / -72%	-80.7 / -38%	-58.9 / -53%
495	-47.1 / -49%	-111.3 / -41%	-68.4 / -54%

Based on the information above, we assume that the transformation of $[Cu_2O_2]^{2+}$ clusters from close interaction with EFAl might actually inhibit the absorption of NO on the $[Cu_2AlO_3(OH)]^{2+}$ cluster, leading to the decrease in the intensity of the band at 1911 cm^{-1}. Since the overall yield of the sample should be the sum of all active clusters combined, we can then calculate the yield and in turn the concentration of $[Cu_2AlO_3(OH)]^{2+}$ cluster (Table A 4.3) according to the difference of the total yield and that contributed by free $[Cu_2O_2]^{2+}$ clusters. Based on the distribution of two active clusters obtained from measurements at low CH_4 pressures and IR spectroscopy, the total yield achieved at 40 bar of methane pressure could also be predicted by assigning two methane molecules activated on each of the clusters at 40 bar. As shown in Figure

4.8, a correlation between the predicted and the actual yield obtained at 40 bar showed good linearity with a slope close to one. This indicates that the distribution determined from the IR bands matches well the experimental data from the activity performance.
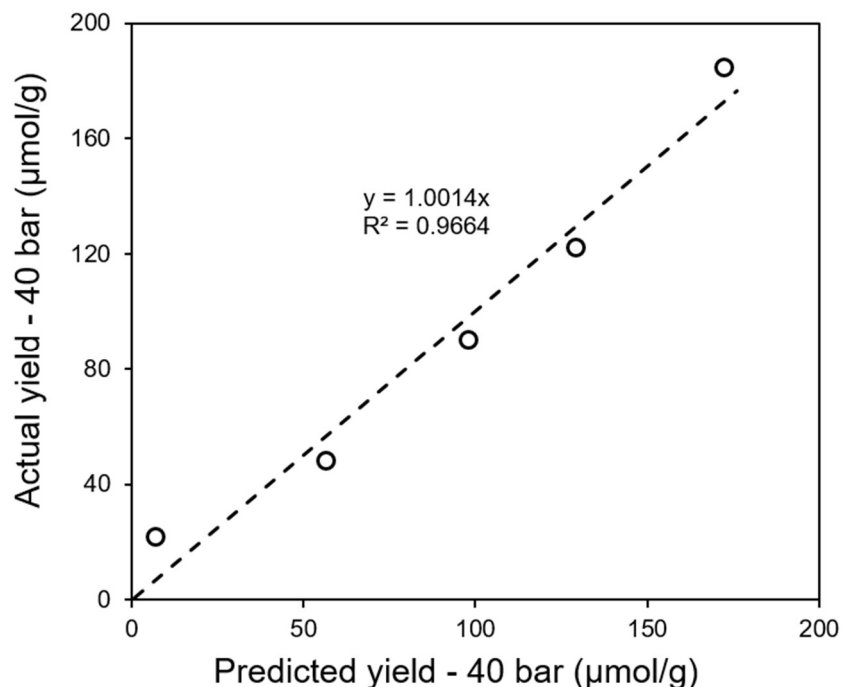

Figure 4.8 Correlation of the actual total yields achieved at 40 bar and the predicted ones based on the analysis of IR bands

Further structural insights were provided by the in situ UV-Vis spectroscopy by monitoring the net change of activated samples upon methane exposure (Figure 4.9). The band centered at 12000 cm^{-1} arises from d-d transition of Cu(II) species, indicative of its reduction to Cu(I) by reaction with methane. The appearance of the d-d transition band is aligned to the ligand-to-metal charge-transfer band (LMCT) at 27000 cm^{-1}, which in essence relates to the active species (extra-lattice O to Cu) reacted with methane.[8, 13, 34] The LMCT band showed lower intensities compared to the untreated samples. This is in line with a lower amount of total active species present in the steamed materials determined from NO adsorption patterns in the IR spectroscopy.
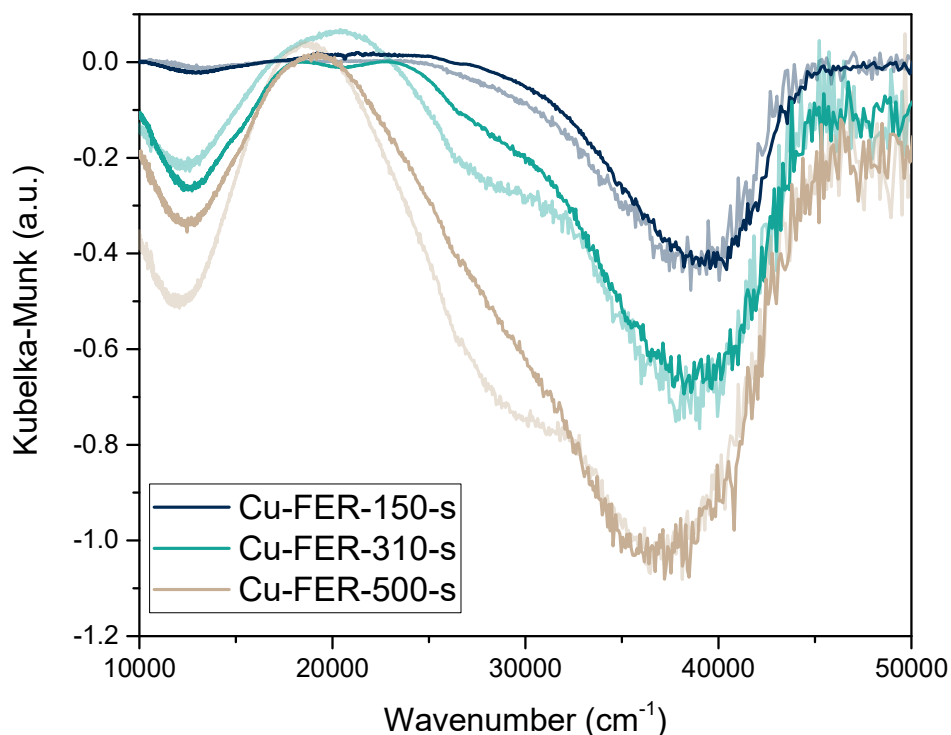
Figure 4.9 Differential UV-Vis spectra of activated steamed Cu-FER series after exposure to CH_4 flow at 200 °C for 30 min. (Lines with lighter colors represent the untreated series)

Based on all this, we proposed that during the mild steaming process, a certain amount of EFAl species formed from detachment from zeolite framework, and in the meanwhile more mobile Cu(I) generated from the autoreduction of existing Cu(II) species moved closer to EFAl and formed the precursor species of $[Cu_2AlO_3(OH)]^{2+}$ clusters. In the following reaction cycle, $[Cu_2AlO_3(OH)]^{2+}$ clusters alongside $[Cu_2O_2]^{2+}$ clusters and other inactive species formed during the activation stage, which altogether contributed to the enhanced activity observed for the steaming series at 1 bar. Yet, both clusters activate two CH_4 molecules at 40 bar, which explained why even with the formation of $[Cu_2AlO_3(OH)]^{2+}$ clusters, the activity of the steamed series observed at high pressure did not differ from the untreated one (Figure 4.10).
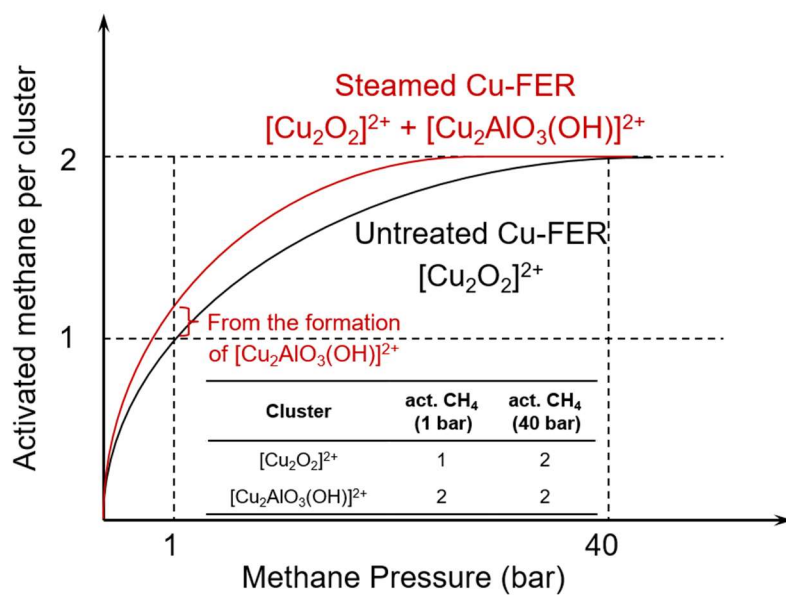
Figure 4.10 Activity change induced by partial formation of $[Cu_2AlO_3(OH)]^{2+}$ clusters from mild steaming of Cu-FER

4.4. Conclusions

In summary, we reported an optimized mild steaming approach on Cu-FER series, which effectively enhanced the overall activity of the Cu-FER samples after steaming. Control experiments showed that the transformation leading to enhanced activity was fully established in a non-oxidative environment at 500 °C. The activity of the steamed series at ambient methane pressure showed a same level of increment, while mild steaming did not make a difference in the activity of steamed series at elevated pressure. By using IR spectroscopy, we found out that the EFAl species was generated from the mild steaming process, which induced the partial formation of $[Cu_2AlO_3(OH)]^{2+}$ clusters from interaction with existing Cu species.

Overall, the study demonstrates the possibility of tuning Cu speciation through generation of EFAl species and the formation of additional active sites. The intrinsically higher reactivity of $[Cu_2AlO_3(OH)]^{2+}$ induced from mild steaming can significantly enhance the overall methane activation efficiency of steamed Cu-FER samples especially at ambient pressure. In particular, this is a first example that the oxidation capacity of Cu clusters active in mild temperature oxidation of methane to methanol can be brought to a maximum at normal pressures and therefore higher conversions are potentially achievable with this approach.

4.5. Experimental Section

4.5.1. Preparation of Cu-FER samples.

Commercial available NH_4-FER (Si/Al = 9) was purchased from Tosoh Corporation. The corresponding H-FER was obtained by calcination of NH_4-FER in synthetic air flow (100 mL/min) at 550°C (10 K/min) for 6 h.

Cu-FER samples were prepared by aqueous ion exchange of H-FER with copper acetate solution under controlled conditions.[13] Typically, Cu^{2+}-exchange was carried out by dispersing 2 g of H-FER at ambient temperature in 120 mL of an aqueous solution of copper acetate (Sigma Aldrich, 99.99%) with desired concentration for 20 h. The pH of the solution was adjusted with aqueous solution of nitric acid (0.2 M) and kept to 5.5 - 6.0 during the Cu-exchange. After the exchange, the sample was separated from the suspension by centrifugation and rinsed four times with double deionized water followed by an intervening centrifugation step after each rinse cycle. The centrifugate was dried at 110 °C for 24 h and labelled as Cu-FER-x (x denotes its Cu content as in x $\mu mol_{Cu}/g_{catalyst}$). All Cu-FER samples were calcined in synthetic air flow at 500 °C (100 mL/min) for 2 h prior to IR measurements. The contents of Si, Al, Na and Cu were measured by atomic absorption spectroscopy (AAS) on a UNICAM 939 AA spectrometer after dissolution in boiling hydrofluoric acid.

4.5.2. Mild steaming of Cu-FER samples.

In a typical mild steaming treatment, 50 mg of Cu-FER (250 - 400 μm) sample was packed in a stainless steel plug flow reactor with a 4-mm inner diameter. A gas mixture containing 10% H_2O in He was flowed continuously through the sample after the reactor was heated up to 120 °C to avoid water condensation. Then, the sample was further heated up to a desired value and kept for a desired time interval before allowed to cool down to 120 °C naturally. After it reached 120 °C, pure He flow was flowed through the reactor for 0.5 h to completely purge out the remaining moisture. The dried sample was ready for the subsequent activity tests or characterization.

4.5.3. Testing of activity for selective oxidation of methane.

The activity of the Cu-FER samples for the selective oxidation of methane to methanol was tested in a three-step reaction scheme. Typically, 50 mg of Cu-FER (250 - 400 µm) sample was packed in a stainless steel plug flow reactor with a 4-mm inner diameter. First, the sample was activated at 500 °C in O_2 flow for 1 h, cooled down to 200 °C and then flushed with He. In the next step, CH_4 was flowed over the sample at 200 °C for 3 h. Finally, the sample was flushed with He and cooled to 135 °C and subjected by a steam-assisted product desorption with 20 % H_2O in He. Reaction products were identified and quantified with a QMG 220 M1, PrismaPlus (Pfeiffer Vacuum) online MS (mass spectrometer) with a C-SEM detector by monitoring the m/z signals of 31, 44 and 46 for CH_3OH, CO_2 and $(CH_3)_2O$. $(CH_3)_2O$ was considered from the condensation of two CH_3OH molecules and therefore the equivalent. The sum of all detected products was taken as the total yield.

4.5.4. In-situ Infrared (IR) spectroscopy.

The IR spectra were recorded on a Vertex 70 spectrometer (Bruker Optics) with a resolution of 4 cm^{-1}. All samples for IR spectroscopy were pressed as self-supporting wafers with a density of ca. 10 mg/cm^2 and activated in vacuum (1.0 x 10^{-7} mbar) at 450 °C with a heating rate of 10 K/min for 1 h. After that, 200 mbar of synthetic air was introduced and kept in the IR cell for another 1 h for oxidative treatment of the samples. Then, the samples were allowed to cool down naturally to 40 °C before the synthetic air was evacuated again for measurement. For the measurements of NO adsorption, the samples were fully cooled down with liquid nitrogen and the IR spectra were recorded after the dosage of NO (0.01 mbar). In case of the measurements with methane reaction, the samples were allowed to cool down naturally to 200 °C instead before evacuation. Next, 10 mbar of methane was introduced and kept for 1 h to react with the activated samples. Similar NO adsorption procedure was then applied after evacuating the methane.

4.5.5. In-situ ultraviolet-visible (UV-Vis) spectroscopy.

The UV-vis spectra were measured on an Avantes AvaSpec 2048 spectrometer equipped with a high-temperature optical fiber (Avantes FCR-7UV400-2ME-HTX). The sample (250 - 400 µm) was placed in a quartz tube with square optical-grade quartz windows. The intensity of the diffuse reflectance UV-vis is shown as the Kubelka-Munk function, defined as $F(R) = (1 - R)^2 / 2R$, where $R = R_s/R_r$, R_s and R_r refer to the signal intensity of the sample and reference, respectively. The reference spectra was taken on the parent H-FER sample. The samples were first activated in synthetic air (16 mL/min) at 450 °C with a heating rate of 10 K/min for 1 h. Then the samples were cooled down to 200 °C and flushed with He (10 mL/min) for 0.5 h, followed by contact with CH_4 flow (16 mL/min) for 1 h. The spectra were recorded periodically with a certain time interval to monitor the changes through time.

4.6. Acknowledgements

4.7. Appendix

Table A 4.1 Physicochemical properties of Cu-FER samples

Sample	Cu acetate conc. (M)	Si/Al	Cu/Al	Na/Al	Cu conc. (wt%)	Cu conc. (μmol/g)
Cu-FER-150	0.0025	9	0.09	0.002	0.96	151
Cu-FER-230	0.005	9	0.13	0.002	1.47	231
Cu-FER-310	0.00625	9	0.18	0.002	2.00	314
Cu-FER-380	0.0075	9	0.22	0.001	2.40	378
Cu-FER-500	0.01	9	0.32	0.001	3.14	495

Table A 4.2 Total yields achieved at different methane pressures for Cu-FER-500 sample before and after steaming

Pressure (bar)	Total yields (μmol/g) before steaming	Total yields (μmol/g) after steaming
1	111.0	122.7
10	171.1	160.2
20	171.2	166.9
30	183.6	165.9
40	206.6	184.5
45	198.8	186.4

Table A 4.3 Distributions and corresponding yields of two active Cu species in the steamed series

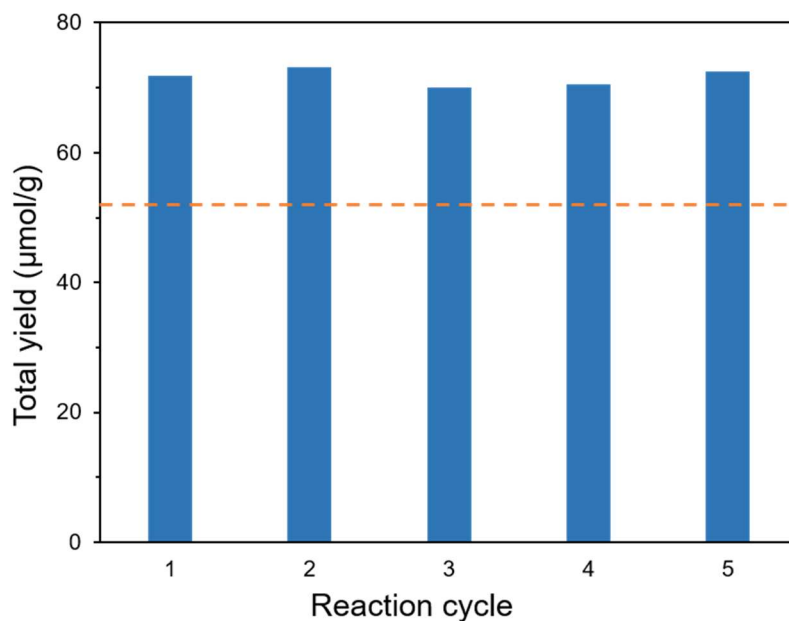| Cu conc. (μmol/g)	Concentration/Yield (μmol/g)				
	Cu conc. $[Cu_2O_2]^{2+}$	Yield $[Cu_2O_2]^{2+}$	Yield $[Cu_2AlO_3(OH)]^{2+}$	Cu conc. $[Cu_2AlO_3(OH)]^{2+}$	Pred. yield (40 bar)
151	64.4	1.0	4.8	4.8	6.8
231	82.2	10.0	36.7	36.7	56.7
314	114.4	26.0	45.8	45.8	97.8
378	131.7	34.7	59.9	59.9	129.3
495	161.4	49.5	73.2	73.2	172.2

Figure A 4.1 Activity of Cu-FER-310-s in repetitive reaction cycles (Orange dashed line represents the activity of untreated sample).
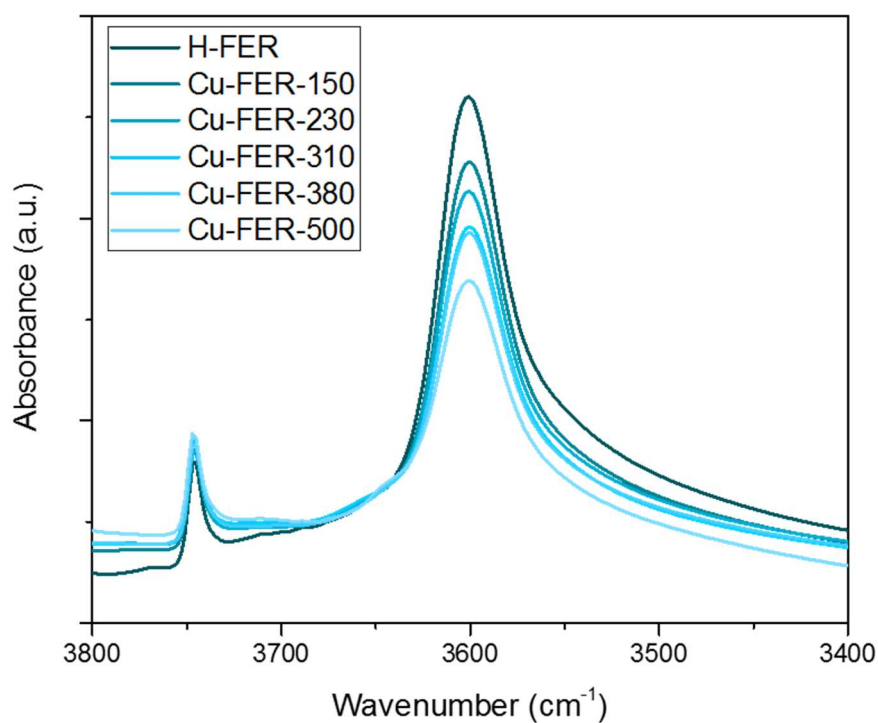

Figure A 4.2 IR spectra for the O-H band of Si-OH-Al species in untreated H-/Cu-FER samples.
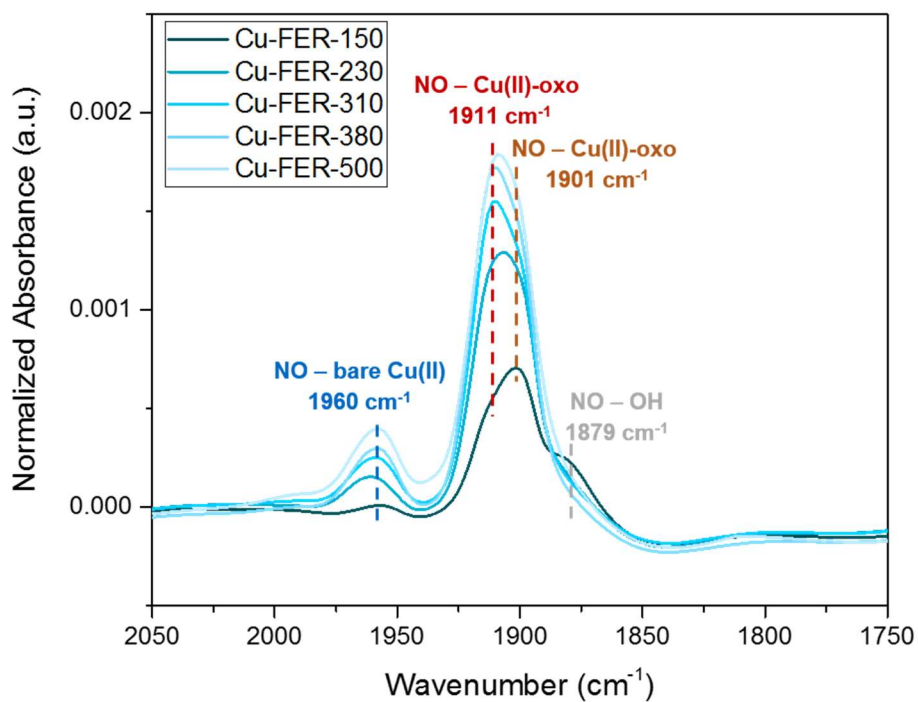
Figure A 4.3 Differential IR spectra of untreated Cu-FER samples with NO adsorption.

4.8. References

1. M. H. Groothaert, P. J. Smeets, B. F. Sels, P. A. Jacobs and R. A. Schoonheydt, *J. Am. Chem. Soc.*, **2005**, *127*, 1394-1395.

2. M. A. Newton, A. J. Knorpp, V. L. Sushkevich, D. Palagin and J. A. van Bokhoven, *Chem. Soc. Rev.*, **2020**, *49*, 1449-1486.

3. A. R. Kulkarni, Z.-J. Zhao, S. Siahrostami, J. K. Nørskov and F. Studt, *Catal. Sci. Technol.*, **2018**, *8*, 114-123.

4. S. Raynes, M. A. Shah and R. A. Taylor, *Dalton Trans.*, **2019**, *48*, 10364-10384.

5. L. Tao, I. Lee and M. Sanchez-Sanchez, *Catal. Sci. Technol.*, **2020**, *10*, 7124-7141.

6. M. Ravi, M. Ranocchiari and J. A. van Bokhoven, *Angew. Chem. Int. Ed.*, **2017**, *56*, 16464-16483.

7. M. H. Mahyuddin, T. Tanaka, Y. Shiota, A. Staykov and K. Yoshizawa, *ACS Catal.*, **2018**, *8*, 1500-1509.

8. H. V. Le, S. Parishan, A. Sagaltchik, C. Göbel, C. Schlesiger, W. Malzer, A. Trunschke, R. Schomäcker and A. Thomas, *ACS Catal.*, **2017**, *7*, 1403-1412.

9. P. Vanelderen, B. E. Snyder, M. L. Tsai, R. G. Hadt, J. Vancauwenbergh, O. Coussens, R. A. Schoonheydt, B. F. Sels and E. I. Solomon, *J. Am. Chem. Soc.*, **2015**, *137*, 6383-6392.

10. B. E. R. Snyder, P. Vanelderen, R. A. Schoonheydt, B. F. Sels and E. I. Solomon, *J. Am. Chem. Soc.*, **2018**, *140*, 9236-9243.

11. G. Brezicki, J. D. Kammert, T. B. Gunnoe, C. Paolucci and R. J. Davis, *ACS Catal.*, **2019**, *9*, 5308-5319.

12. D. K. Pappas, A. Martini, M. Dyballa, K. Kvande, S. Teketel, K. A. Lomachenko, R. Baran, P. Glatzel, B. Arstad, G. Berlier, C. Lamberti, S. Bordiga, U. Olsbye, S. Svelle, P. Beato and E. Borfecchia, *J. Am. Chem. Soc.*, **2018**, *140*, 15270-15278.

13. S. Grundner, M. A. C. Markovits, G. Li, M. Tromp, E. A. Pidko, E. J. M. Hensen, A. Jentys, M. Sanchez-Sanchez and J. A. Lercher, *Nat. Commun.*, **2015**, *6*, 7546.

14. S. Grundner, W. Luo, M. Sanchez-Sanchez and J. A. Lercher, *Chem. Commun.*, **2016**, *52*, 2553-2556.

15. J. Zheng, I. Lee, E. Khramenkova, M. Wang, B. Peng, O. Y. Gutiérrez, J. L. Fulton, D. M. Camaioni, R. Khare, A. Jentys, G. L. Haller, E. A. Pidko, M. Sanchez-Sanchez and J. A. Lercher, *Chem. Eur. J.*, **2020**, *26*, 7563-7567.

16. K. D. Vogiatzis, G. Li, E. J. M. Hensen, L. Gagliardi and E. A. Pidko, *J. Phys. Chem. C*, **2017**, *121*, 22295-22302.

17. N. K. Dandu, J. A. Reed and S. O. Odoh, *J. Phys. Chem. C*, **2018**, *122*, 1024-1036.

18. A. J. Knorpp, A. B. Pinar, M. A. Newton, T. Li, A. Calbry-Muzyka and J. A. van Bokhoven, *RSC Adv.*, **2021**, *11*, 31058-31061.

19. V. L. Sushkevich and J. A. van Bokhoven, *Catal. Sci. Technol.*, **2018**, *8*, 4141-4150.

20. M. Dyballa, D. K. Pappas, K. Kvande, E. Borfecchia, B. Arstad, P. Beato, U. Olsbye and S. Svelle, *ACS Catal.*, **2019**, *9*, 365-375.

21. I. Lee, M.-S. Lee, L. Tao, T. Ikuno, R. Khare, A. Jentys, T. Huthwelker, C. N. Borca, A. Kalinko, O. Y. Gutiérrez, N. Govind, J. L. Fulton, J. Z. Hu, V.-A. Glezakou, R. Rousseau, M. Sanchez-Sanchez and J. A. Lercher, *JACS Au*, **2021**, *1*, 1412-1421.

22. C. J. Heard, L. Grajciar, F. Uhlík, M. Shamzhy, M. Opanasenko, J. Čejka and P. Nachtigall, *Adv. Mater.*, **2020**, *32*, 2003264.

23. S. Schallmoser, T. Ikuno, M. F. Wagenhofer, R. Kolvenbach, G. L. Haller, M. Sanchez-Sanchez and J. A. Lercher, *J. Catal.*, **2014**, *316*, 93-102.

24. Y. Zhang, R. Zhao, M. Sanchez-Sanchez, G. L. Haller, J. Hu, R. Bermejo-Deval, Y. Liu and J. A. Lercher, *J. Catal.*, **2019**, *370*, 424-433.

25. M. Dyballa, U. Obenaus, S. Lang, B. Gehring, Y. Traa, H. Koller and M. Hunger, *Microporous Mesoporous Mater.*, **2015**, *212*, 110-116.

26. M. Müller, G. Harvey and R. Prins, *Microporous Mesoporous Mater.*, **2000**, *34*, 135-147.

27. T. Ikuno, S. Grundner, A. Jentys, G. Li, E. Pidko, J. Fulton, M. Sanchez-Sanchez and J. A. Lercher, *J. Phys. Chem. C*, **2019**, *123*, 8759-8769.

28. C. W. Andersen, E. Borfecchia, M. Bremholm, M. R. V. Jørgensen, P. N. R. Vennestrøm, C. Lamberti, L. F. Lundegaard and B. B. Iversen, *Angew. Chem. Int. Ed.*, **2017**, *56*, 10367-10372.

29.   L. Zhang, I. A. W. Filot, Y.-Q. Su, J.-X. Liu and E. J. M. Hensen, *J. Catal.*, **2018**, *363*, 154-163.

30.   V. L. Sushkevich, A. V. Smirnov and J. A. van Bokhoven, *J. Phys. Chem. C*, **2019**, *123*, 9926-9934.

31.   F. Amano, T. Tanaka and T. Funabiki, *J. Mol. Catal. A Chem.*, **2004**, *221*, 89-95.

32.   P. Tomkins, A. Mansouri, S. E. Bozbag, F. Krumeich, M. B. Park, E. M. Alayon, M. Ranocchiari and J. A. van Bokhoven, *Angew. Chem. Int. Ed.*, **2016**, *55*, 5467-5471.

33.   M. Ravi, V. L. Sushkevich and J. A. van Bokhoven, *Chem. Sci.*, **2021**, *12*, 4094-4103.

34.   Y. Kim, T. Y. Kim, H. Lee and J. Yi, *Chem. Commun.*, **2017**, *53*, 4116-4119.

5. Conclusions

The incentive of this dissertation is to figure out the speciation and reactivity of active Cu-(Al-)oxo clusters hosted in zeolite materials for selective oxidation of methane to methanol.

An FER material with relatively high Al content (Si/Al = 9) was chosen as the host material to study the Cu speciation after an optimized pH-adjusted Cu exchange procedure. Following the activity measurement under ambient and elevated methane pressure, the series was found to demonstrate Cu efficiencies of 0.33 and 0.58 respectively after passing an activity threshold of ca. 150 µmol/g. The consumption ratio of BAS resulted from introduction of Cu species was shown to be constant at 1.16 by examining the intensity change of Si-OH-Al band from IR studies. Probing the samples with NO after an oxidative treatment in the IR cell revealed three co-existing Cu species, with the majority one showing an absorption feature at 1911 cm^{-1}. Exposing the same samples to methane in the IR cell prior to the NO adsorption pinpointed the key role of the majority species as the active center in the reaction. Further correlation of the active species with activity and BAS consumption indicated that the active species was dimeric in nature bearing two active oxygen species, which was located in 8 MR of FER framework. With the help of structural information determined from NO adsorption, the fitting of EXAFS gave constant coordination numbers of 3.5 - 3.6 for the Cu-O path, implying a roughly equal mixture of tri- and tetra-coordinated Cu species. In-situ Raman spectra of the samples showed characteristic absorptions at 601 and 780 cm^{-1}, in good agreement with symmetric and asymmetric stretching vibrations of the Cu-O bond from a tight Cu-O-Cu angle (less than 100°). Based on these results, the active species was assigned to a bis-(μ-oxo)/(μ-η^2:η^2) peroxo dicopper cluster stabilized in the 8 MR of FER.

The effect of EFAl species on Cu speciation was studied on an EFAl-rich MOR zeolite. The oxidation activity measured respectively at 1 and 40 bar of methane pressure hinted at a different speciation of Cu from a conventional Cu-MOR system containing single-site $[Cu_3O_3]^{2+}$ clusters. Replacing the scavenge agent from water to ethanol for the formation of ethyl methyl ether implied that the speciation of Cu was most likely to be divided into two regions marked by a Cu concentration of ca. 300 µmol/g. Based on

previous studies on Cu-(Al-)oxo clusters in MOR, a co-existence of $[Cu_3O_3]^{2+}$ and $[Cu_2AlO_3]^{2+}$ clusters was proposed and the distribution could be derived from the assumptions on the reaction stoichiometries. Through ab initio thermodynamic analysis and molecular dynamics, a $[Cu_2AlO_3(OH)]^{2+}$ cluster was identified to account for the enhanced reactivity at 1 bar of methane pressure for the series and the activation of two methane molecules was shown to be favored in thermodynamics. Both clusters remained roughly equal in amount at lower Cu concentration range, while $[Cu_3O_3]^{2+}$ quickly became the predominant species with higher Cu concentrations over 300 µmol/g. The calculated Gibbs free energies proved that the $[Cu_2AlO_3(OH)]^{2+}$ cluster was stable within a wide range of Cu concentrations, and yet that it tended to form $[Cu_3O_3]^{2+}$ at a significant high level of Cu species present in the system. With the cluster distribution, the derived overall yields of methane oxidation at 40 bar and EME formation were well correlated with the experimental values. Further experimental evidences on the cluster distribution were provided by spectroscopic studies. The Cu L_3-edge XANES showed different ΔE values for samples lying in the two regions, and meanwhile in-situ UV-Vis spectra recorded during the methane reaction also corresponded well with the distribution.

On the basis of the understandings on Cu speciation in FER and the positive role of EFAl, a mild steaming approach was applied to increase the EFAl content in FER in a controlled manner. The optimal steaming condition was settled upon screening relevant parameters. The steamed series was then tested for methane oxidation at different methane pressures. A universal increase in overall yields was observed on measurement at 1 bar, while at 40 bar the activity remained almost unchanged compared to the untreated series. IR spectra of the steamed series showed an intensity decrease of the Si-OH-Al band and a simultaneous increase of a shoulder band at 3650 cm^{-1}, corresponding to Al-OH on EFAl species. This pointed to the transformation of Al species from the zeolite framework into EFAl after mild steaming. Therefore, the reaction behavior demonstrated by the steamed series could be attributed to the partial formation of similar $[Cu_2AlO_3(OH)]^{2+}$ clusters as in the EFAl-rich MOR, so that the overall yields achieved at 1 bar increased and yet still were bound to the oxidation capacity of maximum two methane molecules per cluster. To obtain more information on the Cu speciation, the steamed samples were probed by NO adsorption with IR spectroscopy. Similar NO adorption features were observed from the steamed series

but with generally lower intensities. Assuming that $[Cu_2AlO_3(OH)]^{2+}$ cluster did not take up NO probes, the distribution of $[Cu_2AlO_3(OH)]^{2+}$ and remaining $[Cu_2O_2]^{2+}$ could be estimated based on the band intensity and overall yield achieved at 1 bar. The yield at 40 bar derived from corresponding distribution matched very well with the experimental value. In-situ UV-Vis spectra recorded during the methane reaction agreed well with the distribution determined from IR spectra with NO adsorption.

Curriculum Vitae

Lei Tao

Born on 18.01.1993 in Shanghai, China

09/2018 – 02/2022	Doctoral researcher at Lehrstuhl für Technische Chemie II (Prof. Dr. Johannes A. Lercher)
	Fakultät für Chemie
	Technische Universität München, Germany
	Topic: "Formation of Cu-(Al-)oxo Clusters in Zeolites for Selective Oxidation of Methane to Methanol"
09/2015 – 06/2018	Master of Science in Physical Chemistry
	Department of Chemistry
	Fudan University, China
	Master thesis on "Construction of Novel Catalytic Pathways for Biomass-Based Furanic Compounds"
09/2011 – 06/2015	Bachelor of Science in Chemistry
	Department of Chemistry
	Fudan University, China
	Bachelor thesis on "Heterogeneous Gold Catalyzed Selective Reductive Transformations of Quinolines"

List of Publications

Journal Articles

Tao, L.; Lee, I.; Khare, R.; Jentys, A.; Fulton, J. L.; Sanchez-Sanchez, M.; Lercher, J. A., Speciation of Cu-oxo clusters in FER for selective oxidation of methane to methanol. *Chem. Mater.* **2022** (Revised).

Tao, L.; Khramenkova, E.; Lee, I.; Ikuno, T.; Fulton, J. L.; Pidko, E. A.; Sanchez-Sanchez, M.; Lercher, J. A., Influence of Cu Concentrations on the Equilibrium of Cu-(Al-)oxo Cluster Speciation in Mordenite for Oxidative Transformations of Methane. (in preparation)

Tao, L.; Zhang, S.; Sanchez-Sanchez, M.; Lercher, J. A., Activity Enhancement from Formation of Cu-Al-oxo Clusters in FER via Mild Steaming. (in preparation)

Lee, I.; Lee, M. S.; Tao, L.; Ikuno, T.; Khare, R.; Jentys, A.; Huthwelker, T.; Borca, C. N.; Kalinko, A.; Gutiérrez, O. Y.; Govind, N.; Fulton, J. L.; Hu, J. Z.; Glezakou, V. A.; Rousseau, R.; Sanchez-Sanchez, M.; Lercher, J. A., Activity of Cu–Al–Oxo Extra-Framework Clusters for Selective Methane Oxidation on Cu-Exchanged Zeolites. *JACS Au* **2021**, *1*, 1412.

Tao, L.; Lee, I.; Sanchez-Sanchez, M., Cu oxo nanoclusters for direct oxidation of methane to methanol: formation, structure and catalytic performance. *Catal. Sci. Technol.* **2020**, *10*, 7124.

Tao, L.; Yan, T. H.; Li, W.; Zhao, Y.; Zhang, Q.; Liu, Y. M.; Wright, M. M.; Li, Z. H.; He, H. Y.; Cao, Y., Toward an Integrated Conversion of 5-Hydroxymethylfurfural and Ethylene for the Production of Renewable p-Xylene. *Chem* **2018**, *4*, 2212.

Tao, L.; Wang, Z. J.; Yan, T. H.; Liu, Y. M.; He, H. Y.; Cao, Y., Direct Synthesis of Pyrroles via Heterogeneous Catalytic Condensation of Anilines with Bioderived Furans. *ACS Catal.* **2017**, *7*, 959.

Lin, J. D.; Bi, Q. Y.; Tao, L.; Jiang, T.; Liu, Y. M.; He, H. Y.; Cao, Y.; Wang, Y. D., Wettability-Driven Palladium Catalysis for Enhanced Dehydrogenative Coupling of Organosilanes. *ACS Catal.* **2017**, *7*, 1720.

Zhu, M. M.; <u>Tao, L.</u>; Zhang, Q.; Dong, J.; Liu, Y. M.; He, H. Y.; Cao, Y., Versatile CO-assisted direct reductive amination of 5-hydroxymethylfurfural catalyzed by a supported gold catalyst. *Green Chem.* **2017**, *19*, 3880.

Li, S. S.; <u>Tao, L.</u>; Wang, F. Z. R.; Liu, Y. M.; Cao, Y., Heterogeneous Gold-Catalyzed Selective Semireduction of Alkynes using Formic Acid as Hydrogen Source. *Adv. Synth. Catal.* **2016**, *358*, 1410.

Li, S. S.; <u>Tao, L.</u>; Zhang, Q.; Liu, Y. M.; Cao, Y., Recent Advances in Nano-Gold-Catalyzed Green Synthesis and Clean Reactions. *Acta Phys. -Chim. Sin.* **2016**, *32*, 61.

<u>Tao, L.</u>; Zhang, Q.; Li, S. S.; Liu, X.; Liu, Y. M.; Cao, Y., Heterogeneous Gold-Catalyzed Selective Reductive Transformation of Quinolines with Formic Acid. *Adv. Synth. Catal.* **2016**, *358*, 1410.

Book Chapters

Li, S. S.; <u>Tao, L.</u>; Liu, Y. M.; Cao, Y., Towards More Sustainable Chemical Synthesis, Using Formic Acid as a Renewable Feedstock. Invited Chapter 12 in Nanoporous Catalysts for Biomass Conversion, eds. Feng-Shou Xiao and Liang Wang (John Wiley & Sons Ltd, UK, 2017).

Oral Presentations

<u>Tao, L.</u>; Lee, I.; Sanchez-Sanchez, M.; Lercher, J. A., Cu-oxo clusters in FER framework for the selective oxidation of methane to methanol. 54. Jahrestreffen Deutscher Katalytiker, Weimar, Germany, March 2021.

Poster Presentations

<u>Tao, L.</u>; Lee, I.; Sanchez-Sanchez, M.; Lercher, J. A., Zeolite hosted Cu-oxo clusters for direct methane oxidation to methanol. 8th Conference of the Federation of European Zeolite Associations, Brighton, UK, July 2021.